WAVE ENERGY DISTRIBUTION ACROSS THE AGULHAS BANK,

A SOURCE OF RENEWABLE ENERGY FOR A SEAWATER PUMPED STORAGE SCHEME

FRANCISCO GEMO ALBINO FRANCISCO

THESIS PRESENTED FOR THE DEGREE OF MASTER OF SCIENCE

IN THE DEPARTMENT OF OCEANOGRAPHY

UNIVERSITY OF CAPE TOWN
IYUNIVESITHI YASEKAPA • UNIVERSITEIT VAN KAAPSTAD

JANUARY 2013

Abstract

This study was undertaken to assess whether the available and recoverable wave power density resource on the Agulhas Bank (South Africa) is sufficient to support a Pumped Storage Scheme (PSS). We used 5 months of insitu wave data collected in a depth of 80 m off Cape Agulhas, Mossel Bay, Tsitsikamma and Cape Recife, together with model wave data from the National Centre for Environmental Prediction (NCEP) - WAVEWATCH III which was reanalysed by the French Research Institute for Exploitation of the Sea (IFREMER) - IWOAGA. The wave power density resource (**P**) was estimated by calculating the wave energy flux across a unit diameter circle of the wave field, and the resource available by the lateral transfer of wave energy along a linear array of wave energy converting devices. The results showed that Cape Agulhas had the most available **P** (75% for 40 kW/m, 25% for 17 kW/m, with an average of 31 kW/m) followed by Mossel Bay (75% for 34 kW/m, 25% for 14 kW/m, with an average of 25.2 kW/m), Tsitsikamma (75% for 32 kW/m, 25% for 13 kW/m, with an average of 25.0 kW/m), and Cape Recife (75% for 30 kW/m, 25% for 12 kW/m, with an average of 23.7 kW/m). For the entire nearshore domain, the most frequent waves had values of **P** between 30 kW/m – 50 kW/m, with the dominant direction of propagation from the southwest. On average, the diurnal cycle was characterised by a peak in energy in the evening nearshore and in the afternoon offshore. The seasonal cycle was characterised by a peak in winter (40 – 50 kW/m) and trough in summer (20 – 30 kW/m). The interannual variability signal had a strong correlation with regional Sea Level Pressure (**SLP**), surface westerlies winds, and regional sea surface currents. It is also correlated to El Niño Southern Oscillation (**NINO3**) and the Southern Annular Mode (**SAM**). In terms of the total annual wave energy resource (**P**), approximately 380 TWh/yr, are available near the 80 and 128 m water depths. For the PSS, it was estimated that for a moderate flow rate of 50 m^3s^{-1}, the required power to pump sea water to an upper reservoir with a volume of 5 and 15 million m^3 is approximately 43 and 150 MW. The pumping process would take between 28 and 82 hours. This study concludes that the entire Agulhas Bank has indeed sufficient wave energy resource to supply a large scale PSS.

Declaration

"I know the meaning of Plagiarism and declare that all of the work in this document, save for that which is properly acknowledged, is my own".

Date and Place: Signature

Supervisors

Prof. Chris Reason:
Department of Oceanography,
University of Cape Town

Dr. Mike Roberts:

Oceans and Coasts,
Department of Environment Affairs, South Africa,
Bayworld Centre for Research and Education

Acknowledgments

I would like to thank my Supervisors Prof. Chris. J. Reason for giving me the opportunity to come and study at the University of Cape Town, and Dr. Mike Roberts for giving the opportunity to research wave energy at this level. For both my Supervisors I would like to say thank you very much for not only supporting me throughout the entire course, but also for believing in my work and for pushing me to complete this MSc with success. I also would like to thank Prof. Frank Shillington for his valuable support and availability and interest in my research. To Prof. Mavume and Dr. Manhique, I am very grateful for their support on paving my way to the University of Cape Town.

I gratefully acknowledge the NANSEN TUTU CENTRE for Marine Environmental Research for fully sponsoring my MSc studies.

I also would like to acknowledge my colleagues who always supported me and taught me MATLAB.

Thanks you Bayworld Centre for Research and Education is the Person of Dr. Mike Roberts for providing me insitu wave data.

I want to thank my family and friends for believing and supporting me in every step I make. Special and big thanks to God my Lord for every single thing I am and for the greatness awaiting for me.

Contents

List of Figures

List of Tables

Acronyms

PSS	Pumped Storage Scheme
NOAA	National Oceanic and Atmospheric Administration
NCEP	National Centre for Environmental Prediction
IFEMER	French Research Institute for Exploitation of the Sea
IWOAGA	International Ocean Waves for Geophysical and other Applications
CERSAT	Centre for Satellite Exploitation and Research
SLP	Sea Level Pressure
SST	Sea Surface Temperature
ENSO (NINO3)	El Nino Southern Oscillation
SAM	Southern Annular Mode
SOI	Southern Oscillation Index
WE	Wave Energy
WEC	Wave Energy Converter
SWEC	Stellenbosch Wave Energy Converter
TOC	Threshold Operating Condition
MOC	Maximum Operating Condition
ROC	Rated Operating Condition
ADCP	Acoustic Current Doppler Profiler
AWAC	Acoustic Wave and Current profiler
AST	Acoustic Surface Tracking
MLM	Maximum Likelihood Method
JAN	January
FEB	February
MAR	March
APR	April
MAY	May
JUN	June
JUL	July
AUG	August
SEP	September
OCT	October
NOV	November
DEC	December
SWAN	Simulating Waves Nearshore
WAM	Wind Wave Model
WaMos	Wave and Surface Current Monitoring System
ITCZ	Intertropical Convergence Zone

List of Symbols

α	Angle between the wave components
a	Wave amplitude
U	Wind speed
c	Phase speed
C_G	Group speed or group velocity
u^*	Friction velocity
m	Meter
s	second
km	kilometre
C_D	Dimensional coefficient
$\boldsymbol{\tau}$	Drag coefficient
u_{10}	Wind speed at 10 m above ocean surface
η	Magnitude of any type of surface disturbance (elevation)
t	time
f	Coriolis frequency
g	Acceleration due to Earth's gravity
H	Water depth
k	Wave number
K	Wave number magnitude
λ	Wave length
w	Dispersion (angular frequency)
x	Displacement on x direction
y	Displacement on y direction
E_k	Kinetic energy
E_P	Potential energy
F	Energy flux across a vertical plane
S	Function of wave spectra
θ	Wave direction
m_n	Spectral momentum
T_n	Wave period
Z	Auto-covariance
σ	Variance
$\boldsymbol{\rho}$	Water density
$\boldsymbol{P}$	Wave power density
P_{PSS}	Power necessary for the pumped storage scheme

Chapter 1

Introduction

1.1 General

About 91% of the South African's national electricity is produced by coal, 4% is produced by hydro power and pumped storage schemes (PSS) and the remainder 5% is generated by nuclear plants (Winkler 2006). Within the South African total final energy consumption, the electricity sector contributes with ~ 28 %, and ~ 95 % of this electricity is supplied by the national utility Eskom, and the other 5% is supplied by other local sources (Winkler 2006). Although the South African national electricity grid is comprehensive, most of the country's rural areas are excluded hence, are supplied by renewable energy such as small hydro and solar photovoltaic.

According to the 2004 White Paper on Renewable Energy, South Africa has renewable energy resources that potentially can contribute 10 000 GWh to the country's future electricity supply, and it also states that at the moment, the main challenge is to find appropriate technology to extract this kind of energy. Early studies report that in the southern Africa region, South Africa has excellent physical conditions for extracting ocean energy due its natural oceanographic and geomorphologic characteristics (Holm et al 2008, p 35, Hammar and Ehnberg 2010). According to these studies, the Agulhas Bank region has an average wave power density (**P**) of 50 kW/m of wave crest, with the southwest coast being the most energetic. From the total wave power resource, it is believed that South Africa can convert ~ 8 000 to 10 000 MW towards the country's future power supply.

Approximately three quarters of the total energy coming from the Sun is received by the oceans. This energy heats the sea surface and is then transformed into wind and waves. Ocean waves therefore, carry large amounts of energy that can be converted into terawatts (TW) of useful work, such as electricity, water pumping, and water desalination among others. Wind waves (surface gravity waves), which are the most frequent in the ocean wave spectrum, are generated by the stress between wind and the surface water. Wave energy is the transport of the accumulated energy from the sun and wind by the ocean waves. **P** is the wave energy flux across a unit diameter circle of a wave field. This quantity varies in time and space according to the variation of the regional wind field.

The use of wave energy is not a new concept. It is been explored for over 200 years (Boyle 2004). However it was only in the 1980s that the concepts of renewable energy conversion became viable with results that wind wave and solar energy conversion has been utilized. Among these three renewable energies, wave energy has the advantage that it is the most predictable and reliable, but it has economical and technical limitations and is still not cost-competitive compared to conventional

energy resources. The economic and technical limitations that wave energy faces will need to overcome by advances in modern technology which will improve the conversion efficiency and reducing costs.

Recently, large scale wave energy extraction projects have started to operate in several locations around the globe. Many of these projects are running as prototypes, but there are also some commercial projects installed in Portugal, UK, Norway, and Australia among other nations (Johnson 2007). In South Africa, the Stellenbosch Wave Energy Converter (SWEC) prototype has been developed at the Stellenbosch University. This system is a 5 MW rated submerged attenuator which has been developed as a prototype. Eskom is now interested in promoting wave power along the South African coast.

Modern concepts of wave energy converting systems extract the kinetic energy from the surface gravity waves and from subsurface pressure fluctuations and convert it into useful work. Although several types of conversion of wave energy exist, only two outputs can be obtained from the conversion, namely, the mechanical or electrical energy. Wave energy can be directly converted into electricity or can be first converted into mechanical energy that can then pump sea water into a turbine or pumped storage scheme and then via turbines be converted into electricity.

1.2 The pumped storage scheme (PSS)

In South Africa, the demand for electricity is rising as the national grid expands. With this, is the need for backup systems that can respond quickly to sudden surge demands or failure of base-load plants. The PSS concept can provide suitable systems to support the national grid during these times.

From site-screening studies, Eskom has now identified 19 sites along the South-Western Cape coast suitable to build seawater pumped storage dams (Figure 1- 1) where wave and wind energy can be converted and used to pump sea water to a reservoir atop mountain. During peak periods or failure of the base-load plant, the sea water in the reservoir can be released and allowed to flow down to the ocean through a penstock (waterway or pipeline) past a turbine generator. This scheme requires a small flow, implying that the entire system is compact comprising one or more turbines, a generator and some housing (Figure 1- 2).

Turbines used in a PSS are designed to run in either flow direction, either extracting energy from the water as a turbine (Figure 1- 3b), or delivering energy to the system as a pump (Figure 1- 3a). The location of the dam must be suitable, meaning that the upper reservoir must not be too far away from the lower reservoir which in our case is the ocean. There is always power loss associated with the conversion process, but modern turbines are very efficient and can retrieve nearly 95 % or more of the input electrical energy.

At present, pump storage schemes are the only practicable and economically viable way to store electrical energy in very large quantities and it plays a large role in national and even international power systems (Boyle 2004). For example, in South Africa, the Drakensberg PSS has been operated by Eskom since 1982 and Palmiet PSS in the Western Cape has been operating by Eskom since 1982 contributes 1 000 MW and 400 MW during the peak periods respectively. At the Drakensberg PSS, the water is pumped from the Thukela River over the Drakensberg escarpment (upper reservoir) into the Wilge River (lower reservoir), a tributary of the Vaal River. At the Palmiet PSS, water is transferred from the Palmiet River catchment into the Steenbras Dam (upper reservoir) to supplement Cape Town's water supply (lower reservoir) (GI 003 2010). Both systems use the electricity from the national grid to pump the water to the upper reservoir during the off-peak periods.

New concepts of pumped storage schemes use a combination of renewable energy power sources instead of power from the grid; these schemes are being implemented successfully and are viable in many locations worldwide (Guzman 2010, Wild et al 2009).

1.3 Research questions

With a view to implementing a similar PSS, this study investigates the characteristics of wind wave fields on the Agulhas Bank and assesses if the naturally available and technically recoverable wave power density resource is sufficient to sustain a PSS. This thesis addresses the following questions:

- What are the wave climate characteristics at selected sites of the Agulhas Bank?
- What is the spatial and temporal variability of the wave climate across the Agulhas Bank?
- What are the long term wave field trends in relation to global climate indices?
- What is the power required for a typical PSS device?
- Is the wave power density resource across the Agulhas Bank sufficient for such a PSS?

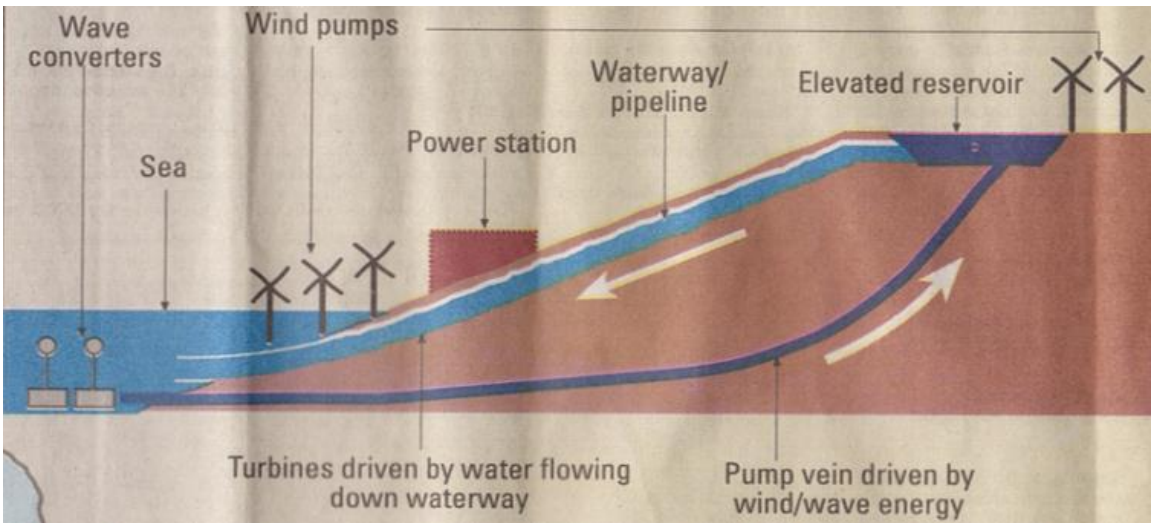

Figure 1- 1. The Eskom idealized pumped storage scheme (Adapted from Eskom).

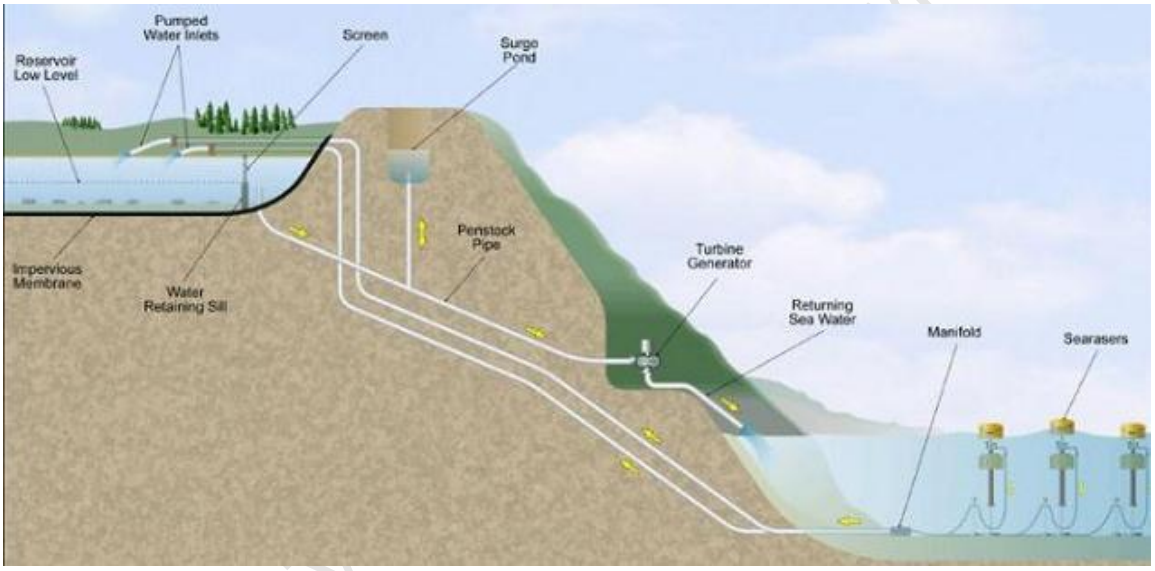

Figure 1- 2. A scheme of wave powered sea water pumps. A diagram of SEARASERS wave pumps (Adapted from Timera Energy 2012).

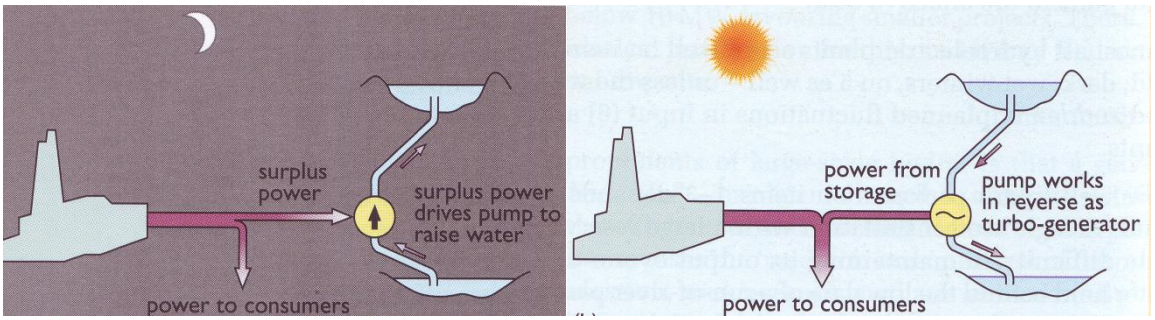

Figure 1- 3. The pumped storage system. (a) At lower demand time; (b) At higher demand time (Adapted from Boyle 2004).

Chapter 2

Literature Review and Theory

2.1 Ocean waves

2.1.1 General

The oscillatory motion is the most basic feature of all physical phenomena in the nature. This oscillatory motion is the medium in which information between two points is transmitted as a function of space and time without the movement of the medium across its path. The energy and phase of the disturbance due to the oscillatory motion travels during the propagation of the disturbance with in, generally no mass transport. This phenomenon is called wave. There are two types of wave electromagnetic waves which do not depend on the medium for its propagation and mechanical waves which only propagate through a medium and are generated due to an existence of a restoring force that acts to bring the system back to its undisturbed state. Inertia causes the system to overshoot after it has returned to its undisturbed state. For the restoring force is due to compressibility or elasticity of the medium, which can be liquid solid or gaseous. Moreover, the particles in this kind of waves can move parallel to the wave propagation. These are known as pressure, elastic or compression waves. The other waves are generated when the disturbance makes the particle to move both perpendicular and parallel to the wave propagation. These waves more frequently occur at the free surface of a liquid or between two fluids with different density, and the gravity is the force that acts as the restoration force of the system. These waves are called surface gravity and internal gravity waves respectively (Kundu and Cohen 2008).

2.1.2 Wind wave formation mechanism

When the winds blow over the ocean surface for a certain period of time, the free surface of the ocean will react as a consequence of momentum transference between the atmosphere and ocean. A wave field initially at rest at the ocean surface is influenced by two principal mechanisms: the first is the resonance between the surface wave modes and the advected surface pressure fluctuations associated with the turbulence caused by the wind. The second is the gradual instability caused by the air flow over a surface already disturbed (Phillips 1962). The area of the ocean many km in length over which the winds blow to generate waves is called fetch. The invariable turbulence of the lower atmosphere causes an arbitrary pressure distribution over the ocean surface. This effect causes convective motions and also cause turbulent eddies over the water surface. The response of the water surface depends on the magnitude of the pressure fluctuations of a given wave number (number of waves that coexist over

a specified distance) and depends on the time over which the pressure and the wave components remain in concordance as they both move along (Phillips 1962). This time scale reaches a maximum when the advection speed of the pressure field is equal to the phase speed of the free surface waves of the same wave number. The pressure forcing remains in phase with the wave motion for the longest time until the interaction among the turbulent eddies modifies the surface pressure distribution (Phillips 1962). If the angle between the wind and the wave components is α and the wind speed on the direction of the propagation of the wave is U, then the condition for resonance will be $c = Ucos \propto$. If this is satisfied, the energy transfer from the wind to the waves must reach directional maximum for a particular frequency at $\propto = \pm cos^{-1}(\frac{c}{U})$ (Phillips 1962). Instability theories (e.g. Toba 1988) suggest that the growth rate of the waves from slow small ripples to fast long waves is proportional to the magnitude of the disturbance already present in the system, it means that the wave height is an exponential function of time, but the resonance mechanism is independent of the waves already existing, and provides a linear rate of growth of wave energy. In initial conditions when the sea is calm, $c \ll U$ and the initial growth will be linear until the waves become large enough for the instability to occur. As an exponential function, after this critical point, the growth rate will increase fast so that the resonance mechanism triggers instability. If $c \approx U$ the waves and the wind travel at ~ the same speed, and the amplification rate is very slow. Thus the instability will hardly occur as the resonance is on its optimal magnitude (Phillips 1962). If the wind blows for a long time, the waves will not grow infinitely, however the waves will reach a state of saturation over at least part of the spectrum. Next is the formation of whitecaps and the energy of the system is lost by turbulence in the water surface (Phillips 1962).

For a free surface of a fluid to change from the steady state into waves due to the movement of another interactive fluid, the relative velocity between them must exceed $U_{crit.} = c\frac{1+s}{\sqrt{s}}$, where s is the density ratio of the two fluids and c is the velocity of the wave form or phase speed (Russell 1954). Calculations however, using this formula are not realistic for ocean wave formation as the wind speed given by this relation is greater that the real wind speed observed in the ocean which generates waves.

In ocean-atmosphere interaction, the momentum is transferred between the atmosphere and oceans by the frictional force known as drag. Drag is the force which resists the differential moment between media and the quantity of frictional force per unit of surface contact area; this is mostly called shear stress τ and is felt by both media. Because of the differences in magnitude between the molecular viscosity and the turbulence caused by shear stress, the term friction is replaced by turbulence, thus there is turbulent shear and turbulent drag (Russell 1954, MacHutchon 2006).

The kinematic stress u^{*2} is related to the interaction between two fluids of different densities. If ρ_w is the ocean water density and ρ_a is the air density and u^* is the friction velocity, then $u^{*2} = \tau/\rho$. The typical u^* vary from 0 m/s (no wind) to 0.5 m/s (moderate wind) and 1.0 m/s (strong wind). In the

real ocean, the turbulent stress is positively correlated with the wind speed and is greater when the ocean surface is already rough, thus the origin of the dimensional coefficient C_D which correlate the shear velocity to the wind speed at a height of 10 meter above the ocean surface u_{10}, so $u^{*2} = C_D \cdot u_{10}^2$. A typical C_D for the open ocean is $1.37 \cdot 10^{-3}$ (Stull 2000).

2.1.3 Surface gravity waves

For the purpose of this study, this section will focus on surface gravity waves which, because of its origin, are also called inertial-gravity waves. The displacement or elevation of the free surface can now be described as:

$$\frac{\partial}{\partial t}\left(\frac{\partial^2 \eta}{\partial t^2} + f^2\eta - gH\frac{\partial^2 \eta}{\partial x^2} - gH\frac{\partial^2 \eta}{\partial y^2}\right) = 0 \qquad \text{Equation 2- 1}$$

The solution for the above equation (Equation 2-1) is in a form of $\eta = \tilde{\eta} e^{i(kx-ly-wt)}$, and admits the trivial solution $u = v = \eta = 0$ unless its determinant vanishes. Hence, in absence of rotation ($f \cong 0$), which means that the rotation can be neglected, and it is a pure case of shallow-water wave where, $> 20H$. The angular frequency w and phase speed c are given as:

$$w^2 = gHK^2 \qquad \text{Equation 2- 2}$$

$$c = \sqrt{gH} \qquad \text{Equation 2- 3}$$

This is the dispersion relation for inertial-gravity waves and it provides the wave frequency in terms of wave number magnitude $\boldsymbol{K}$ (Cushman and Beckers 2011). There is a similarity between gravity waves and the inertial oscillation and hence the name Inertial-gravity waves. For the gravity waves, we get the dispersion relation in sinusoidal form as following:

$$w^2 = gK \tanh KH \qquad \text{Equation 2- 4}$$

$$c = \sqrt{\frac{g}{K}\tanh KH} = \sqrt{\frac{g\lambda}{2\pi}\tanh KH\frac{2\pi H}{\lambda}} \qquad \text{Equation 2- 5}$$

In Summary surface waves travelling from Deep Ocean into shallow waters suffer the following transformation (Kundu and Cohen 2008):

Table 2- 1. Shallow water wave transformation.

Deep-Water	Intermediate-Water	Shallow-Water
$\frac{H}{\lambda} > \frac{1}{2}$	$\frac{1}{20} \leq \frac{H}{\lambda} \leq \frac{1}{2}$	$\frac{H}{\lambda} < \frac{1}{20}$
$c \cong \sqrt{\frac{g}{K}}$	$c = \sqrt{\frac{g}{K}\tanh KH}$	$c = \sqrt{gH}$

For a group of waves: $c_G = \frac{c}{2}\left[1 + \frac{2KH}{\sinh 2KH}\right]$	
$c_G = \frac{c}{2} = \frac{1}{2}\sqrt{\frac{g}{K}}$	$c_G = c$

2.1.4 Wave energy propagation

The surface gravity waves carry with them kinetic energy of the particles motion and gravitational energy associated with vertical displacement (Pond and Pickard 1983). The kinetic energy per unit of horizontal distance is given by the integration over the depth and averaging over a wavelength. The potential energy of the wave system is the work done to deform a horizontal free surface into the disturbed state and is equal to the difference of potential energy of the system in the disturbed and undisturbed (Equation 2- 6) (Kundu and Cohen 2008).

$$E_k = E_p = \frac{\rho g}{2}\overline{\eta^2} \qquad \text{Equation 2- 6}$$

It is shown that for surface gravity waves the kinetic and potential energy are equal, verifying the principle of equilibrium of energy. This however, is only valid when the Coriolis force is neglected. The total energy in the water column per unit of horizontal area is:

$$E = E_k + E_p = \rho g\overline{\eta^2} = \frac{\rho g}{2}a^2 \qquad \text{Equation 2- 7}$$

Another features of the surface gravity waves is the energy flux across a vertical plane which is the pressure work done by the fluid. The average energy flux per unit length of wave crest is:

$$F = \left[\frac{1}{2}\rho g a^2\right]\left[\frac{c}{2}\left(1 + \frac{2KH}{\sinh 2KH}\right)\right] \qquad \text{Equation 2- 8}$$

The first factor has the wave energy. The second factor is the group speed which is the speed of propagation of wave energy of component (Kundu and Cohen 2008).

2.1.5 Waves in shallow water

Waves propagate into shallow water, both small and long waves travel at the same speed in a decreasing water of depth *H*. However, when the bottom depth changes the wave direction and all other wave parameters except period, also change. When the group velocity decreases the wave crests moves further apart and the wave height also decreases in wave energy. By decreasing group velocity near the shore, the wave group crests bulk into each other raising the wave height and leading to a rise in wave energy, this phenomenon is called wave shoaling (Kundu and Cohen 2008,).

Deep water wave travelling to the coast at a certain angle to the coastline, the section of wave in deeper water moves faster than the section in shallow water. This causes the waves change direction to be more parallel to the coastline therefore they become surf. This phenomenon is called wave refraction and is due to the change of wave direction associated with the change of wave phase speed. Ocean waves propagating into shallow waters can also be reflected or diffracted. Wave diffraction occurs when an ocean wave encounters a surface-piercing obstacle. Diffraction causes energy to be transferred along a wave crest, and also cause waves to effect water far of the interfering structure (Kundu and Cohen 2008, Pound and Pickard 1983). If a wave propagates against a rock cliff or a sea wall the wave will be reflected back to the ocean.

2.1.6 Interaction between wind waves and surface currents

The form of surface waves can be significantly altered by currents. These currents can be induced by different mechanisms in the ocean. For example, an important wave-current interaction in the ocean results from the interaction between surface gravity waves with the wake produced by a moving object or vessel (Cooper 1986). Wave-current interaction and the associated effects on wave direction, wave length, and wave height are of concern for ocean engineering applications such as wave energy conversion systems principally in areas of strong tidal currents near bays and rivers. These effects of currents on the waves are also a factor in the development of abnormally high waves in strong western boundary currents such as the Agulhas Current (Earle and Bishop 1984). Surface waves that propagate in the opposite direction from the currents will suffer a decrease in wavelength and an increase in wave height, and at times the wave steepness may increase enough to induce wave breaking and vice versa (Figure 2- 1) (Earle and Bishop 1984). Strong oceanic currents can therefore cause the formation of huge waves. These are characterized by their extreme wave height 1.5-2.0 times the significant waves of the surrounding wave field (Baschek 1999). For wave energy conversion systems, the effect of currents on wave steepness and energy transference between waves and currents are important to access the amount of energy to be captured from the ocean motion. According to Baschek (1999), for deep water waves, the amplitude of the wave in interaction with an oceanic current is given by the following equations:

$$\frac{a}{a_0} = \frac{c_0}{\sqrt{(2u + c)c}} \qquad \text{Equation 2- 9}$$

Where a_0 and c_0 is the amplitude and phase speed of a wave traveling on a current. And, the wave energy is given by:

$$\frac{E}{E_0} = \left(\frac{a}{a_0}\right)^2 \qquad \text{Equation 2- 10}$$

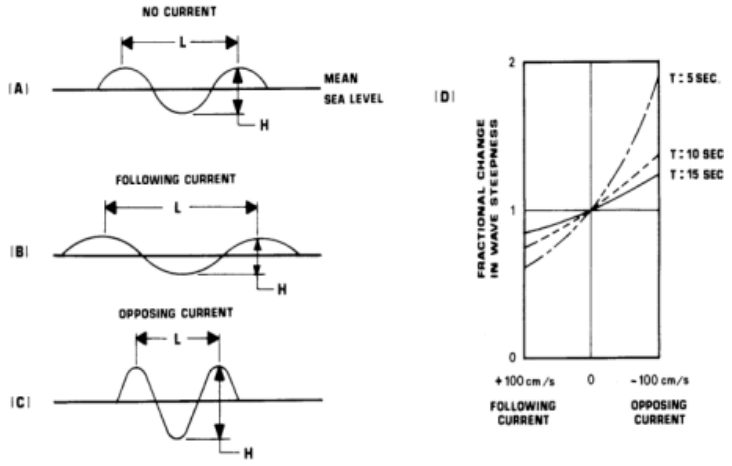

Figure 2- 1. Effects of currents of a simple harmonic wave showing: (a) no currents; (b) following current; (c) opposing current, and (d) the fractional change on the wave steepness (Adapted from Earle and Bishop 1984).

2.1.7 Wave climate spectra

Surface gravity waves in the ocean are basically generated by wind. Thus, the longer the wind blows and the larger the area of ocean blown by the wind, the bigger the waves will be. In ocean engineering projects, it is important to know the wave spectra at a given location by analysing the past and present wind and states.

Real ocean waves do not have the simple regular and precise properties of simple harmonic waves. At a given sea state, surface waves can be expressed mathematically as the sum of simple harmonic waves each with a specific amplitude, wave length, frequency, and direction of propagation (Earle and Bishop 1984). The phase components of the waves are arbitrary distributed over 360° and each component wave travels at a phase speed that depends on its wave length leading to a dispersion of the longest waves ahead of the shortest (Earle and Bishop 1984).

There are various approaches used to build a wave spectrum according to a number of parameters such as wind speed, fetch and modal frequency. The most common are the Bretschneider or ITTC two parameter spectra, the Pierson-Moskowitz Spectrum, DNV Spectrum and the JONSWAP spectrum (Earle and Bishop 1984).

From the wave energy Equation (2- 7), it is seen that the energy is dependent only on the wave amplitude. Thus, a wave spectrum indicates the amount of wave energy at different wave frequencies and it is constructed by plotting spectra density against frequency.

For wave energy conversions purposes, it is necessary to study the directional $S(f,\theta)$ and non-directional $S(f)$ wave spectra. The non-directional spectrum is given by the integral of the directional spectrum over all directions at each frequency multiplied by the directional resolution $\Delta\theta$. Given a function $S(f,\theta)$ as the directional wave spectrum in $[\frac{\frac{m^2}{Hz}}{radian}]$ and after integration the non-directional

spectrum will be given as $[m^2/Hz]$ (Earle and Bishop 1984).

$$S(f) = \Delta\theta \sum_{i=1}^{N} S(f,\theta) = \frac{2\pi}{n} \sum_{i=1}^{N} S(f,\theta) \qquad \text{Equation 2- 11}$$

Where θ is the wave direction ("towards") in radians, N is the number of directional bins.

The wave spectral characteristics

The spectral momentum m_n is the first spectral characteristics directly related to the time series of surface waves (Earle and Bishop 1984):

$$m_n = \int_0^{\infty} f^n S(f) df = \sum_{i=1}^{N} (f_i)^n S(f_i) \Delta f_i \qquad \text{Equation 2- 12}$$

$$m_0 = \int_0^{\infty} S(f) df \qquad \text{Equation 2- 13}$$

$$\bar{T} = \frac{m_0}{m_1} \qquad \text{Equation 2- 14}$$

Where n is positive integer value (n = 0,1,2,…). This is the spectral moment in which can be used to calculate many other time series of wave parameters. The first component of the spectral moment is the m_0 which is the variance of the wave time series.

The modal period T_0 is the wave period corresponding to the maximum wave energy (Earle and Bishop 1984). The mean period of the peaks and the mean zero crossing periods can be written as:

$$\overline{T_p} = \frac{m_2}{m_4} \qquad \text{Equation 2- 15}$$

$$\overline{T_z} = \frac{m_0}{m_2} \qquad \text{Equation 2- 16}$$

The width of the spectrum band ε can vary form $\varepsilon = 0$ if the spectrum is a narrow band and $\varepsilon = 1$ for wide band spectrum. Normally a surface wave spectrum is a narrow band except if we deal with ripples.

The significant wave height H_{m_0} is the average of the highest third of the waves in a random seaway and can also be written as $H_{1/3}$ (Earle and Bishop 1984).

$$H_{m_0} = 4\sqrt{m_0} \qquad \text{Equation 2- 17}$$

$$\text{Z(t)} = \overline{\eta(t_0) \cdot \eta(t_0 + t)} \qquad \text{Equation 2- 18}$$

Where Z(t) is the auto-covariance which measures the time lag (t) of the related surface elevations, and $Z(0) = m_0$.

2.1.8 Wave forecast models

Generally surface gravity waves are generated by two important factors (forcings) that can act together or individually. According to MacHutchon (2006) these forcings are described by two theoretical explanations: (i) the wave incoherent stochastically forcing by random atmospheric pressure fluctuations and (ii) wave coherent forcing by wave induced atmospheric pressure fluctuations proportional to the wave amplitude. Models try to reproduce the reality in which the wave growth is linear in time and thus account for the incoherent forcing unrelated to wave amplitude. Models also incorporate a variance growth exponential in time in order to account for the coherent forcing proportional to wave amplitude. For example the well-known wave model SWAN describes the evolution of the wave spectrum by a spectral balance equation as follows:

$$\frac{\partial}{\partial t}N + \frac{\partial}{\partial t}C_x N + \frac{\partial}{\partial t}C_y N + \frac{\partial}{\partial t}C_\sigma N + \frac{\partial}{\partial t}C_\theta N = \frac{S(\sigma,\theta)}{\sigma} \qquad \text{Equation 2- 19}$$

Where the first term is the rate of change of perturbation density in time, the second and third terms are the propagation of the perturbation in geographic space, the forth term is the shifting of the relative frequency due to variations in depth and current and the fifth term is the depth induced, current induced refraction. The term on the right side of the equation is the source term which in terms of energy density it represents the effects of generation, dissipation and non-linear wave-wave interaction (MacHutchon 2006).

$$S(\sigma,\theta) = S_{in}(\sigma,\theta) + S_{ds}(\sigma,\theta) + S_{nl}(\sigma,\theta) \qquad \text{Equation 2- 20}$$

Where $S_{in}(\sigma,\theta)$ represents the wave energy generation by the wind thus, it models the transformation of the kinetic energy of wind water wave energy and include the wave frequency and direction (A) and wind speed and direction (B) and the following E is the component of the spectral energy density.

2.1.9 Ocean wave measurements

To measure waves with high accuracy, a number of considerations have to be taken into account of, which the most important is to know the purpose of the measurements. According to Earle and Bishop (1984), wave data applications can be divided into two general major groups. The first group requires information on the typical wave conditions that are representative of wave conditions on a monthly, seasonal or annual basis. The second group requires information on extreme wave conditions that are representative of severe wave conditions that occur over long time periods. A typical wave application uses the first group in which wave measurements are usually made for time periods of a few years or less depending on the user needs. Long period measurements are important to calibrate wave models. Measurements in deep water are mostly done by a non-fixed platform, thus accelerometers, submerged acoustic Doppler, pressure sensors and buoys. In shallow waters several options are

available. If there is a fixed platform or pier available then wave staffs, submerged pressure sensors, acoustic and Doppler sensors, wave orbital velocity sensors can be utilized. Insitu recording has the advantage of not requiring telemetry, but the disadvantage is that the loss or failure of sensors and instrument means loss of data. Other disadvantages are the exceeding memory, overcome by doing wave records of ~ 20 min/h or per three to six hours (Earle and Bishop 1984). Telemetry either can overcome this disadvantage.

Wave sensors

Several techniques are used to measure (Figure 2- 2). Briefly these include:

Sea State estimated by observers at sea – is the most common and oldest method for wave measurements. Although this kind of measurement is estimated to be 25% to 50% accurate. It has been used for climatology proposes as a large number of visual observation can be averaged and calibrated (Earle and Bishop 1984).

Wave staffs – this is uses submerged devices attached to a fixed structure such as a pier or an off shore platform.

Subsurface pressure sensors – pressure sensors measure the changing wave-induced pressure beneath waves. As the depth of the sensor increases, the wave pressure fluctuations decrease, and pressure of higher frequency waves with larger wave number are more rapidly attenuated with depth than the pressure for lower frequency waves with smaller wave numbers. The depth below the surface where the sensors can be employed successfully depends on the signal to noise ratio where the signal is the wave pressure and the noise is due to characteristics of the sensor and the transmission, recording and processing data. Normally pressure sensors cannot be used at depth below 30 meters of the sea surface (Earle and Bishop 1984).

Upward looking acoustic and Doppler sensors – are mounted on the sea bed and emit acoustic pulses and receive the echo from the surface. The measurement is based on the time interval between the transmission and reception which determine the varying distance between the sea surface and the sensor.

Buoys – Accelerometers are employed into floating buoys to measure vertical acceleration which is time integrated twice to provide a record of wave elevations. The most accurate measurements are made using an accelerometer stabilized by a gyro so the axis of the accelerometer is always vertical. Most of these buoys use telemetry to send data in real time or near real time to the recorders in shore.

Remote sensing – one fast and relative cheap way of measure waves at a vast spatial scale is to use remote sensing. There are several methods of performing remote sensing wave measurements, which includes the use of land based radars, radars from aircrafts, and radars from satellite. Satellite altimeters are now the most widely source of wave measurements. According to Stewart (2005) and

Earle and Bishop (1984), altimeters were flown on Seasat in 1978, Geosat from 1985 to 1988, ERS-1 & 2 from 1991, Topex/Poseidon from 1992, Jason from 2001, and Envisat. In altimetry a radio pulse from a satellite altimeter is first reflected from wave crests, and later from the wave troughs. The reflection stretches the altimeter pulse in time, and the stretching is measured and used to calculate wave-height with an accuracy of ±10%. The altimeter data are used to produce monthly mean maps of wave-heights and the variability of wave energy density in time and space. These data are also assimilated into wave forecasting models to increase the accuracy of wave forecasts (Stewart 2005). Land or shore based radars constitute a very good way of measuring waves. Ionosphere reflected radar signals has a wide range of 800 to 3000 km, and direct wave reflection radar signals has range of 20 to 70 Km (Earle and Bishop 1984).

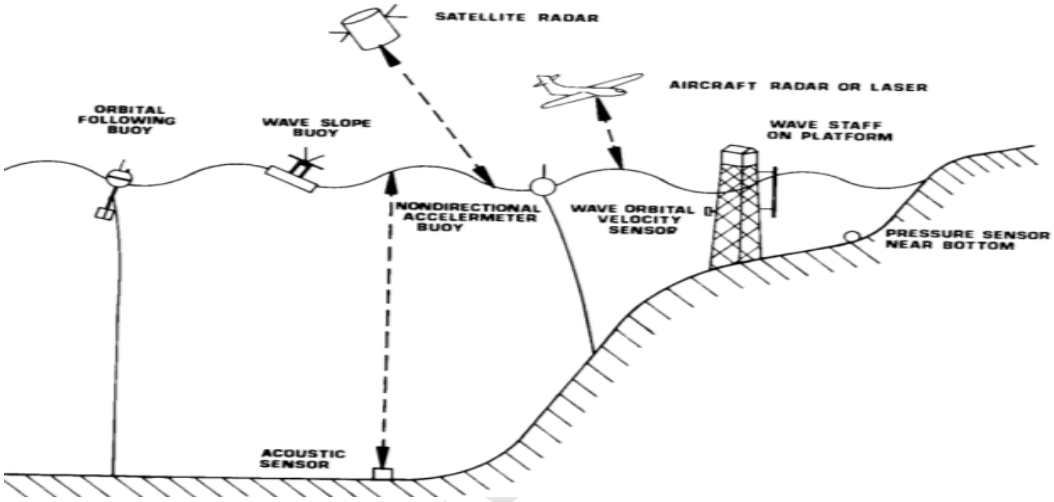

Figure 2- 2. Schematic diagram of various wave measurement systems (Adapted from Earle and Bishop 1984).

2.2 Wave energy

2.2.1 Introduction to renewable energy

The main source of energy in the Earth system is the Sun. Renewable energy sources derived by the power of the Sun radiation is both once the most ancient and the most modern forms of energy used by the Humanity (Boyle 2004).

From the Total energy system on Earth, only 0.02% is currently utilized by human society (Sorensen 2004). From this small portion of energy utilized by human civilization, renewable energy currently provides about 25% or more of the total energy supply in the world. Most of this energy is in form of biomass energy (global average of 222 W/cap), hydro (global average of 50 W/capita), wind and solar and ocean energy contributes with only 0.01 W/cap. Hydropower therefore, constitutes a substantial source, although its use is no longer growing due to environmental limitations (Sorensen 2004).

In theory, the term renewable energy source is the maximum rate at which energy may be extracted in a renewable mode. In other word, it is the rate at which new energy is arriving or flowing into the

reservoirs associated with many of the renewable energy cycle (Sorensen 2004). Renewable energy source is the Sun radiation which is transmitted (but not totally) by the atmosphere and absorbed (but not totally) by ocean and converted into wind and wave energy and distributed over the Earth-atmosphere system through a number of complex processes.

In this study, Ocean Energy (OE) particularly Wave Energy (WE) is the focus. Wind blows over the ocean and transfers momentum into the sea surface generating waves. As the wind is originally derived from solar energy we may consider the energy in ocean waves to be a stored and, moderately high density form of solar energy. Solar power levels typically in the average order of 100W/m^2 can be eventually transformed into waves with power levels of over 100 kW/m (Boyle 2004).

On large or medium time scales, wave is energy a more dependable energy source than wind energy. However, on a seasonal scale, the variations in wind and wave energy are expected to be positive correlated to each other (Sorensen 2004).

Ocean waves located near or within the generation area typically storm waves, and are characterized by forming an irregular and complex sea. However, when the waves travel out of this generation area with a minimum loss of energy they become swell waves at great distances from the origin.

Surface gravity waves generated by the winds loose large quantities of power when they travel onto the continental shelf. The Agulhas Bank is located at the southern tip. This implies that the Agulhas Bank is surrounded by stormy seas, generated by the quasi permanent storm region over the South Atlantic Ocean at about 50° S and the end of the long South Atlantic fetch with winds blowing mostly from southwest.

2.2.2 The global wave energy resource

Wave energy is one of the most predictable and dependable forms of renewable energy. It is fairly well distributed around the world with potential to extract wave power sites available to locations close to settlements.

The Figure 2- 3 shows the estimates of the power density at various locations around the world. Most regions in the mid-latitudes have higher wave energy due to the influence of persistent winds rather that those regions in the tropics where the wind is weak.

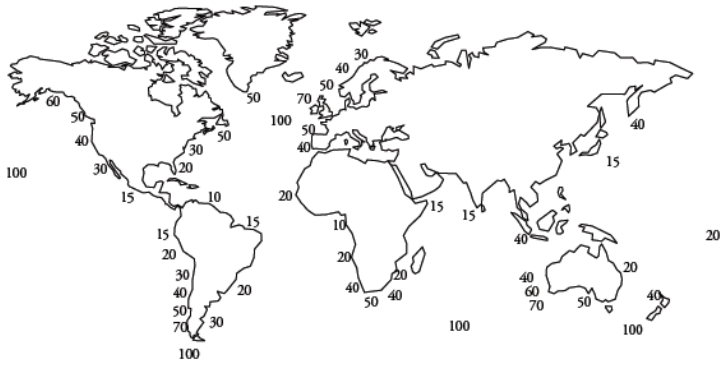

Figure 2- 3. Annual average of wave power density in Kilowatts per meter of wave crest (kW/m) for various locations around the world (Adapted from Thorpe 1999)

2.2.3 Wave power density of the sea surface

To quantify the amount of energy available in a certain region of the ocean, it is necessary to estimate the energy and power density contained in the waves. Energy density of a wave is the mean energy flux crossing a vertical plane parallel to a wave crest. The energy per wave period is the wave power density. The wave power density is also the rate at which the combined potential and kinetic energy of the sea surface would be transferred to the cross-section of any wave energy device in its path or transferred to an array of wave converting devices and its rate of renewable by surrounding wave field (Jacobson 2011).

Wave power density for a regular wave

Wave power density of a single harmonic wave is the rate at which the combined potential and kinetic energy of the wave is transferred through a vertical plane of unit width orientated perpendicular to the direction of the wave propagation and extending down from the surface.

Wave power density for long-crested irregular wave

Long-crested irregular waves are a set of several single waves traveling with different wavelength and speed. This irregular wave can be separated into its harmonic components by harmonic analysis, and each component contributes with a certain amount of the total variance of the sea surface. When this variance is divided by the frequency, it results in a sea surface variance density spectrum or simply wave spectrum. When the total variance is multiplied by the density of the sea water and acceleration due to gravity it then represents the total energy per unit area of sea surface. Wave energy conversion devices are positioned so as to intercept this total energy as it propagates at the group velocity of it harmonic components.

As mentioned before, due to the characteristics of the wind in the real ocean environment, the wave component of short crested irregular waves propagate in different directions at the same time. Therefore, real surface gravity waves are finite in width and continually appear and disappear as the various directional components interfere with one another. The total variance of the short crested

waves is a function of frequency and direction of its harmonic components. By dealing with this concept with a real approach, we can now say instead that the wave power density is the amount of energy that crosses a circle 1 m in diameter in 1 s. importantly this definition now implies clearly that the energy can come from many sides at once.

For each harmonic component of the wave spectrum, the energy the wave energy travel at the group velocity C_G given by the Equation 2- 21.

$$C_G = \frac{1}{2}\sqrt{\frac{g}{k}\tanh(kd)\left(1+\frac{2kd}{\sinh(2kd)}\right)} \qquad \text{Equation 2- 21}$$

Where g is acceleration due to gravity, k is the wave number ($k = \frac{2\pi}{L}$).

The total wave power density or wave energy flux, in watts per meter of wave crest width at any given water depth, is given by:

$$P = \rho g \int_0^\infty C_G(f,H)S(f)df = \frac{\rho g^2}{4\pi} m_{-1} = \frac{\rho g^2}{64\pi} T_e (H_{m0})^2 \qquad \text{Equation 2- 22}$$

Where $T_e = \frac{m_{-1}}{m_0}$, the sea water density is $\rho = 1025\ kg/m^3$ and the acceleration of gravity $g = 9.81\ m/s^2$.The equation of total wave power density will now take the following from:

$$P = 490\ T_e (H_{m0})^2 \quad [Wm^{-1}] \qquad \text{Equation 2- 23}$$

2.2.4 Wave energy flux across a linear feature

The wave energy flux depends on the wave power density of the sea surface, direction of the wave group, orientation of the coastline, bathymetric contours, and national boundaries or other linear feature of reference (Boyle 2004, Jacobson 2011). This quantity indicates that a line or array of wave power converting devices will not intercept all the incident wave power. The absorbed wave power will depend on the angle between the wave crest and each device.

The above theory of energy flux does not apply to all cases. For example, a heaving buoy point absorber absorbs all the wave power density at wide range of incident wave angles, not just when the row is perpendicular to the direction of the waves (Jacobson 2011). Point absorber wave energy converter devices do not absorb all the energy from a given direction, but instead absorb parts of several wave power densities from different angles at the same time. A study done by the *Danish Wave Star (2004)* evaluated the efficiency of an isolated buoy. Their results indicated that for a wave height of 2.5 m and average wave period of 5.5 s the wave power density is 20.2 kW/m. consequently, a 10 m diameter buoy in isolation absorbed 63.6 kW which correspond to 31% efficiency (Jacobson 2011). An

interesting feature is that when the same experiment is conducted using five identical buoys separated by gaps with size which corresponds to diameter of zero to one buoy and with incident angles from 0° to 90°. For example, using the above theory, and for the five buoy scheme described above, the **q-factor** (defined as the wave energy absorbed by the entire row divided by the wave energy that would be absorbed by an individual isolated buoy) the only wave power density available for this row of buoys was the amount incident on the end of the row, would be calculated by assuming the percentage of energy absorbed by each buoy. So the total wave power density would be equal to 31% + 21.4% + 14.8% + 10.2% + 7.0% = 84.4% and dividing by the five times the energy absorption efficiency of an individual buoy, leading to a **q-factor** of 0.54. However, the real **q-factor** is proximately 0.76 for **zero m** gaps and 0.81 for **ten m** gap, all in 0° incident angle (Jacobson 2011). Moreover, models show that the **q-factor** can be even larger if the gaps between the floats were in the range of about 5 to 15 buoy diameters (Jacobson 2011).

The *European Marine Energy Centre in Orkney Islands* had conducted a numerical analysis of a 10 m diameter buoy in directional spectra and the results indicated that when the buoys are aligned parallel to the prevailing wave energy flux direction the array of buoys has its maximum absorption at a buoy separation distance of 25 producing a peak **q-factor** of 1.16 for an array of two buoys and q-factor of 1.14 for an array of 2 buoys in line. The **q-factor**s that have values greater than one, means that the vertical buoy motion are transforming part of the absorbed energy into radiated waves that the next buoy is able to absorb (Jacobson 2011). According to Folley and Whitaker (2009) and Jacobson (2011), an array consisting of ten buoys diameter or beyond, at a separation distance greater than 100 m, then the equivalent **q-factor** will be 1.0, meaning that the buoys in the array receive the same quantity of energy as if they were individually moored as isolated devices. Babarit (2010) described in his report that for two heaving buoys aligned in the same direction as the incident wave energy flux, their interaction is negligible if the gap between them is greater than 200 m. The conclusion of all these analyses is that the wave power density is a quantity which better estimates the available wave energy resource rather the directional wave energy flux.

2.2.5 Available wave energy resources along a linear feature

In order to estimate the wave energy along bathymetric contours or coast line or across the holly region, simply it must be multiplied the wave power density by the distance spanned from one hindcast grid point to its precedent along the same contour to yield the average power for the entire contour. Then the average wave power is multiplied by the appropriate time (in hours) and land scale L in km to yield total available energy in Wh.

$$P_{Tot.Av} = 490\, T_e (H_{m0})^2 \cdot t \cdot L \quad [Wh] \qquad \text{Equation 2- 24}$$

2.2.6 Technically recoverable wave energy resources along a linear feature

This quantity describes the amount of wave power density that interacts with a device or an array of devices moored in the flux pathway of a wave (Figure 2- 4a and Figure 2- 4b). The incident wave power that enters a unit diameter circle can travel according with the following pathways: (i) energy can be reflected by the devices array or radiated by the motion of the devices; (ii) energy can be dissipated as heat and sound by friction between the mechanical elements of the wave power conversion systems or even by fluid friction within hydraulic or pneumatic conversion systems; (iii) Energy can be recovered as electrical energy at the array of devices; (iv) and energy can propagate in between devices or be shed passing through the unit circle (Jacobson 2011).

The power density of a renewable energy system normally can be characterized by only one parameter, for instance, wind, current speed or solar radiation. However, incident wave power density is characterized by two parameters which are the wave significant height and the wave energy period. The characteristics that describe the operating range of a wave energy converter device are namely: the threshold operating condition (**TOC**); the rated operating condition (**ROC**); and the maximum operating condition (**MOC**). Therefore, comparing the operating conditions of others renewable energy sources which only depend on one parameter, the **TOC**, **ROC** and **MOC** of wave energy converting devices must be presented by a tri dimensional matrix.

A device set below the **TOC**, the incident power density is insufficient to motivate the power conversion mechanism, because the device is idle. Under these conditions, no wave energy is withdrawn from the device. The only wave reduction that occurs is due to wave reflected from the device and frictional dissipation by idle device (Jacobson 2011).

Above the **TOC** and bellow the **ROC**, the device start operating and convert wave power into electricity. Within this range, the efficiency of the absorbed energy depends on the significant wave height and on the wave energy period. Moreover, between **TOC** and **MOC** the power depends more on the wave height rather than on the period (Jacobson 2011).

The range above the **ROC** but below the **MOC**, the device operates at a rated capacity and generates a constant power output (Jacobson 2011). In this stage, the device must avoid absorbing excessive energy levels that can damage the power conversion mechanism. Thus, when the wave power density increases above the **ROC** the device becomes inefficient capturing less energy by shading power (Jacobson 2011). The setup of the wave converting devices in terms of operational characteristics (principally the choice of **ROC**) involves a balance between under-utilization of capital investment and excessive shading of available power. Thus a lower **ROC** means a higher capacity factor, which means a lower capital investment for a given annual energy production, but it means a lower technical recoverable resource (Jacobson 2011).

Above the **MOC**, the device enters in survival mode and stops the conversion mechanism. Note that the survival mode puts the device parked minimizing the wear and tear of the system, reducing maintenance and repair costs. It also reduces mooring and structural loads (Jacobson 2011). In this standpoint the device is designed to be more passive to the incident waves when it is at the parked state rather than when it is operating.

Knowing the **TOC**, **ROC** and **MOC**, is possible to estimate the percentage of technical recoverable energy resource for a given site. The cumulative probability distribution analyses can be done to estimate the fraction of total annual available wave power density resource as a function of significant wave height. For example, **TOC** for a given region can be selected depending on the wave climate of each site. If **TOC** = 1 KW/m – it corresponds to a mild wave climate where the annual wave power density is below 10 kW/m. If **TOC** = 2kW/m – it corresponds to a moderately energetic wave climate where the annual wave power density is above 10 kW/m but below 20 kW/m. And if the **TOC** = 3 kW/m – it corresponds to a highly energetic wave climate where the annual wave energy density is equal or above 20 kW/m (Jacobson 2011).

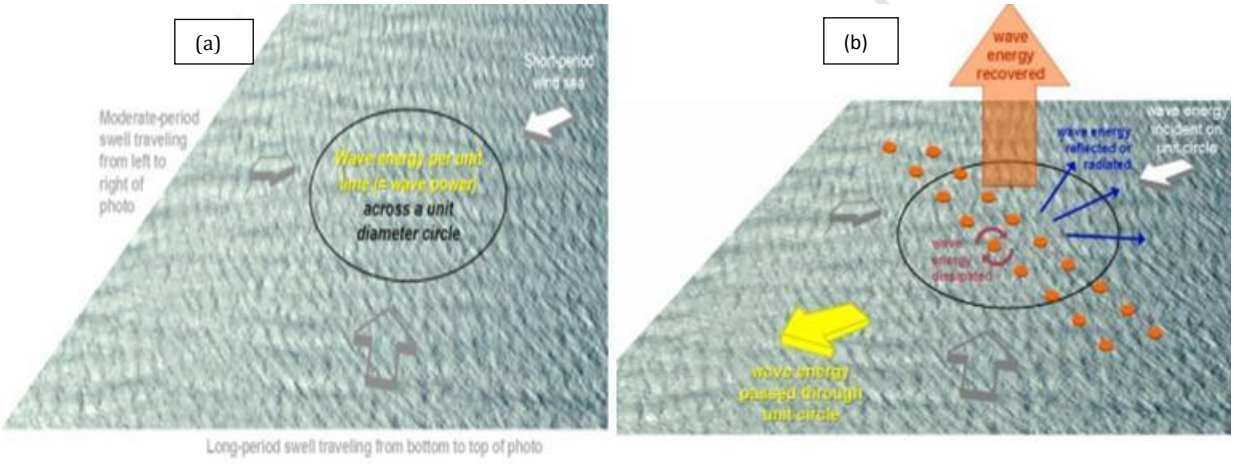

Figure 2- 4. (a) Illustrative diagram of the available wave power density for a three-partition wave field (Jacobson. 2011); (b) Illustrative diagram of the recoverable wave power density (Adapted from Jacobson 2011).

2.2.7 Wave reduction as a function of distance array of floats

When modelling an array of devices as a single large obstacle in the path of direction of propagation of waves, it is observed that the obstacle will absorb or reflect a certain percentage of incident wave energy and will transmit the balance (Smith et al 2010, Jacobson 2011). In this case, is assumed that the transmission of wave energy trough the obstacle is simulated as a proportional decrease of wave energy at all frequencies of the wave spectrum (Jacobson 2011). Figure 2- 5 shows the pattern of wave height reduction for a swell spectrum with a directional spectrum of 10° and a wind sea spectrum with 30° directional spectrum spreading. The obstacle is 30 km wide and absorbs 10% of incident wave energy and transmits 90%. Diffraction of wave energy behind the obstacle eventually restores significant wave height to 99% of its incident value. And this is also observed in very large obstacles. Although the down-wave distance at which wave recovers its full height depends on the obstacle width. According to Jacobson (2011), for an obstacle of 3 km of width, the significant wave height is restored to 99% of its incident value at a down-wave distance of about 50 km, for an obstacle width of 15 km, the down-wave distance will be about 150 km. studies reveal that the wave never recover 100% of its height after interacting with an obstacle due to energy spreading to the surrounding area.

The wind-wave and current interaction add more energy onto the sea state enabling wave height recover over a shorter distance and time. For example, for a cross wind of 10 m/s, the down-wave distance would reduce from 150 km to 70 or 80 km. And if wind speed were 20 m/s, it would add the same amount of energy to the surrounded area as locally withdrawn by 90% transmitting obstacle, thus enabling the significant wave height to recover 100% of its incident value by 150 km (Jacobson 2011, and Smith et al 2010). Torch et al (2010) simulated numerically the wave reduction and recover (Figure 2- 6). He used a full scale 2 km wide by 4.5 km long wave basin, with a device width of 36 m. The gaps between the devices ranged from two times the device width 2D to twenty times the device width 20D. Due to the device width, each device only absorbs 45% of the incident wave energy, so the total wave power density absorbed by the entire array is 19.3% for a 2D gap, 12.3% for a 4D gap, and 9.0% for a 6D gap. At the widest gap which is 6D the wave height is 95% recovered. For a scheme of wave converting devices which does not transmit any energy behind them, the wave height recovers rapidly with help by lateral spreading of wave energy from the surrounding area. The recover depends on the directional spreading of the incident wave spectrum (Beels et al 2010). The wave height recover is directly proportional to the directional spreading. After all these analysis, it seems like for an array of heaving boy point absorber devices which is positioned aligned with the local depth contours so that the long dimension of the array is aligned with the bathymetric contours and the short dimensions of the array extends onshore to offshore. The components of directional wave energy flux that are incident on the shorter dimension side of the array will recover in 99% of its incident value within less than 100 m distance from one buoy to the next and 500 m to 2.0 km from one array to the next, even in narrowly-spread swell. Moreover the refraction of the long swells will

align most of the directional wave energy flux normal o the long dimension of an array. Local wind driven sea would be the quantity aligning to the shorter side of the mooring.

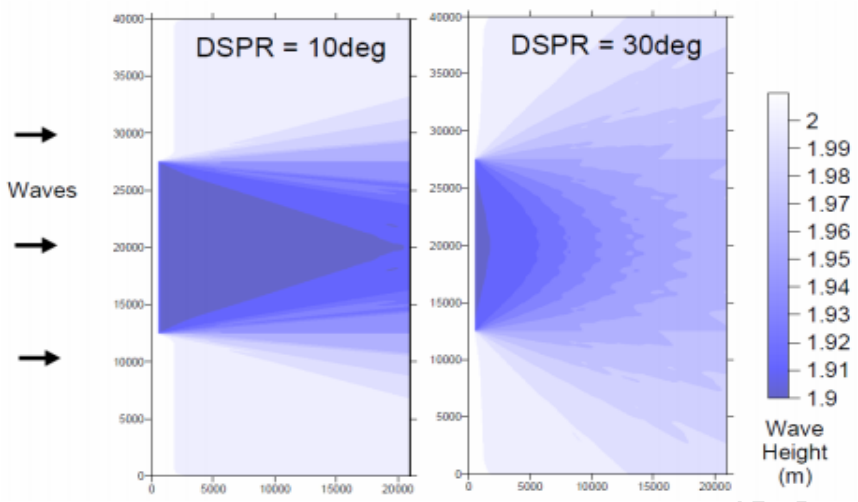

Figure 2- 5. Wave height reduction for 90% transmitting obstacle with 15 km of width located in the path of the 2 meter high wave propagation for different angles of directional spreading (DSPR). According to Jacobson (2011) in the immediate wake of the obstacle the wave height is reduced by 10 cm., and as the energy is proportional to the square of the wave height, 10% energy withdrawal corresponds to 5% reduction in significant wave height (Smith *et al*. 2010) (Adapted from 2011).

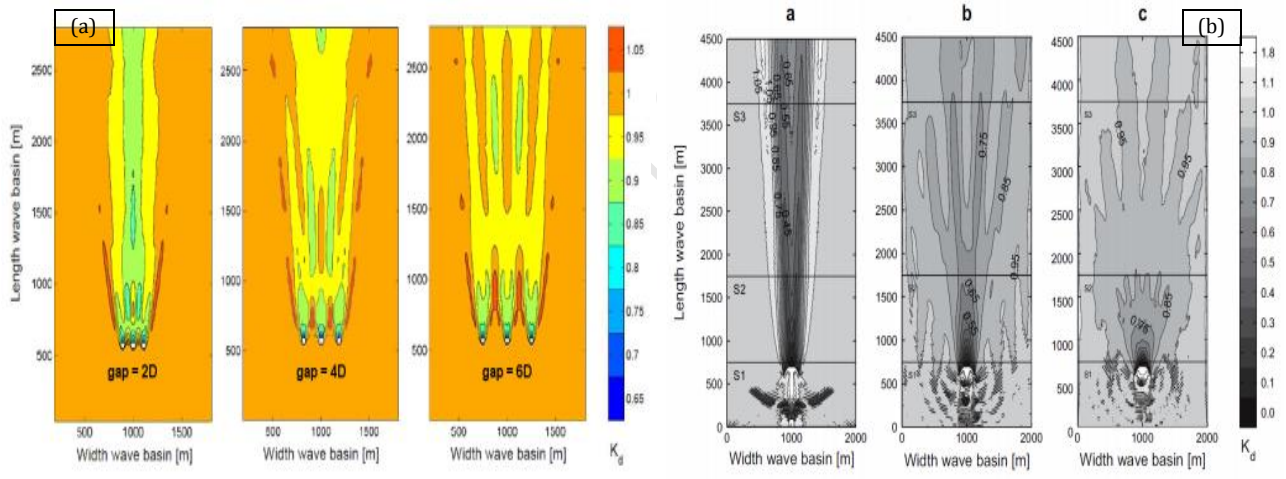

Figure 2- 6. (a) Here D=36 m, and the devices were exposed to long crested irregular waves with significant height of one meter ad peak period of 5.2 s (Troch et al 2010); (b) Simulation of a single device with width of 260 m, exposed to irregular waves of 1.0 m and peak period of 5.6 s: **a** long-crested waves; **b** directional spreading of 9° (long travel swell); **c** directional spreading of 24° (local wind driven seas) (Adapted from Beels et al 2010).

2.2.8 Wave energy converting technology

Wave power technologies are meant to extract the kinetic energy from surface waves and/or from subsurface pressure fluctuations and convert this energy into useful work such as electricity, sea water desalinations, sea water pumping etc.

Wave energy is generally environmental friendly when the site selection and design is appropriate. This form of energy does not directly generate emissions or waste compared to the traditional fossil and nuclear fuels. Moreover, wave energy is generally more predictable than solar and wind energy and carries zero continuing fuel cost (EPRI 2004).

As described before, when waves propagate past a stationary position, the height of the free surface changes, changing the kinetic and potential energy and the water near the surface moves. The pressure under the surface also changes. Several devices for converting wave energy to shaft power or compressions have been developed and deployed. According to reports from the Centre for Renewable Energy Sources, over a thousand wave energy conversion techniques are patented worldwide. Wave energy converters can be grouped into a few general types.

Heaving devices – these can be floating or submerged. They provide a heave motion that is converted by both or either mechanical and hydraulic systems in linear or rotational motion for driving electrical generators.

Pitching devices – these consist of a number of floating bodies, hinged together across their beams. Here the relative motions between the floating parts are used to pump high-pressure oil through hydraulic motors, which drive electrical generators.

Surging devices – these devices exploit the horizontal particle velocity in a wave to drive a deflector which generates a pumping effect facing the wave front.

Overtopping devices – these devices can be floating or fixed to the shore. They collect the sea water from incident waves in an elevated reservoir to drive one or more low head turbines.

Oscillating Water Columns (OWC) – these systems are placed partially submerged hollow structures open to the seabed below the water line. Air inside the structure is alternatively pressurized by the heave motion of the sea surface, generating a reciprocating flow through a turbine installed beneath the roof of the device.

Wave power converters can also be classified in terms of their location, thus, they can be: (i) fixed to the seabed, generally in shallow waters; (ii) floating offshore in deep water, or; (iii) tethered in intermediate depth (Boyle 2004). They can be also classified in terms of their geometry and orientation such as: (iv) terminators that have their principal axis parallel to the incident wave front i.e. they physically intercept the wave; (v) attenuators that have their principal axes perpendicular to the wave front so that wave energy is gradually drawn towards the device as the wave moves past it; or (vi) point absorbers that also work by drawing wave energy from the sea water beyond physical dimensions (Boyle 2004). Point absorbers are mostly slim vertical cylinders that execute vertical movements in response to the waves (Boyle 2004). This relative motion is used to drive electromechanically or hydraulic energy converters.

2.2.9 The worldwide implemented and commercial wave energy converting technologies

The oscillating water column (OWC)

This wave energy converter device consists of a chamber with opening to the sea below the waterline (Drew *et al*. 2009). It is mostly made of concrete and is built into the shoreline (Figure 2- 7a) and works as follows: when waves approach the device, sea water is forced into the chamber exerting hydraulic pressure on the air within the chamber. The air then passes through a turbine. As the wave retreats seawards, the air circulates through the turbine in the opposite direction. Normally this system uses low pressure turbines which rotate in the same direction irrespective of the air direction (Drew et al 2009, and Rodrigues 2012). This device is rated to supply from 20 kW to 4 MW of electricity (CRES 2002, Enciso 2009, and VOITH 2012). The advantages of OWC systems include the near shore location which provides easy access for operation and maintenance, and also reduces transmission costs. However because they are placed nearshore, they convert less energy compared with off shore placed systems.

LIMPET

This is the first commercial grid connected wave energy converting system. It is a 500 KW system developed by the Queen's University of Belfast and WAVEGEN Ltd in the United Kingdom. It has been operating on the west coast of Scotland since 2000, and is also operating in Portugal. The LIMPET is an OWC with 35% efficiency (Figure 2- 7a) (Thorpe 1999). Its dimensions are 21 x 7 m and are installed in areas with 6 m water depth. It has an average resource of 20 KW/m.

WAVEDRAGON

The WAVEDRAGON is a nearshore floating overtopping device comprising two parabolic reflecting arms, a curved ramp, a storage basin and turbines. The incident waves are channelled by the two arms to an overtopping ramp and into a basin placed above the water level. The water from the basin (with a storage capacity of about 5 000 to 14 000 m^3) is channelled through the turbines which generate electricity (Figure 2- 7c). This system is made from steel and concrete, and can align its self to the incident wave direction. The WAVEDRAGON is rated to convert 4 to 11 MW depending on the dimension which can vary from 269 to 390 m of width and form 150 to 220 m of length (Beels et al 2011). It is designed to operate at water depth greater than 25 m.

PELAMIS

PELAMIS is an attenuator device in a cylindrical frame which is subdivided into four sections linked together by a hydraulic power conversion system. The power is generated by the conversion of energy created by the relative movement between each section which drives the digitally controlled hydraulic conversion system. The body of this calendric system has a diameter and length of 4 m and 50 m

respectively (Figure 2- 8a). This device has been tested on the coast of Portugal and is rated to produce a maximum power of 750 KW per unit (Pelamis Wave power 2012).

AQUABUOY

This system is relative simple and is an efficient point absorber (Figure 2- 9a). By floating within the water column, it moves relative to a submerged reaction tube which contains a piston. The piston drives an elastic pump, and then an accumulator levels the power output. The pressurized water from the pump is channelled to an electric turbine generator. The buoy has a diameter of meters and the submerged section of the device is about 30 m in length. It has a power converting rate of 250 KW and can be moored in water depths greater than 50 m (OPT 2012).

POWERBUOY

This is a point absorber device which works similar to AQUABOY, although it is rated to convert 150 KW per unit (Figure 2- 9a). According to the manufacture Ocean Power Technologies (OPT), it can be configured in arrays of 50 to 100 MW or even more. POWERBUOY can be moored at any depth greater than 55 m and can produce power with waves as low as one 1 m of significant wave height. It has similar dimensions as the AQUABUOY and costs (OPT 2012).

Archimedes Wave Swing (AWS)

The ASW is a point absorber WEC that consists of a submerged buoyant cylinder, moored to the seabed (Figure 2- 9b). The wave motion moves an air filled upper casing against a lower fixed cylinder. The vertical movement is converted into mechanical energy and then converted into electricity by a linear generator converter (Rodrigues 2012 and Thorpe 2003). The full scale device (AWS III) will measure ~ 16 m x 8 m deep within a circular structure of 60 m diameter with a total weight of 1300 ton and will be configured to depth over 10 m. The AWS is rated to deliver from 690 kW up to 2 MW and the AWS III will deliver over 2.5 MW (Costa et al 2005 and AWS 2012).

CETO

CETO is a point absorber device which converts ocean energy into renewable power and desalinated freshwater. It was developed by Australian Carnegie Wave Energy Limited and has been successfully tested in Australia and is now going commercial. It is a fully submerged, pumping technology that drives water onshore therefore generating power by a standard reverse osmosis system. Submerged buoys are moved sideways by the ocean waves, driving pumps which pressurize freshwater that are delivered ashore by a subsea pipeline (Figure 2- 10a). Once onshore, the high-pressure freshwater is used to drive hydro turbines, generating electricity. It is rated to 78 KW per unit.

Oyster

The *Oyster* is a surge WEC which consists of a wide buoyant bottom-hinged oscillating flap that completely penetrates the water column from above the surface to the seabed (Whittaker et al 2009). The wave motion forces the flap to move sideways which drives hydraulic pistons. Then pressurize the water and pump it to shore through pipelines where the onshore hydroelectric plant converts the hydraulic pressure into electrical power via a Peloton wheel. This turns a 315 kW electrical generator (Figure 2- 10b). From here, the water passes back to the device in a closed loop via a second low pressure return pipeline (Cameron et al 2010). *Oyster* harnesses the energy of near-shore ocean waves and is designed to operate in water 10 to 12 m deep. This device is made up of a power connector frame (PCF) weighing 36 ton which is bolted to the seabed by 1 x 4 m concrete piles that are drilled 14 m deep into the seabed. It has a power capture unit (PCU) weighing 200 ton comprising 18 x 12 x 4 m buoyant flap hinged to the PCF. The new generation of *Oyster*, the *Oyster* 2 delivers 2400 kW of electricity and costs ~ R 56 million. It will be capable of supplying 12 000 homes with electricity (Andrew 2012).

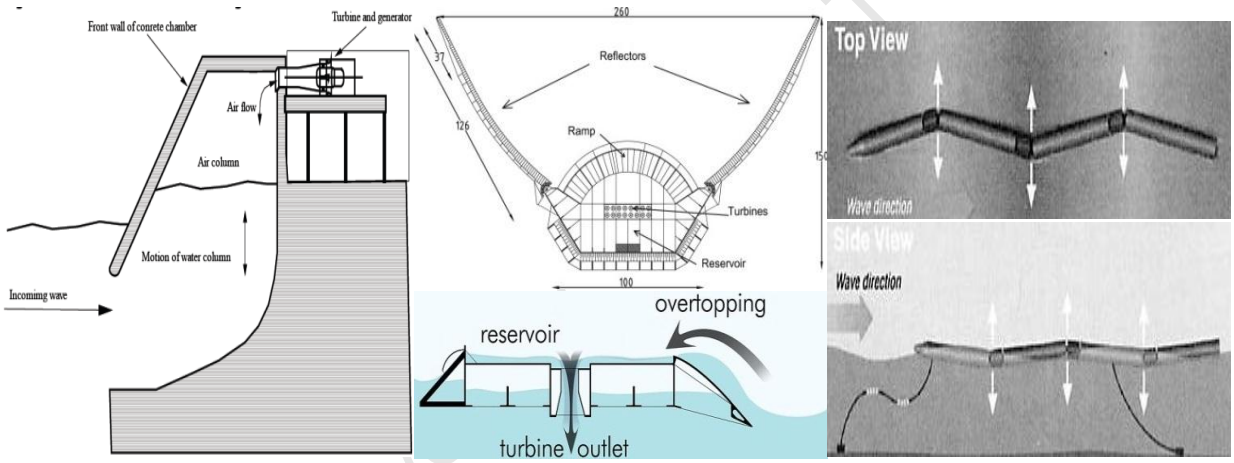

Figure 2- 7. Shoreline and Nearshore WECs: (a) Diagram of an OWC (Adapted from Thorpe 1999); (b) Diagram of WAVEDRAGON (Adapted from Beels et al 2011); (c) Diagram of Pelamis WEC (Adapted from Pelamis Wave Power 2012).

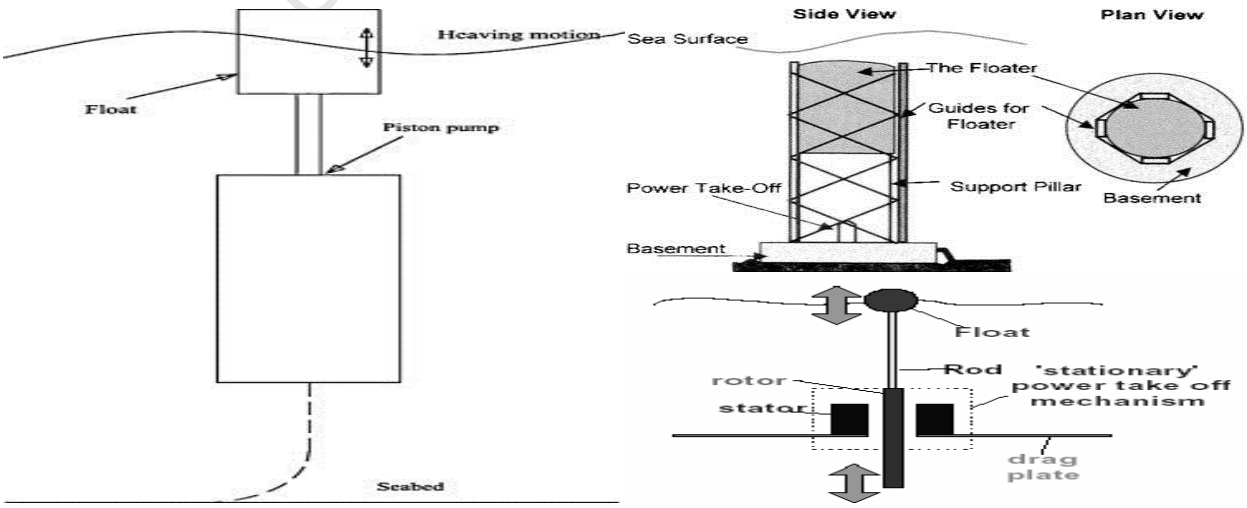

Figure 2- 8. Offshore point absorbers WECs: (a) Diagram of a point absorber WEC (Adapted from Zibihian and Fung 2011); (b) Diagram of AWS (Adapted from Clément et al 2002);

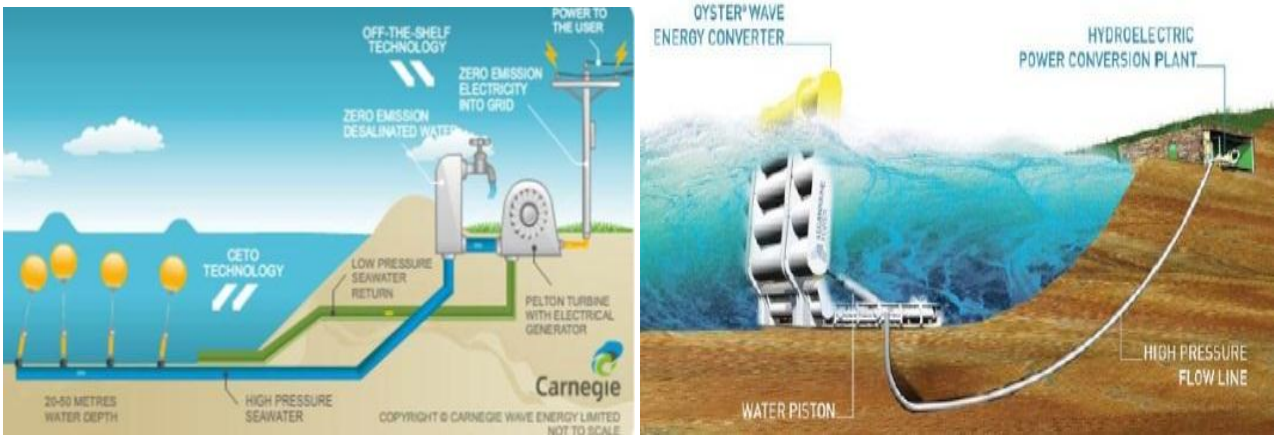

Figure 2- 9. Nearshore point absorbers pumps: (a) Diagram of CETO system (Adapted from Canergie Wave Energy 2009); (b) Diagram of Oyster WEC (Adapted from the ENEC 2012).

2.2.10 Implementation of WECs in South Africa

The Stellenbosch Wave Energy Converter (SWEC) developed by the Stellenbosch University is a 5 MW rated submerged attenuator (Figure 2- 11). This system similarly functions on wave height and comprises a pair of pre-fabricated 300 m of length concrete collectors coupled in a V-format each at an inclination angle of 30° with respect to the shore. These collectors connect to an air turbine and power generator placed above the water level. The power is generated by pressurized air produced by the oscillation of collectors sent to a power generator. This entire system is located at 1.6 km from the shore and built on the seabed where the water depth is about 15 to 20 m. The vision is to cover 40 km stretch of coastline with this kind of device to produce 770 MW. Retief (2007) estimated a cost between R 60 to 75 cents/kWh and ~ R 1 million per unit.

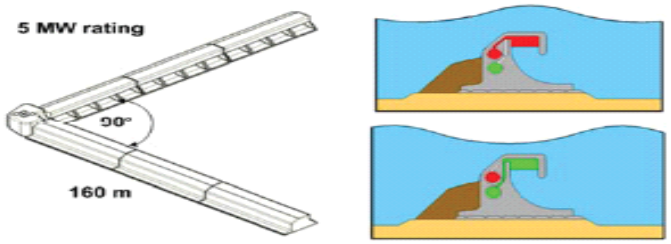

Figure 1: Layout of the SWEC and its operational principle

Figure 2- 10. The SWEC concept (Adapted from Retif 2007).

2.3 South African wave climate

2.3.1 The global atmospheric circulation

A good understanding of the atmospheric processes in the southern hemisphere particularly in the mid-latitudes of the South Atlantic and South Indian Ocean is indispensable to better understand the wave climate and distribution on the Agulhas Bank.

Due to the Earth's geometry, the tropics are warmer than the poles. The annual average solar radiation is greater near the equator than at the poles. This difference is compounded by the fact that the Polar Regions are covered by ice and snow and therefore the albedo in these regions is very much greater than from the tropical regions. The tropical regions therefore receive more energy from the Sun than they emit back to space. To balance the heat budget in the whole system, there must be a process that transports the excess energy from the tropics to make up the deficits in the high latitudes. This difference of heat content between the latitudes creates heat and pressure gradients that lead to wind cells (Nicholson and Flohn 1980).

Essentially there are three regional wind cells on the Earth, namely the Hadley cell, the Ferrel or Mid-latitude cell and the Polar cell. The Hadley cell is a direct thermal cell that initiates in the equatorial low pressure areas where the warm moist air is lifted up to the troposphere and driven polarward. At about latitudes 30° S/N, it descends into a high pressure area with part of the descendent colder air driven towards the equator along the earth surface closing the loop and creating the trade winds. It is important to mention that the flux of the air into this cell is affected by the Coriolis Effect. Furthermore, the position of these cells varies seasonally, although the variations are not much pronounced. The Ferrell cell is located in the mid-latitudes between the Hadley cell and the Polar cell and is associated with the southern westerlies. In this cell the upper level winds are essentially westerly with the surface winds varying in direction. A high moving equatorward and a low moving poleward maintains or even accelerate the westerly flow. An important feature of the Ferrell cell is that it results from the movement of air masses and their relation to the location of the jet stream. The surface movement of the mid-latitudes air masses are somewhere between latitudes 30° and 60° S/N, but the upper flow is not well defined (Nicholson and Flohn 1980). The polar cell is as simple as the Hadley cell and is located between latitudes 60° and 90° S/N. In this cell, relatively warm air rises at 60° S/N and flows poleward through the upper troposphere and when the air masses reach the polar areas it descends as a cold and dry high pressure area, then moves away from the poles along the Earth's surface, but is strongly turned by the Coriolis effect to produce the polar easterlies.

2.3.2 Southern Africa atmospheric circulation

The sea level pressure field (**SLP**) over the Southern Hemisphere is characterized by a maximum in the subtropics, a minimum in the subpolar regions and another maximum in the polar zone. The pressure fields vary seasonally. In winter low pressure centres located at the subpolar regions at about 60° S to 70° S are about 4hPa less than in summer (Hurrel et al 1998). Moreover, the location of the hemispheric low pressure belt known as the circumpolar trough (CPT) also varies seasonally. The circumpolar trough moves poleward and also deepens during the austral summer (December, January, and February). During the austral winter it moves towards the equator and weakens. According to Hurrel et al (1998), the meridional pressure gradients in the middle and high latitudes reach a maximum during the spring and autumn implying that the **SLP** in these regions is minimum during summer and winter. The above differences in pressure fields lead to geostrophic winds. These geostrophic winds are mostly horizontal and westerlies. The seasonal variability in pressure fields have causes the wind pattern to similarly vary. The surface winds in the Southern Africa and South Atlantic region are therefore, stronger during the austral winter (White and Tyson 1988). Moreover, the peak in wind intensity in this region is reached around 30° S in the winter and the contrary occurs around 50° S during the summer.

The climate over the Southern Africa region is highly influenced by the Indian and Pacific Oceans (Reason et al 2006). Reason et al (2006) also highlighted some clear examples for parts of Southern Africa where the Atlantic influence is significant, if not dominant and is related to the variability in the intertropical convergence zone (**ITCZ**), the South Atlantic anticyclone and the midlatitude westerlies. The most important interannual mode for the southern Africa is the El Niño-Southern Oscillation (**ENSO**), while the Southern Annular Mode (**SAM**) is the leading pattern in the mid to high latitudes (Kidson 1988, Thompson and Wallace 2000). The Antarctic Circumpolar Wave is also a significant feature of the mid- to high latitude climate, at least during certain decades. As yet, no evidence exists of its influence on southern African climate (White and Peterson 1996). **ENSO** is known to project strongly over Southern Africa and the South Atlantic, and tends to enhance the temperature and pressure gradients. This arises from changes in the regional atmospheric circulation, primarily via the local Walker circulation and the South Indian convergence zone (Cook 2000, 2001). Additionally Reason et al (2006) suggest that on top of the influence on mid- and high-latitude atmospheric circulation over the South Atlantic, **ENSO** also influences the South Atlantic convergence zone (**SACZ**) mainly during the austral summer. It also influences the jet stream and generation of midlatitude depressions, which can then impact on the development of tropical–extra-tropical cloud bands over southern Africa (Reason et al 2006).

2.3.3 Wind patterns

As mentioned in section 2.3.2, the southern region of South Africa (including the Agulhas Bank) is a region under influence of two different weather systems namely, the moist subtropical wet summer climate to the east and the north and the Mediterranean climate in the south to southwest of this region. The winds on the Agulhas Bank are mainly parallel to the coastline. The north-easterly winds have the greatest seasonality with > 40% occurrence frequency in (the austral) summer, declining to 25% in winter (Lutjeharms 2006, Schumann and Martin 1991). Average speeds for these north-easterly winds at the centre of the Agulhas Bank are > 4 m/s in summer but only 1.5 m/s in winter (Lutjeharms 2006). The south-westerlies winds have an inverse seasonal occurrence compared to north-eaterly winds with the average wind speed around 4 m/s. this means that on the eastern Agulhas Bank, the most frequent and strongest winds are from the east in summer and from the west in winter (Lutjeharms 2006). The wind pattern on the Agulhas Bank has been shown to be related to global **ENSO** and other perturbations (Lutjeharms 2006, Schumann 1992). Wind patterns on the Agulhas Bank are also influenced by coastal lows (due to the topography effects; (Lutjeharms 2006, Gill 1977)) mostly associated with cold fronts that move from west to east. These coastal lows move along the S coast with periods of 2 to 5 days and propagation speeds of 14 to 20 m/s. Analyses of the climatological variability of the major winds axes along the coast of the Agulhas Bank (Schumann et al. 1991) has shown a distinct spectral peak at 6 days. The wind pattern on the western side of the bank is different from those from the central and east side. In the Western Cape, the winds are mostly seasonally and from the southeast with an 80% occurrence in summer and an 40% occurrence in winter with average wind speeds “4 m/s” and only “1.5 m/s” in winter respectively. The north-westerly winds are more prevalent in winter with a constant average speed of about 3m/s (Lutjeharms 2006).

2.3.4 Description of the South African wave climate

The wave climate in this region is associated with local or regional wind patterns and conditions. The major wave-generating system that results in high waves along the South African coastline is the west to east passing of cold fronts with their associated low pressure systems that pass just to the south of the continent (Rossouw et al 1982). These fronts together with two south permanent high-pressure systems (the South Atlantic High off the west coast and the South Indian Ocean High off the east coast) totally dominate the wave generating forces in the oceans surrounding the southern tip of the continent. These low-pressure systems normally shift towards the south in summer and towards the north in winter so that high waves along the South African coast occur more frequently in winter. On some occasion, however, these fronts move far enough northward in summer to cause large waves at the Agulhas Bank (Rossouw et al 1982). Tropical Cyclones and storms moving down the Mozambique Channel can also contribute to the wave climate on the South African coast.

The South African wave climate is characterized by high intensity storms and has seasonal variability which varies in intensity and direction around the coast (Theron et al 2010). The southwest region of the South African coast has the most severe wave conditions, with the magnitude of the waves decreasing from west to east. This means that the highest waves tend to concentrate on the Agulhas Bank. The wave period distribution remains constant along the coast due to the swell propagation northwards. The wave direction is predominantly from the southwest, but is more toward south and south-easterly on the east coast (Theron et al 2010).

Chapter 3

Data and Methods

3.1 Study area

3.1.1 The Agulhas Bank

The Agulhas Bank (Figure 3- 1), is a triangular shaped part of the continental shelf S of South African (34° S to 37° S; 17° E to 27° E). It is ~ 1 000 km in length and 250 km wide at the apex. The shelf drops steeply to 50 m near the coast and then gradually drops to the 200 m contour. At 200 m the shelf then breaks steeply and drops to depths of 4 000 m (Lutjeharms 2006). Approximately 60% of the Agulhas Bank consists of hard substratum with high profile reefs occurring both near the coast of and offshore S of Cape Agulhas (Hutchings 1994).

This large bank is a physical boundary that separates the Agulhas current on the east from the Benguela Current on the west coast. The Alphard Rise, where the shelf is widest, constitutes the border between the western and the eastern Agulhas Bank (Lutjeharms 2006). These two sides of the bank are very distinct from each other. On the eastern side of the Agulhas Bank, the warm water of the Agulhas Current follows the shelf edge, then the current start to meander near Port Elizabeth. These meanders cause cyclonic shear edge eddies and attendant warm plumes (Lutjeharms 2006) which propagates westwards into the Atlantic Ocean as warm core rings. On the other side, the western side, the Benguela Current flows equatorward.

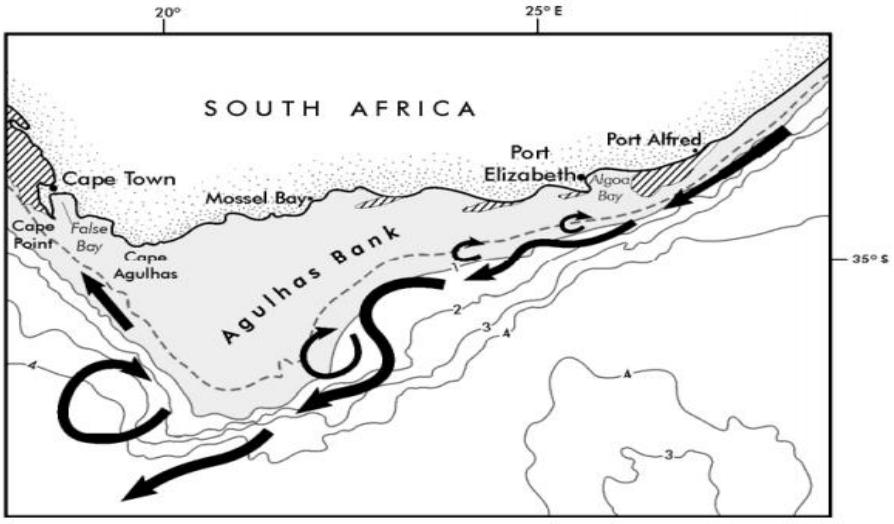

Figure 3- 1. Bathymetry and circulation offshore of the Agulhas Bank. The 200 m isobath represented by the dashed marking the edge of the continental shelf. Prevalent upwelling cells shown by the shading (Lutjeharms 2006)

3.1.2 Characteristics of the four selected mooring sites

Moorings were deployed at four sites across the Agulhas Bank at depths of ≈ 80 m (Figure 3- 2). There have been given geographical names for ease references.

Cape Agulhas – situated off Cape Agulhas. This site is characterized by notable high waves and strong wind. The coastline in this region is mostly rocky. The width of the continental shelf is about 200 km. The mooring site is about 30 km offshore in a depth of ≈ 80 m.

Mossel Bay – this location is situated in the middle of the Agulhas Bank and is characterized by Westerly and Easterly winds in winter and summer respectively. Here the coastline is also mostly rocky. The continental self is also wide and flat bathymetry. The mooring was deployed in a depth ≈ 80 m located 27 km from the coast.

Tsitsikamma – this mooring was deployed in the Tsitsikamma National Park and. At this site, the mooring was deployed 4 km from shoreline in a depth of ≈ 80 m. The bathymetry at Tsitsikamma is a mixture of sand sediments and rocky reef (Fleming et al 1998).

Cape Recife – is situated on the eastern side of the Agulhas Bank. Here the width of the shelf is narrower with the shelf edge being some 70 km offshore. The mooring at this location was deployed near to the shore some 5 km from the shoreline where the water depth was 80 m.

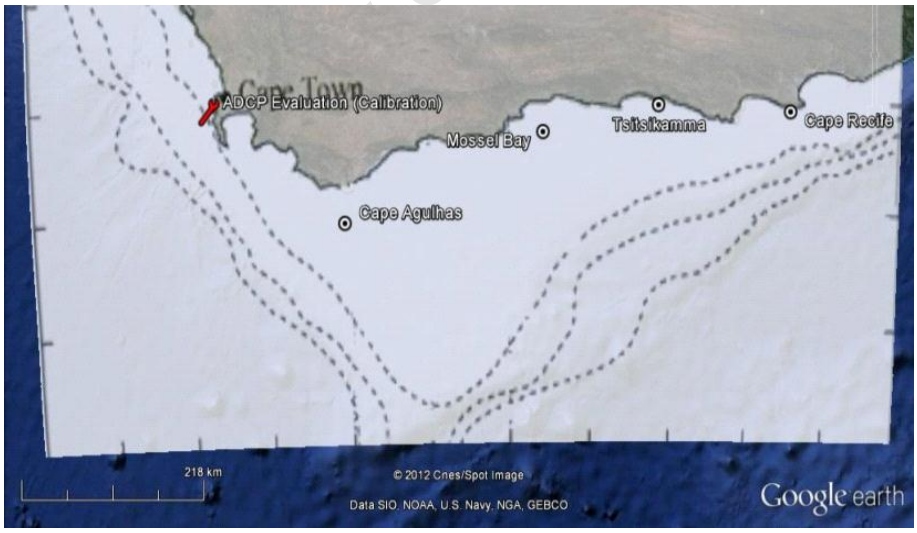

Figure 3- 2. Map of the Agulhas Bank showing the four mooring sites referred to as Cape Agulhas, Mossel Bay, Tsitsikamma and Cape Recife (Adapted from Google Earth 2012).

3.2 Wave data

To quantify the wave field across the Agulhas Bank, insitu wave data were acquired using Acoustic Current Doppler Profilers (ADCPs). Reanalysis data from the National Center for Environmental Prediction (NCEP) – WAVEWATCH III as well as satellite data from AVISO were used to analyze both the spatial and time domains.

3.2.1 ADCP dataset

In situ data were collected by the Operational Oceanography Group of the Bayworld Centre for Research and Education BCRE). "*Nortek AWAC* (Acoustic Wave and Current profiler)" were used to collect the data. The device characteristics and specifications are shown in Appendix A, Table 3- 1.

The AWAC measures wave height and period using the unique acoustic surface tracking (AST) feature. A short acoustic pulse is transmitted vertically toward the water surface, and the time lag between the transmitted ping and its reflection is used to generate a time series of the surface elevation. The AST feature is based on echo-ranging to the surface with the vertically oriented transducer. This method of measuring waves circumvents the depth limitations imposed by bottom mounted pressure and velocity measurements. The AST also gives the ability to derive wave parameters based on times series analyses, meaning that AWAC can directly measure complex wave parameters such as **Hm0**, **H1/10**, **Tm0**, etc.

Wave direction is calculated by combining AST with orbital velocity measurements in an array near the surface. The four point array data can be processed with the maximum likelihood method (MLM) to generate accurate directional wave spectra. The MLM uses an interactive technique to sweep through frequency and direction to find the probable solution for the direction and frequency spectrum.

The piezoresistive sensor used in the AWAC has an intrinsic accuracy of +/- 0.5% of full scale. The compass consists of a flux gate with liquid tilt, allows a maximum tilt of 30° and has accuracy of 2°/0.1°. The tilt or liquid level has accuracy of -0.2°/0.1° which detects automatically the up or down positions.

The AWAC software is used to configure the instrument for deployment, retrieve the data, and convert all raw data files to ASCII. The wave parameters are calculated using the non-graphical QuickWave software.

The AWAC is mounted in a specific platform which employs four acoustic transducers asymmetrically arranged on one hemisphere to ensure that the beams point away from the mounting structure (Figure 3- 4).

ADCP set up and mooring

The AWAC were configured as follows: Profile interval = 1800 s, Number of samples – 1024, Interval = 5400 s (90 min), Depth = 40 m, SUV enabled, Av interval = 60 s, Blank = 0.5 m, Compass update rate = 10 s. The data were collected at 16 cycles a day.

To measure the wave characteristics across the Agulhas Bank, four wave moorings were deployed along the S coast of South Africa (more details are found in Appendix A, Table 3- 2). The mooring design (Figure 3- 4b) comprised a *Nortek AWAC 600 kHz* instrument deployed encased within a Flotation Technology spherical buoy at the end of a 40 m strop (anchor to buoy) in ~ 80 m of water. To ensure the insitu measurements were accurate, four different wave measurement instruments plus mooring design devices were evaluated in the sea at about 34° 12' 15"; 18° 17' 24" near Cape Town. The four devices moored included a *Wave Rider* buoy (WRN), an *Anti-trawl RDI Workhouse* (SKA), a *RDI* short *RDI Workhouse* (SKs), *RDI* long *RDI Workhouse* (SKL) and a *Nortek AWAC* (SKN). The *Wave Rider* buoy traditionally is regarded as the standard method to measure waves and therefore was selected as the reference. After the 2 months collection measurements, the data from the three *RDIs* and *Nortek AWAC* were compared with the data collected by the *Wave Rider* buoy. The results show that the *Nortek AWAC* provided results very similar to the *Wave Rider* buoy. Therefore, the *Nortek AWAC* was used in the four selected sites on the Agulhas Bank (Figure 3- 3).

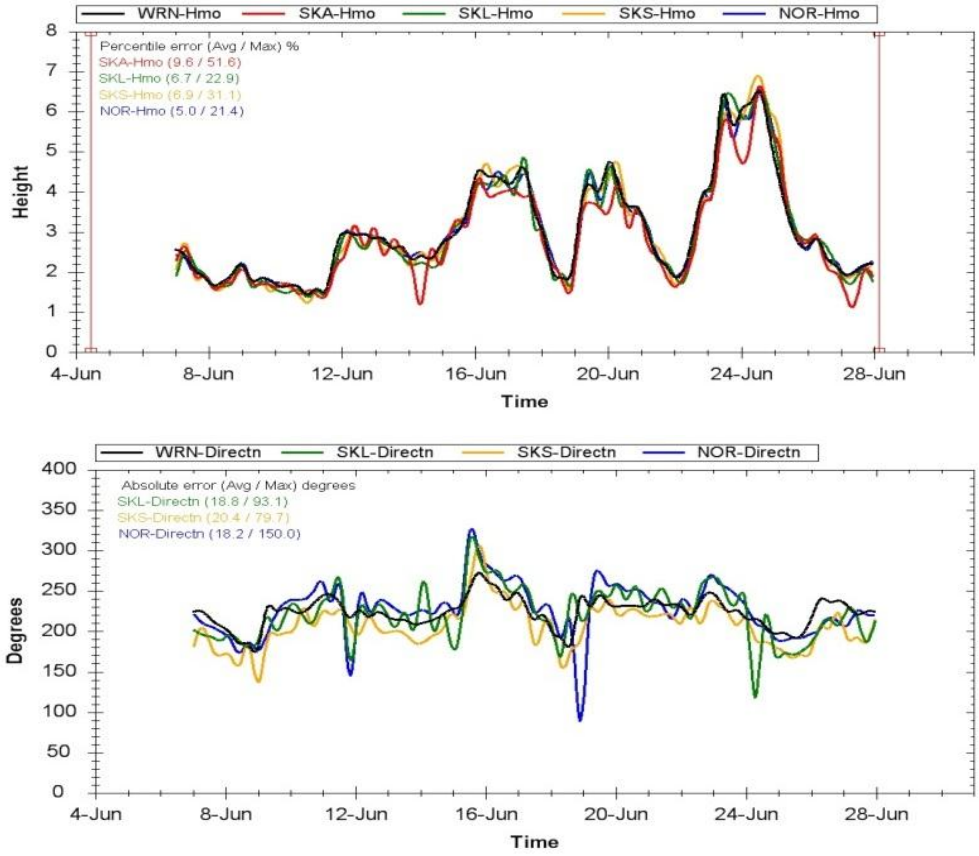

Figure 3- 3. Graphs showing the comparison of wave height plus direction measurements made by RDI and Nortek ADCP instruments moored on the seabed, on short 5 m mooring lines and 30 m mooring lines all in a depth of 80 m – and relative to a Datawell Wave Rider Buoy (Department of Environmental Affairs. South Africa 2012).

The ADCP Mooring Dilemma

As mentioned before, the AWAC uses the MLM method for directional wave processing. However, this method has limitations in the horizontal size of the data array and it prevents the resolution of waves shorter than two times the smallest horizontal separation between any two array elements. It means that the bottom mounted AWAC has maximum range of about 30 m below the sea surface, for example if it is mounted at 20 m depth, its upper wave directional frequency limit in ~ 0.32Hz (Siegel 2006). This looks to be the general limitation for all bottom mounted sensors which experience the attenuation of the wave signal with the increased depth. A primitive solution for this problem is to move the sensors closer to the water surface to keep the optimal measuring distance. It is accomplished by mounting the AWAC on a subsurface buoy, but by doing so, the directional measurements are compromised due to the rotation of the buoy which interferes with the MLM algorithm which assumes a stationary array.

Due to the rotation of the buoy, an alternative method must be used to estimate wave directional parameters. One of the alternative techniques is to interpolate the near surface horizontal velocity components (U, V) to the vertical aligned with the AST. This technique is referred as SUV (orbital velocity, U, V) which is similar to the well-known PUV (Pressure and Orbital velocities, U, V). Using the SUV technique the AWAC, equipped with high resolution compass and tilt sensor which operates at the same frequency of the beam velocities, can overcome the tilt problem as the interpolation is carried out instantaneously (Siegel 2006). The wave directional analyses can be done by using the conventional triplet techniques but instead of P (Pressure) it is used acoustic tracking system, leading to AST, U, V measurements (Siegel 2006).

The above solution allows the AWAC to be moored at any water depth. However during our measurements, it was observed that the quality of the data is affected by the swinging of the mooring. Thus, when the period of the swinging is similar to the wave period, the directional data get corrupted. This destructive interference occurs because the setup of the mooring line can cause the buoy to rotate in such frequency range equal to the frequency of the waves that the sensor is measuring. To avoid this problem, the mooring has to be mounted such that the Characteristic Response Period is lower or greater than the measured wave period (Figure 5).

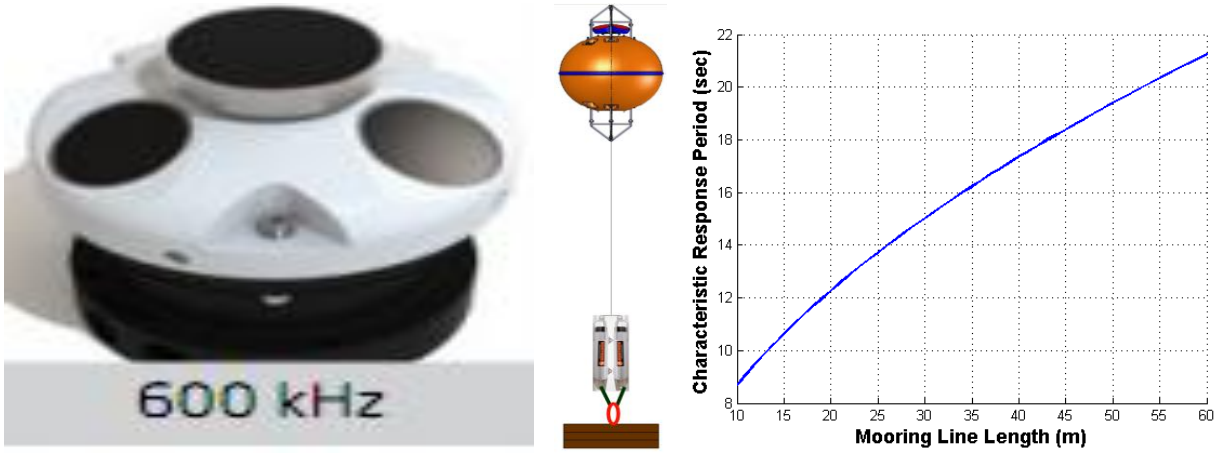

Figure 3- 4. (a) The 600 Hz ADCP Nortek AWAC; (b) The mooring design (Adapted from NORTEK 2005); (c) The characteristic response of period. (Adapted from NORTEK 2005).

***The ADCP deployments and* wave products and data processing**

The insitu data were collected over a period of 90 days (from September to December 2011). The arrays of devices were moored mid shelf on the 80 m depth contour with the *AWAC* positioned 30 m below the sea surface. The position of each mooring are: Cape Agulhas (35˚ 07.052 S, 019˚ 57.077 E), Mossel Bay (34˚ 18.719 S, 022˚ 25.986 E), Tsitsikamma (34˚ 03.653 S, 023˚ 52.132 E), and at Cape Recife (34˚ 05.316 S, 025˚ 32.321 E) (for more details, see Appendix A).Detailed information regarding the ADCP mooring configuration and the respective description of output files and selection of wave parameters can be found in Appendix A, Table 3- 4 and 3- 5.

3.2.2 NCEP – WAVEWATCH - III dataset

Model data from NCEP WAVEWATCH III version 3.14 were also used to estimate the wave power density distribution across the Agulhas Bank. These data are hindcast reanalysis done by the IFREMER (French Research Institute for Exploration of the Sea) – IOWAGA (International Ocean Waves for Geophysical and other Applications) with the software version 4.05-IFREMER_rev513 at a 0.5°x0.5° resolution. This is an 8 hour dataset which spans 16 years from 1994 to 2010. And for this particular study, the spatial coverage was from 32° S to 38° S and from 18° E to 27° E. However, for certain analyses this area was widened from 32° S to 40° S and from 15° E to 35° E. The model output is routinely validated using altimeter, SAR, buoy and dedicated field campaign data. Moreover, according to IFREMER, for validation and analysis purposes, various parameters are computed from modelled spectra. More information can be found at https://forge.ifremer.fr/plugins/mediawiki/wiki/ww3/index.php/Accueil. The data were retrieved directly from the following addresses: ftp://polar.ncep.noaa.gov/pub/waves/ and ftp://ftp.ifremer.fr/ifremer/cersat/products/gridded/ WAVEWATCH3/HINDCAST/.

The WAVEWATCH III model is run at 8 cycles a day, each cycle is 9 hours hindcast and 180 hours forecast. This model does not assimilate wave data and is based on shallow water physics without mean currents (Tolman 2009).

The governing equations used by the WAVEWATCH III model are shallow water equations described in the previous section. The general source terms used by this model are described by Equations 2- 32 and 2- 33. Other source terms are easily added and are defined for energy spectra. More information about the WAVEWATCH – III model can be found on the model user manual (http://polar.ncep.noaa.gov/mmab/papers/tn222/MMAB_222.pdf).

The model inputs are winds from the operational Global Data Assimilation Scheme (GDAS) and the Global Forecast System (GFS). The winds are converted to 10 m height assuming neutral stability. SST data from GDAS is also an input of this model and is used for stability correction for wave growth. The boundary data are also included as input. This model uses a combination of bathymetry and obstruction grids, which contain an array of water depth values or land flags at the same resolution as the wave model.

The Model provides graphical and binary data of wave parameters which includes wave significant height, wave mean and peak period, wave mean and peak direction, wave energy and directional spectra, and it also provides wind data.

3.2.3 AVISO dataset

Significant wave height and wind data from AVISO were also used to estimate the wave power density distribution across the Agulhas Bank. The wave and wind data are derived from altimetry. The altimeter products are produced and distributed by AVISO (http://www.aviso.oceanobs.com/), as part of the Ssalto ground processing segment. These are merged and gridded data with a spatial resolution of 1° x 1° resolution. More information can be found at: http://www.aviso.oceanobs.com/en/data/products/wind-waves-products/mswhmwind/processing-gridded-wind-wave-products.html.

As input, the AVISO data is from the previous two days of each satellite observations. Then the data is processed and cross-calibrated using OSTM/Jason – 2 as the reference mission. First, sigma0 and wave histograms are calibrated, and then the OSTM/Jason-2 wind algorithm is applied to cross-calibrated sigma0 (AVISO 2012).

The output parameters of AVISO of interest to this study are the **Hm0** and modulus of the sea surface wind speed and covers and area from 32° S to 40° S and from 15° E to 35° E.

3.2.4 Climate data

To assess the causes of the temporal variability of wave power density across the Agulhas Bank, this study investigated the correlation between several climate variables, global climate parameters and wave power density of the Agulhas Bank. These included regional sea level pressure, surface wind, sea surface current, sea surface temperature, and parameters such as **ENSO**, **SOI**, and **SAM**. The climate indices were all retrieved from NCEP and NOAA (National Oceanic and Atmospheric Administration) PSD Climate and Weather Data. All these variables are monthly mean for the period between 1994 and 2010. The **SLP** and surface wind were 2.5° x 2.5° gridded data (from 0° S to 60° S and from 85° W to 35° E). The sea surface current is 1° x 0.3° gridded data (from 0° S to 60° S and from 85° W to 35° E). The **SST** is 1° x 1° gridded data (global). **ENSO**, **SAM** and **SOI** were mean monthly time series. This study also used scatterometer data from IFREMER – CERSAT, a QuikSCAT monthly mean wind field data with a 0.5°x0.5° resolution from July 1999 to October 2009. For calculations purposes poor quality data were not used, indicated by the quality flags shown in the Figure 3- 6a. These indicates that 50 – 60% of the data in the region 60° S – 50° W and 35° E were of low quality (50 – 60% of the data were exclude from the calculations).

3.2.5 Data validation

In order to validate these data, this study compared the daily mean significant wave height from the ADCPs with AVISO, NCEP (WAVEWATCH III) and NCEP – IFREMER (WAVEWATCH III) Reanalysis (Figure 4- 5). It is seen that measured data from Cape Agulhas differ from that measured data from Mossel Bay, Tsitsikamma and Cape Recife. The results also show that the measured **Hm0** in Cape Agulhas compares well with AVISO but it has small differences with the NCEP dataset principally in the peaks. For a better comparison, the daily mean ADCP data of **Hm0** from the four selected mooring sites were grouped, and then the daily mean was calculated to obtain a single time series that can be compared with the NCEP and AVISO dataset (blue line in Figure 3-5). It was found that ADCP dataset is more similar to the AVISO and NCEP – IFREMER and less similar to the NCEP. Correlation and regression analyses were done between the data sets. These analyses were done only for the period which corresponds to the ADCP time series. Thus, correlation and regression coefficients between the ADCP and AVISO dataset were **r** = 0.83 and $\mathbf{R^2}$ = 0.49, between the ADCP and NCEP- IFREMER Reanalysis were **r** =0.7 and $\mathbf{R^2}$ **=** 0.68, and between ADCP and NCEP were **r** < 0.4 and $\mathbf{R^2}$ < 016. The reason why the NCEP differ from the other three datasets is probably the absence of reanalysis and calibration using insitu wave data from wave buoys. The small differences between the ADCP, NCEP – IFREMER and AVISO datasets may be related to the spatial and temporal resolution and the algorithm which the AVISO dataset uses. Based on this comparison, and due to the fact that the NCEP - IFREMER (WAVEWATCH III) and ADCP data sets were much similar comparing to the other data sets, this study chose to use the long time series NCEP - IFREMER and the short time series insitu ADCP data sets.

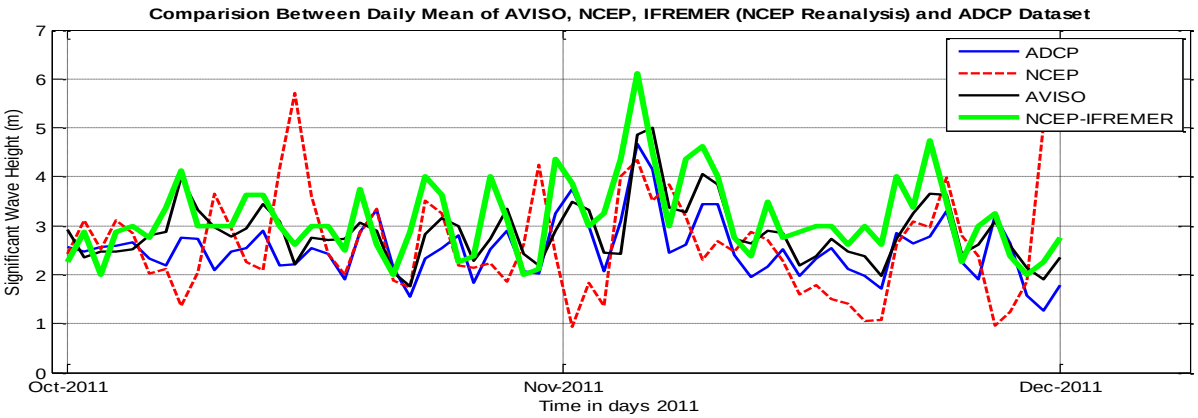

Figure 3- 5. Data validation by comparing different datasets with the insitu data. The time series corresponds to the daily mean of Hm0 for the parallel 34° S on the Agulhas Bank for the period modelled between 1st October and 1st December 2011. The blue line represents the mean of the four selected (ADCP) mooring sites.

3.3 Data analysis

The data used in this study were analysed assuming that the wave height and wave period follow the Rayleigh distribution (a continuous distribution which relates the magnitude of wave height and period to wave direction components). It is also assumes the linear wave theory and narrow band spectrum (Early and Bishop 1984).

All data were analysed using MATLAB 2011b. MATLAB is a numerical computing environment and fourth generation programming language (http://www.mathworks.com/products/matlab/). Auxiliary tools such as KNMI Climate Explorer (a web research tool designed to investigate climate statistically (http://www.climexp.knmi.n)), and Microsoft Excel (http://www.office.microsoft.com/en-us/excel).

The NCEP dataset was used to analyse the temporal and spatial distribution and variability of the wave parameters and wave power density across the Agulhas Bank. Because this is a gridded datasets and to improve the comparison between the NCEP data and the ADCP data, the calculations and estimation were conducted along 35.3° S (~128.5 m water depth) rather than at 80 m water depth as was done for the ADCP dataset.

The ADCP data was used to analyse the wave field characteristics and variability at the 4 selected sites on the Agulhas Bank. The AVISO data-set was used to analyse the wind and significant wave height on the Agulhas Bank by comparing it with NCEP and ADCP Data.

Methodology for assessing the wave field characteristics

This section describes the methodology employed to assess the wave field on the Agulhas Bank using both ADCP and NCEP datasets.

First, wave data were retrieved from both datasets then filtered by removing the abnormal values. Then the wave parameters were plotted without any analysis in order to visualise the real tendencies.

In total there were 1274 data points for each parameter measured by the ADCP and 46505 data points of wave parameters provided by NCEP. As indicated above, the ADCP data correspond to the 80 m bathymetric contour and the NCEP data to128 m.

To calculate the daily mean of the wave parameters measured by the ADCP using Equation 3- 1. Both the energy and directional wave spectra were obtained by calculating the global mean of the total of each individual spectrum.

To obtain the frequency of occurrence of waves with a certain significant wave height, period, direction and power density for both datasets, each of these quantities were plotted using cumulative histograms described by Equation 3- 2.

Another statistical analysis involved the cumulative distribution function (CFD) (Equation 3- 2) of the wave parameters including the quantity wave power density. The CFD describes the probability that a real random value of a given variable with a given probability distribution will be found at a value less than or equal to *x*. In order to compare the same wave characteristics for different wave fields, the 25% and 75% percentile method was used and can be described by Equation 3- 3.

$$\mu_N = \frac{X_j}{N} \qquad \text{Equation 3- 1}$$

Where μ is the mean, N represents the total number of samples and j is the index of the individual sample.

$$M_i = \sum_{j=1}^{i} m_j \qquad \text{Equation 3- 2}$$

Where M is the cumulative count of total number of observations which fall into the disjoint categories (bins) m_j in all bins of index i up to the specified bin.

$$F(x) = \int_{-\infty}^{x} f(x)dx \qquad \text{Equation 3- 3}$$

Where $\boldsymbol{f(x) = P[a \leq X \leq b]/dx}$, in which P is the probability of a random variable $\boldsymbol{X}$ (in this case $\boldsymbol{X}$ represents a wave parameter) fall within a particular region of the interval with limits $\boldsymbol{a\ b}$ given by the density of the variable integral.

$$n = \frac{P}{100} \cdot N + 0.5 \qquad \text{Equation 3- 4}$$

Where n is the nearest rank, P is the percentile which in this case is 25 and 75 and N is the order value from least to last.

The third task was to calculate the diurnal cycle, monthly and seasonal mean. These means where obtained as follows: The daily mean was obtained by averaging the total data points of each day for the whole period using same equation as Equation 3- 1 where ***N*** represents the total number of data points (samples), ***X*** is the variable and *j* is its index. The monthly mean was calculated by averaging all the data points contained in each month for the whole period. This also uses the same equation as the daily mean however the days are replaced by months. To obtain the seasonal mean, the year was divided into four seasons namely: January, February and March which corresponds to summer; April, May and June, corresponding to autumn; July, August and September, which corresponds to winter season. And October, November and December which correspond to spring. Then, the average for each season was calculated within the entire period of 16 years (2008 has missing data). Equation 3- 1 was also used for this propose in which ***N*** represents the total number of data points contained in each season, ***X*** is the variable and *j* is the index.

Methodology for estimation of the temporal variability of the wave parameters and wave power density

ADCP dataset was used to estimate the average diurnal cycle of the wave parameters and wave power density at the 4 selected sites. The high sampling frequency (16 samples of 30 min each per 24 hours day) enable an easy interpolation of data. To extract the average diurnal cycle, the day was divided by 4 parts which correspond to the morning (6h to 11h 59min), afternoon (12h to 17h 59min), evening (18h to 23h 59min) and night (24h to 5h 59min) respectively, and the mean for each period was calculated for all days of sampling . Equation 3- 1 was again used in this section however, for this purpose *N* represents the total number of data points contained in each period, *X* is the variable and *j* is the index.

The long term trend of the wave parameters and wave power density were done by analysing the monthly mean, seasonal mean and annual mean. Then, from these calculations, the temporal and spatial variability were estimated. Equation 3- 5 was used to estimate the temporal variability:

$$COV(\boldsymbol{X}) = \frac{\sigma(\boldsymbol{X}(t))}{\mu(\boldsymbol{X}(t))} = \frac{\overline{\sqrt{(\boldsymbol{X} - \overline{\boldsymbol{X}})^2}}}{\overline{\boldsymbol{X}}} \qquad \text{Equation 3- 5}$$

Where the vector $\boldsymbol{X} = X_1, X_2, X_3 \ldots . X_n$ represents the variable in study, t is the total time, σ is the variance of the variable, and μ is the mean of the variable. The correlation between wave power density and climate indices were analysed taking into account the temporal and spatial dimensions. For sea level pressure, wind and sea surface currents, the domain was the region between 80° W to 30° E and from 0° S to 60° S was used. For SST the domain was global so as to cover the **NINO** regions. Given the dimensions of the data the P-value selected was 0.4. Equation 3- 6 describes the correlation between the two variables. Moreover, this study also estimated the relationship between two variables by using multiple regression model ($\hat{Y}i$ and R^2), assuming that $\hat{Y}i = \alpha + \beta_1 X_{1i} + \beta_2 X_{2i}$. And

$R^2 = \sum(\hat{Y}i - \bar{Y})^2 \Big/ \sum(Yi - \bar{Y})^2$ Where α and β are the population parameters (β is the regression coefficient and α is the Y intercept), X is the independent variable, Y is the corresponding dependent variable and $\bar{Y}$ is its average. R^2 describes variability in Y accounted by the regression model and indicates the strength of linear relationship between multiple variables.

$$CORR(\boldsymbol{X}, \boldsymbol{Y}) = \frac{COV((\boldsymbol{X}, \boldsymbol{Y})}{\sigma_{\boldsymbol{X}}\sigma_{\boldsymbol{Y}}} \qquad \text{Equation 3- 6}$$

Where the vectors $\boldsymbol{X}$, $\boldsymbol{Y}$ represents the two variables in study.

Methodology for estimating the total naturally available wave power density resource

The wave power density (which is the wave energy flux per meter of wave crest) was estimated using Equation 2- 23. This equation describes the wave power density in watts per meter aggregated across a unit diameter circle, this includes the resource made available by the lateral transfer of wave energy along wave crests which enables wave diffraction to substantially re-establish wave power densities within a few km of a linear array or single wave converting device. The total recoverable wave power density can be obtained by multiplying Equation 3- 7 by the total length of the desired region and by the desired time (Boyle 2004, Sorensen 2004, and Jacobson 2011).

$$P_{Total} = 490\, T_e (H_{m0})^2 \cdot L \cdot t \qquad \text{Equation 3- 7}$$

Where the total is time (e.g. 8.760 hours for annual totals) and is the length of the bathymetric in analysis.

To better assess the available wave power density across the Agulhas Bank, this region was divided into three: the southwest region (18° E to 21° E) which contain the Cape Agulhas, the S region (21° E to 24° E) which contain the Tsitsikamma and the southeast region (25° E to 27° E) which contains the Cape Recife. Each region contains 248 data points for the bathymetric contour of 128 m (35.5° S) (Figure 3- 6b).

Methodology for estimating the total technically recoverable wave power density resource

Technically, wave power density can be estimated by first defining the operating range of the wave power density devices. As referenced before, a converting device has the threshold operating condition (TOC), the rated operating condition (ROC) and the maximum operating condition (MOC) (Jacobson 2011). There is a sea state threshold below which the wave spectrum is not adequate to sustain continuous operation of any wave power converting system due to technical and mechanical limitations such as friction between the sea water and the device parts and at-rest inertia. Thus, this study investigated the minimum, the average and the maximum available wave power density which can be continuously recoverable by a device or array of devices. This was done by analysing the

cumulative histograms which show the frequency of occurrence of the significant wave height and period of the wave field.

Methodology for Estimating the Power Necessary for the Pump Storage Scheme

To assess the power that is necessary to pump sea water into the upper reservoir of the PSS the following steps were taken: first is calculated the power ($\mathbf{P_{PSS}}$) for a given head (**H**), flow rate (**Q**) and efficiency (**η**), using Equation 3- 8 (is the density of the sea water, is the acceleration due gravity) (Boyle 2004). And knowing that the flow rate can vary from very weak (0.05 m^3s^{-1}), medium weak (1 m^3s^{-1}), medium (50 m^3s^{-1}) and high (100 m^3s^{-1}), and also knowing that the hydro plants can be of small scale (30 MW capacity), and medium to large scale (with a capacity greater than hundreds of MW). The power generation capacity is also linked by the efficiency of the pumps or turbines, which for convenience this study selected efficiencies of 85% and 85%. The new technologies can provide machines with efficiency near 98%.

$$P_{PSS} = \rho \times Q \times g \cdot H \times \eta$$ Equation 3- 8

Where ρ is the density of the sea water, g is the acceleration due gravity.

The second step was to calculate the time (***t***) necessary to fill up the upper reservoir with a small, medium and large volume (***V***) of sea water. The study selected volumes of 5 million m^3, 10 million m^3 and 15 million m^3 w. The pumping time is a function of water flow rate and volume size of the reservoir and it can be described by Equation 3- 9.

$$t = \frac{V}{Q}$$ Equation 3- 9

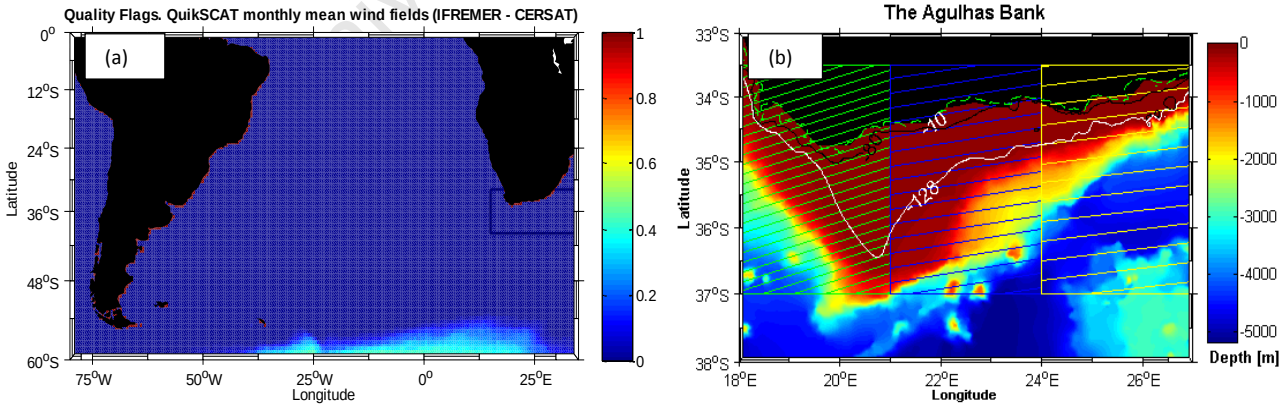

Figure 3- 6. Quality Flags for the QuikSCAT IFREMER- CERSAT wind data fields (units in percentage); (b) The Agullhas Bank and the three sub regions. Green box corresponds to the Southwest region, the blue box corresponds to the South region, and the yellow box corresponds to the Southeast region.

Chapter 4

Results

4.1 Description of wave field based on the insitu ADCP data

This chapter presents the results of the data analysis done using the previously addressed methodologies. The first section of this chapter presents the results of the wave field characteristics and wave power density on the Agulhas Bank obtained using insitu (ADCP) wave data, and the third section presents the results obtained using model (WAVEWATCH II) wave data. The diurnal cycle is analyzed in the second section, and the seasonal and interannual variability is analysed in the third section. The fourth section presents the relationship between wave power density and some climate variables. The estimated wave power density resource on the Agulhas Bank presented in the fifth sections of this chapter, and the estimated power necessary for the pumped storage scheme is presented in the sixth section. Extra Figures have been placed in Appendix A and are denoted by the prefix "A".

4.1.1 Daily mean values of the wave field parameters

The wave field of Cape Agulhas is characterized by high wave heights. The observations show a maximum value of significant wave height (**Hm0**) of 5.9 m, with a minimum of 1.4 m, with an average of 2.9 m. The daily mean (Equation 3- 1) of the **Hm0** varied from 1.6 to 4.9 m (Figure 4- 1a1).

The initial data (Figure A2) shows that at Cape Agulhas, the mean period (**Tm0**) varied from 4.5 s to 11.2 s, with a mean of 6.6 s. The peak period (**Tp**) was well above the **Tm0**, reaching a maximum of 17.2 s and a minimum of 5.3 s, with an average 10.5 s. The maximum wave heights (**Hmax**) varied from 2.1 m to 9.3 m, with an average of 4.6 m. The daily values of **Tm0** varied from 5.1 s to 9.0 s (Figure 4- 1b1). These observations also show that the predominant mean direction (**Mdir**) of wave incidence at Cape Agulhas is from southwest around 200° to 280°, although waves coming from the S, southeast and from the northwest were also observed (Figure A3). The energy spectrum in Figure 4- 2a shows that the predominant waves at Cape Agulhas are those in the spectral band from 0.05 to 0.2 Hz, with the 0.1 Hz being the peak of the wave field. The directional spectrum shows that the waves at this site propagate predominantly from the southwest (Figure 4- 2b). The average swell height was 2.6 m the minimum and maximum were 1.1 m and 5.9 m respectively. The average **Tm0** was 8.8 s, the minimum and maximum were 6.7 s and 12.8 s respectively. The seas had a daily mean of 0.8 m for **Hm0** and 3.5 s for **Tm0** (Figure A5).

The wave field at Mossel Bay is characterized by waves with **Hm0** varying from 1.2 m to 5.6 m with an

average of 2.6 m (Figure A6). The **Hmax** values varied from 1.4 m to 9.3 m with an average of 3.9 m (Figure A7). The daily values of **Hm0** had a minimum of 1.3 m and a maximum of 4.6 m (Figure 4- 1a3). The **Tm0** at Mossel Bay varied from 4.5 to 10.8 s with an average equal to 6.9 s. The observed **Tp** varied from 5.7 to 16.8 s, with an average equal to 10.7 s. The daily mean of **Tm0** varied from 5.4 to 8.9 s and the **Tp** varied from 8.2 to 14.8 s. The zero crossing period (**Tz**) values were very similar to the **Tm0** as the Figure 4- 1b2 shows. The **Mdir** at Mossel Bay is similarly from the southwest, 200° to 280° (Figure A8 and A16). The energy spectrum clearly shows a predominance of waves of frequency 0.1 Hz. The directional spectrum also confirms that the predominant waves propagate from the southwest (Figures 4- 2a and 4- 2b). The swell waves measured heights varying from 0.9 m to 5.4 m with an average of 2.4 m. The daily mean were 0.8 m for **Hm0** and 3.5 s for **Tm0**. The daily mean swell had **Hm0** which varied from 1.3 to 4.4 m and **Tm0** which varied from 6.6 to 12.1 s and **Tp** had an average of 10.7 s (Figure A9). The seas have **Hm0** varying from 0.2 to 1.4 m and **Tm0** < 4.7 s (Figure A9).

At Tsitsikamma, the values of **Hm0** were in the interval between 1.1 to 5.3 m with an average of 2.5 m. **Hmax** varied from 1.4 to 9.8 m with an average of 3.8 m (Figure A10). The daily mean **Hm0** values varied from 1.3 m to 4.7 m (Figure 4- 1a3). The **Tm0** values were in the interval between 4.4 and 10.7 s with an average of 6.8 s. The average **Tp** was 10.9 s, the minimum and maximum were 5.4 s and 15.1 s respectively (Figure A11). The daily mean values for wave period had the following range: from 4.8 to 9.4 s for **Tm0,** from 8.5 to 13.7 s for **Tp,** and from 5.2 to 9.7 s for **Tz** (Figure 4- 1b3). The energy spectrum shows that the wave field at Tsitsikamma was mostly characterized by waves with frequencies in the range of 0.05 to 0.2 Hz with a peak at 0.1 Hz. The directional spectrum clearly shows that the waves are predominantly from the southwest (200° to 250°), (Figures 4- 6a and 4- 6b). The measured swell at Tsitsikamma had **Hm0** which varied from 1.0 to 4.3 m with an average of 2.4 m, and **Tm0** varied from 6.7 to 12.3 s with an average of 9.1 s, and **Tp** varied from 7.6 to 14.1 s. The sea waves had heights between 0.3 and 1.4 m and periods between 2.9 to 3.7 s (Figure A13).

The wave field at Cape Recife was characterized by **Hm0** which varied from 1.3 to 5.3 m with an average of 2.5 m. **Hmax** varied from 1.5 to 8.3 m with an average of 3.8 m (Figure A14). The daily mean values of **Hm0** from 1.4 to 4.3 m (Figure 4- 1a4). **Tm0** had an average of 6.5 s, a minimum and maximum of 4.0 and 11.0 s respectively. **Tp** varied from 5.6 to 15.0 s, with an average of 11.0 s (Figure A15). The daily values for wave period at Cape Recife varied from 4.7 to 9.2 s for **Tm0**, from 7.4 to 14.1 s for **Tp,** and from 5.0 to 9.8 for **Tz** (Figure 4- 1b4). The data also shows that **Mdir** is from the southwest, but, at Cape Recife the waves come more from the south compared to the other three sites (Figure A16 and A21). The energy spectrum at Cape Recife shows that the wave field was mostly composed by 0.1 Hz waves, and the directional spectrum also shows that the waves at this location were indeed predominantly from the southwest (200° to 250°). The measured swell at Cape Recife has **Hm0** varying from 1.1 to 5.2 m with an average of 2.4 m, the **Tm0** varied from 6.8 to 12.5 s with an average of 9.1 s, and **Tp** varied from 5.6 to 15.0 s with an average of 11.0 s (Figure A17). The sea waves

had values of **Hm0** varying from 0.3 to 1.4 m in wave height and a **Tm0** < 3.8 s.

4.1.2 Daily mean values of wave power density

The wave power density (**P**) which is a function of **Hm0** and **Tm0** (Equation 2- 40), was analyzed at each observed site across the Agulhas Bank. From west to east, the values of **P** were estimated using the measured wave parameter at Cape Agulhas, Mossel Bay, Tsitsikamma and Cape Recife, with the following results.

According to the data, the wave field at Cape Agulhas was characterized by having values of **P** which varied from 4.3 kW/m to 194.9 kW/m with an average of 31.2 kW/m (Figure A22). The daily mean values of **P** varied from 7.4 kW/m to 85.5 kW/m, with an average of 30.3 kW/m (Figure 4- 3).

At Mossel Bay, the wave field was characterized by values of **P** that varied from a minimum of 3.3 kW/m to a maximum of 125.5 kW/m with an average of 25.2 kW/m (Figure A23). The daily mean values of **P** had a minimum of 5.4 kW/m, a maximum of 79.3 kW/m and an average of 24.4 kW/m (Figure 4- 9).

At Tsitsikamma, **P** had values that varied from 3.3 kW/m to 140.0 kW/m with an average of 25.0 kW/m (Figure A24). The daily mean varied from 4.7 kW/m to 80.5 kW/m with an average of 24.5 kW/m (Figure 4- 9).

The wave field at Cape Recife had **P** that varied from 3.7 kW/m to 120.0 kW/m, with an average of 23.7 kW/m (Figure A25). The daily mean values of **P** at this site varied from 5.2 kW/m to 70.9 kW/m with an average of 22.9 kW/m (Figure 4- 9).

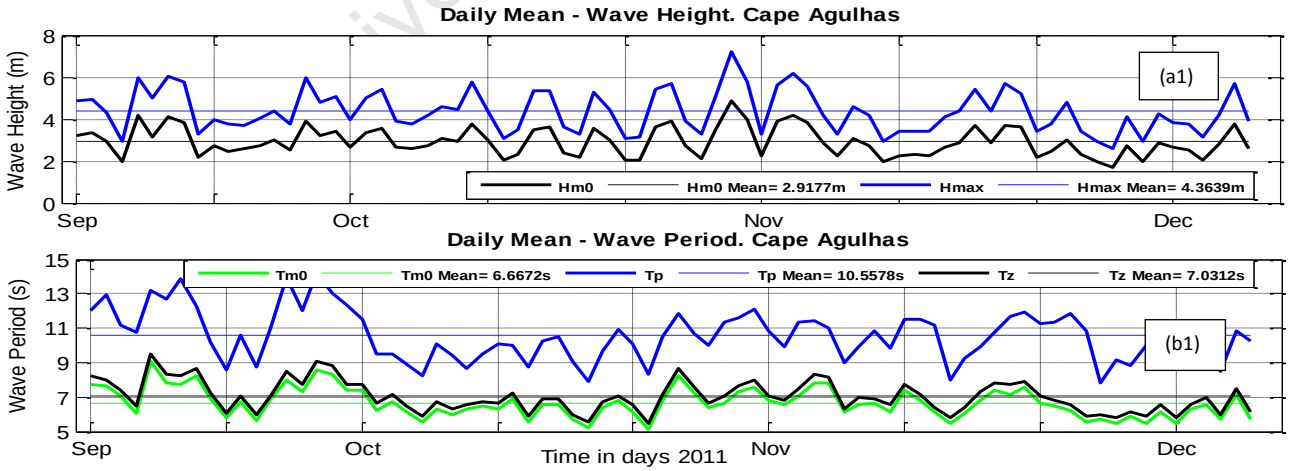

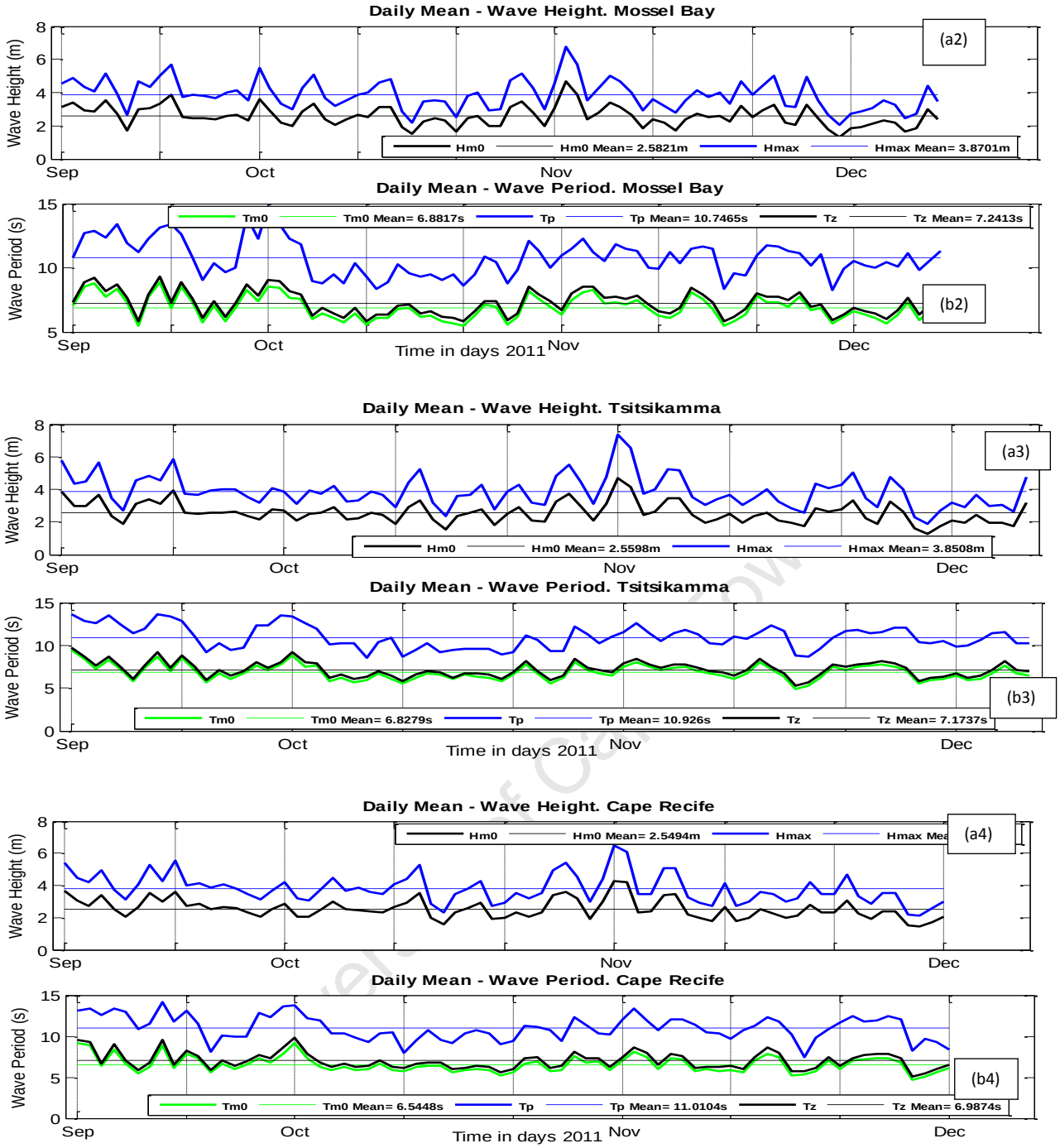

Figure 4- 1. (a) Daily mean values of significant wave height and maximum wave height; (b) Daily mean values of mean period, peak period and zero crossing periods for the four selected sites across the Agulhas Back.

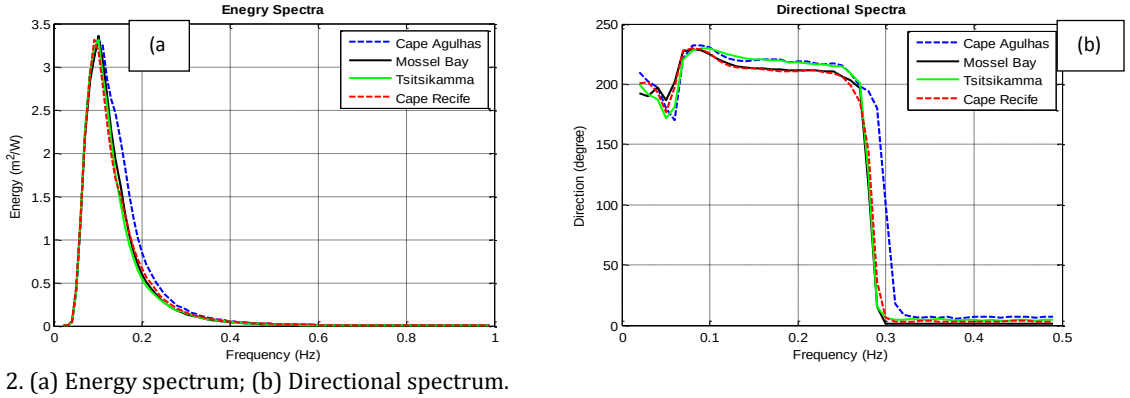

Figure 4- 2. (a) Energy spectrum; (b) Directional spectrum.

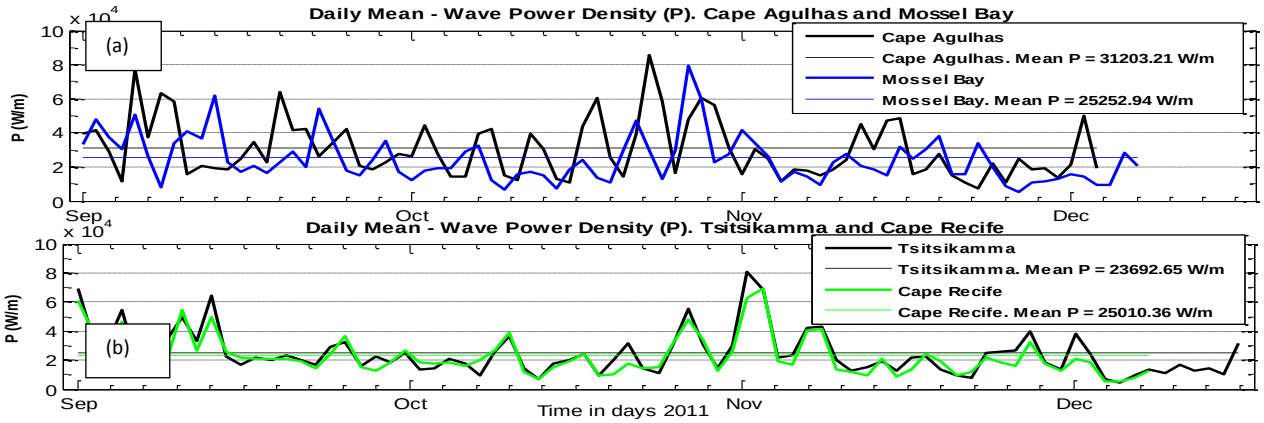

Figure 4- 3. Daily means of wave power density (P): (a) Cape Agulhas and Mossel Bay; (b) Tsitsikamma and Cape Recife.

4.1.3 Cumulative distribution of the wave field parameter and wave power density

In order to better understand the characteristics of the wave field and the distribution of the wave power density across the Agulhas Bank, a cumulative distribution (Equation 3- 2) was calculated for **Hm0**, **Tm0** and for the wave power density (**P**) by counting and summing the number of times in which a certain wave characteristic occurred within the observation period.

At Cape Agulhas, the observations show that most of the waves had **Hm0** in the interval between 1.7 to 4.5 m, although waves with 2.0, 2.3, 2.5, 2.7 and 3.0 m also occurred with higher frequency (Figures 4- 4a). This spectrum also shows that most the frequent waves were below 3.5 m. Waves with maximum height (**Hmax**) occurred more in the range between 2.8 and 6.0 m with a higher frequencies between 3.0 and 4.8 m (Figure A26). Waves with **Tm0** in the range between 5.0 and 8.0 s were more likely to occur, however the high frequency of occurrence was for waves with 6.0 to 7.5 s (Figure 4- 4b). On other hand, the spectrum of **Tp** show that the higher frequency of occurrence was for the waves with 11 and 12.0 s (Figure A27). At Cape Agulhas, most values of **P** were concentrated in the interval between 10 and 50 KW/m with the highest frequency between 15 and 30 kW/m (Figure 4- 4c) However if we estimate **P** using **Hmax** and **Tp**, then it is seen that values of **P** were more concentrated in the interval between 25 and 150 kW/m with highest frequency of occurrence between 30 and 70 kW/m (Figure A28).

At Mossel Bay, the frequency of occurrence of waves with 1.8 to 3.5 m was higher with the highest frequency corresponding to waves with 2.5 m (Figure 4- 4a). Waves with **Hmax** had the higher frequency of occurrence in the range between 3.0 and 5.0 m, with the highest frequency corresponding to waves with 3.5 m (Figure A26). The spectrum for the mean period at Mossel Bay is wide and the higher frequency of occurrence corresponds to waves with **Tm0** in the interval between 5.3 to 8.5 s (Figure 4- 4b). Waves with **Tp** between 10.0 and 12.0 s had a higher frequency of occurrence (Figure A27). These results also show that **P** at Mossel Bay wave field was more concentrated in the interval between 5.0 to 40 kW/m, with the highest concentration of **P** in the interval between 15.0 and 24.0

kW/m (Figure 4- 4c). The spectrum of maximum values of P shows that high frequency of occurrence corresponds with waves with values of **P** between 30.0 to 90.0 kW/m (Figure A28).

The Tsitsikamma wave field had the most frequent waves occurring with **Hm0** in the interval from 1.8 to 3.0 m with the highest frequency for waves with 1.8, 2.3, and 2.5 m (Figures 4- 4d). It was also observed that those waves with **Hmax** in the interval between 2.8 and 4.5 m had more probability of occurring (Figure A26). At Tsitsikamma, waves with **Tm0** in the interval between 5.5 to 8.5 s have a higher frequency of occurrence with 7.3 s waves having the highest frequency of occurrence (Figure 4- 4b). The spectrum of wave **Tp** at this location shows clearly that waves with **Tp** near 11 s were more frequent (Figure A27). The wave field was characterized by values of **P** in the interval between 0.5 and 50 kW/m, with the highest frequency of occurrence in waves with 10, 20 and 25 kW/m (Figure 4- 4c). By estimating **P** using the **Hmax** and **Tp**, the results show that values **P** were concentrated in the interval between 25 and 125 kW/m (Figure A28).

Cape Recife was characterized by a higher frequency of occurrence with **Hm0** in the interval between 1.5 to 3.5 m, and highest frequencies for waves with heights of 2.1, 2.3, 2.7 and 3.1 m (Figure 4- 4a). The most frequent **Hmax** were between 2.8 to 4.8 m (Figure A26). Waves with the **Tm0** in the interval between 5.2 to 8.3 s had higher frequency of occurrence with waves with **Tm0** near 5.5, 6.0, 6.5 and 7.0 s being the most frequent (Figure 4- 4b). The **Tp** spectrum shows that waves with period from 10 to 12 s had higher frequency of occurrence (Figure A27). The results also show that the average **P** at Cape Recife was more concentrated in the interval between 5.0 to 35.0 kW/m with the peak of occurrence for waves with 13 to 20 kW/m (Figure 4- 4c). However, if we consider the maximum **P** spectrum, then the results would be that values of **P** were more concentrated in the interval between 30 to 80.0 kW/m of wave crest (Figure A28).

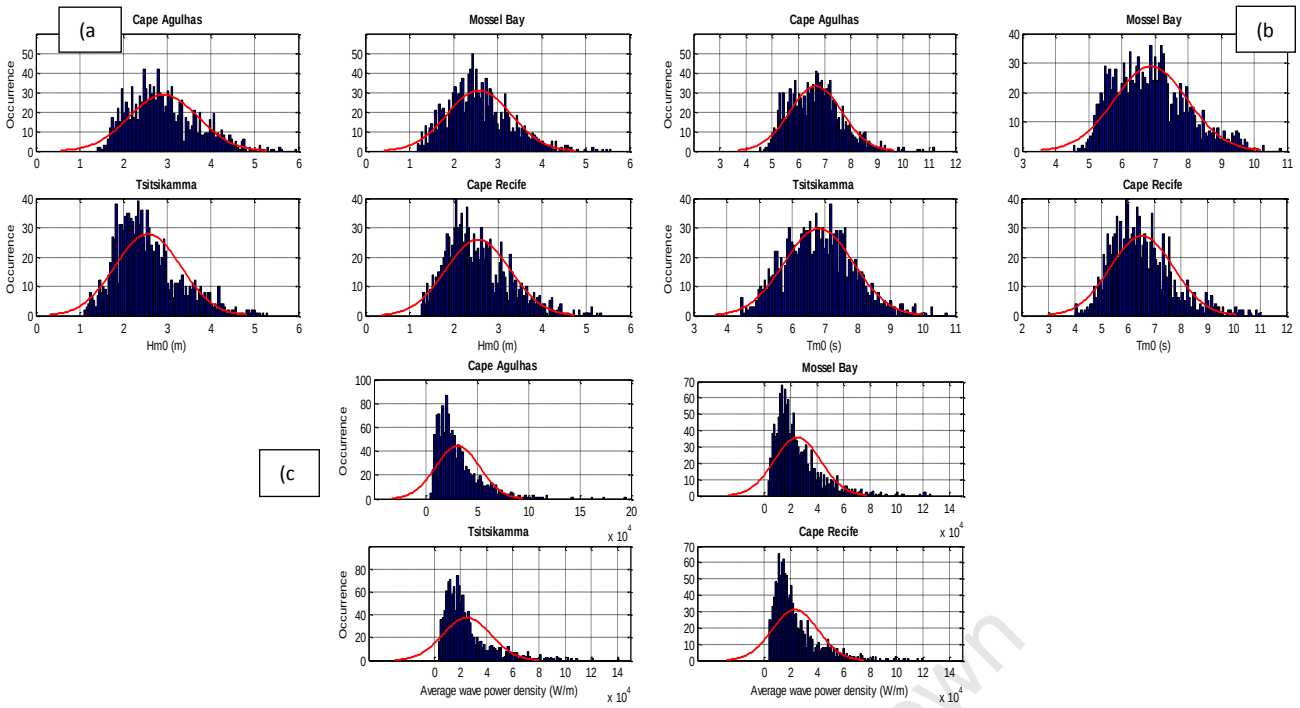

Figure 4- 4. Frequency of occurrence of: (a) significant wave height (Hm0); (b) mean period (Tm0); and (c) wave power density (P).

4.1.4 Wave field comparison between sites

Comparing the four selected mooring sites across the Agulhas Bank, it is clear that Cape Agulhas has the highest **Hm0**, followed by Mossel Bay, Tsitsikamma and least Cape Recife. The recoverable resource is estimated as the percentage of the available resource that can be absorbed within the optimal device operating range of most of wave converting devices. Table 4-1 and Figure 4- 5a show the distribution of waves per **Hm0** range. In terms of the cumulative probability distribution, it seen that Cape Agulhas has 99% of the waves with **Hm0** below 5.0 m while, Tsitsikamma, Mossel Bay and Cape Recife have 99% of the waves with **Hm0** below 4.1 m. in contrast, Cape Agulhas has only 34% of the waves with **Hm0** below 2.0 m, Tsitsikamma, Mossel Bay and Cape Recife has between 51% and 54% of the waves with **Hm0** below 2.0 m (Figure 4- 5b). In terms of the total average **Tm0**, Mossel Bay has the highest values, second is Tsitsikamma, third is Cape Agulhas and fourth is Cape Recife. Table 4-2 and Figure 4- 5c show the distribution of waves per mean period. It is also observed that waves with **Tm0** between 9 to 11 s occurred more at Tsitsikamma and Cape Recife. In terms of cumulative probability distribution, Cape Recife has 96% of the waves with **Tm0** below 9 s, Mossel Bay and Tsitsikamma has 97% and Cape Agulhas has 98%. Below 6 s, Tsitsikamma has only 40%, Mossel Bay has 41%, Cape Agulhas has 45% and Cape Recife has 55% (Figure 4- 5d).

Table 4- 3 and Figure A30 show the results of the comparison between **P** estimations for Cape Agulhas, Mossel Bay, Tsitsikamma and Cape Recife. In terms of the cumulative probability distribution, Cape Agulhas has 97.5% of **P** below 100 kW/m, Mossel Bay, Tsitsikamma and Cape Recife have 99% of the **P** below 100 kW/m. Below 60 kW/m. on the other hand Cape Agulhas has only 35% of values of **P** below

20 kW/m while Mossel Bay and Tsitsikamma has 50 % and Cape Recife has 55% of the waves with **P** below 20 kW/m (Figure 4- 5e).

For values of **P** estimated using **Hmax** and **Tp** which we can call as maximum wave power density, the results are that Cape Agulhas has 95% of the **P** below 300 kW/m, Tsitsikamma, Mossel Bay and Cape Recife has ~ 98%. Below 120 kW/m, Cape Agulhas has 66%, Tsitsikamma, Mossel Bay and Cape Recife has ~ 79% below 120 kW/m. Below 60 Tsitsikamma, Mossel Bay and Cape Recife has ~ 98%. Below 120 kW/m, Cape Agulhas has only 25%, Tsitsikamma, Mossel Bay and Cape Recife have ~ 40% of values of **P** below 60 kW/m (Figure 4- 5f).

Using the 25% and 75 % percentile method (Equation 3- 3) for this analyse and comparing the **P** between the 4 selected sites, the results confirm that Cape Agulhas has more available **P** 75% for 40 kW/m and 25% for 17 kW/m with the median corresponding to 26 kW/m; second is Mossel Bay with 75% for 34 kW/m and 25% for 14 kW/m with a median corresponding to 21 kW/m; third is Tsitsikamma with 75% for 32 kW/m, 25% for 13 kW/m and the median corresponds to 20 kW/m; least Cape Recife with 75% for 30 kW/m, 25% for 12 kW/m and the median corresponds to 18 kW/m (Figure 4- 5g).

Table 4- 1. Cumulative distribution of wave according to its significant wave height

	Hm0 [2.1 to 3.1 m]	Hm0 [3.1 to 4.1 m]	Hm0 [4.1 to 5.1 m]	TOTAL Hm0 >1.0 m
Cape Agulhas	37%	42%	18%	96%
Mossel Bay	50%	34%	9%	93%
Tsitsikamma	54%	29%	10%	93%
Cape Recife	52%	32%	8%	92%

Table 4- 2. Cumulative distribution of waves according to its mean period

	Tm0 [5.0 to 6.0 s]	Tm0 [6.0 to 7.0 s]	Tm0 [7.0 to 8.0 s]	Tm0 [8.0 to 9.0 s]	TOTAL Tm0 >4.0 s
Cape Agulhas	13%	29%	37%	15%	94%
Mossel Bay	11%	32%	34%	16%	93%
Tsitsikamma	11%	32.5%	32%	19%	94.5%
Cape Recife	18%	36%	32%	11%	97%

Table 4- 3. Comparison between the wave power density (P) of the four selected wave fields using initial and daily averaged values

	P [minimum]		P [mean]		P [maximum]	
	Initial	Daily average	Initial	Daily average	Initial	Daily average
Cape Agulhas	4.3 kW/m	7.4 kW/m	31.2 kW/m	30.3 kW/m	195 kW/m	85.5 kW/m
Mossel Bay	3.2 kW/m	5.4 kW/m	25.2	24.4 kW/m	125.5 kW/m	79.3

			kW/m			kW/m
Tsitsikamma	3.3 kW/m	4.6 kW/m	25.0 kW/m	24.5 kW/m	141.4 kW/m	80.5 kW/m
Cape Recife	3.8 kW/m	5.1 kW/m	23.7 kW/m	22.8 kW/m	120.2 kW/m	68.9 kW/m

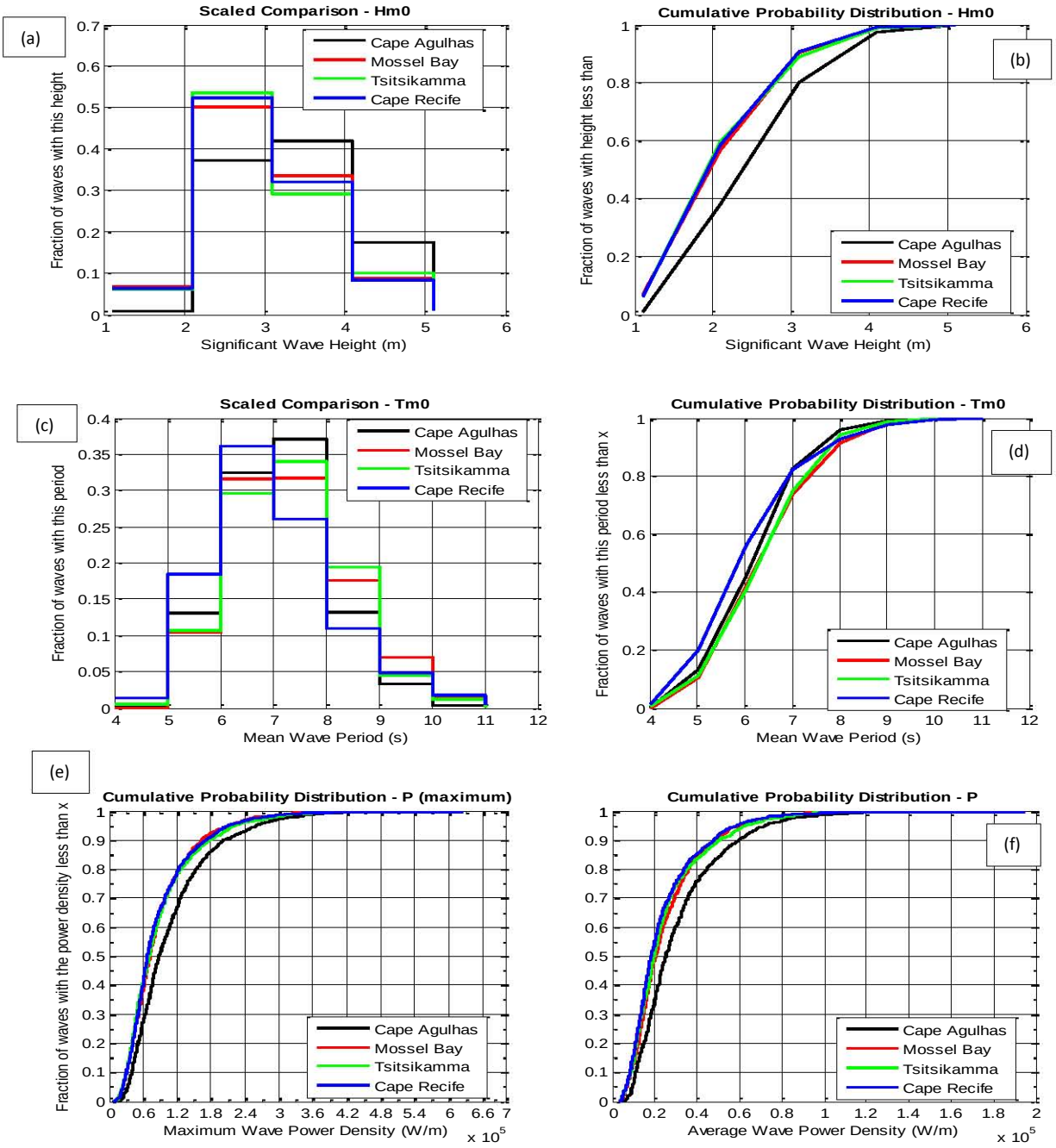

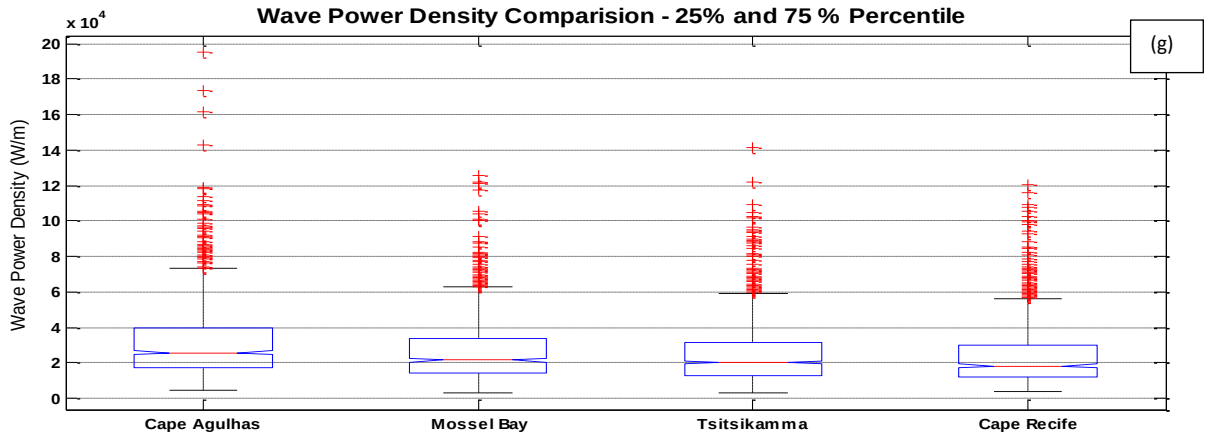

Figure 4- 5. (a) Scaled cumulative distribution comparison for Hm0; (b) cumulative probability distribution for Hm0; (c) Scaled cumulative distribution comparison for Tm0; (d) Cumulative probability distribution for Tm0; (e) Scaled cumulative distribution comparison for average wave power density; (f) Scaled cumulative distribution comparison for maximum wave power density; (g) 25% and 75% percentile comparison for values of P between the four selected sites.

4.2 Diurnal cycle

The high temporal resolution of the ADCP dataset and the long time series of the NCEP data, enabled this study to investigate whether or not, a diurnal cycle exists in the wave field across the Agulhas Bank. Table 4- 4 and Figure 4- 6 describe the diurnal cycle extracted from the 16 hourly ADCP data collected at the four selected sites. The 8 hourly long time series NCEP data (Figure 4- 7), shows that in deed there is a diurnal cycle on the Agulhas Bank wave field. This dataset shows that **P** and **Hm0** has higher values during evenings and lower values during morning nearshore and the offshore **P** and **Hm0** values are higher during afternoons and lower during nights. However, the nearshore **Tm0** values are higher during mornings and lower during evenings, while the offshore values of **Tm0** are higher during nights and lower in the evenings.

Table 4- 4. Diurnal cycle of the wave field parameter and Pacross the four selected mooring sites (ADCP data)

		Hm0	Tm0	Mdir	Wave power density
Cape Agulhas	Hourly (Figure A35 to A37).	Lowest values from 22h to 01h (2.85 m); highest values occur from 09h (3.0 m); Peak around 13h (2.96 m)	Lowest values around 10h (10.44 s); highest value from 07h to 09h (~ 10.7 s)	Varied from the 225° southwest around 07h to 232° (19h and 20h)	Minimum around 20h 22h to 01h (42kW/m), to maximum from 09 (47kW/m) to 12h (46 kW/m) (Figure A38a).
	6 hourly	Lower in the evening and night (2.85 m) and higher in the morning and afternoon (2.95	Lower in the evening (6.64 s) and higher at night and in the morning (6.68 s). (Figure 4-		Lower in the evening (42 kW/m) and higher in morning and afternoon (44.5 kW/m), (Figure 4- 6ci).

		m). (Figure 4- 5ai and 6bi)	6ai and 6bi)		
Mossel Bay	Hourly (Figure A35 to A37)	Highest values are from 13h to 20h (2.63 m; Peak around 16h (2.65 m); Lowest values occur form 01h (2.6 m) to 6h (2.47 m)	Highest value at 07h (10.87 s) and 8h (10.85 s); Lowest values occur from 22h (10.66 s) to 00h (10.64 s).	Varied from the 220° southwest around 00h and 01h to 225° (07 to 18h)	Minimum t 05h ant 06h (32 kW/m) to a maximum around 13h (36 kW/m) 16h (37 kW/m) to 20h (36 kW/m) (Figure A38b).
	6 hourly	Lower at night (2.55 m) and higher in the afternoon (2.63 m). (Figure 4- 6cii).	Lower during the evening and night (6.86 s) and higher during the evening (6.9 s). (Figure 4- 6cii).		Lower in the night and morning (34 kW/m) and higher in the afternoon and evening (36 kW/m), (Figure 4- 6cii).
Tsitsikamma	Hourly (Figure A35 to A37)	Lower in the period from 04h (2.5 m) to 09h (2.48 m) and is higher around 12h (2.55 m) to 22h (the peak, 2.63 m)	Lower around 12h and 13h (10.7 s) and highest around 07h 09h (11 s), 20h and 01h (11.1 s)	Varied from the 225° southwest (from 06h to 06h) to 230° (13h to 15h).	Low values from 04h to 09h (33 kW/m) and higher values from 16h (36 kW/m) to 22h; Peak at 19h (above 37 kW/m). (Figure A38c)
	6 hourly	Lower in the morning (2.5 m) and higher in the evening (2.6 m) (Figure 4- 6aiii and 6iii).	Lower in the afternoon (6.7 s) and higher in the evening and night (6.9 s), (Figure 6aiii and 4- 6iii).		Lower in the morning (34 kW/m); Higher values in the afternoon (35 kW/m) and evening (36 kW/m). (Figure 4- 6ciii)
Cape Recife	Hourly (Figure A35 to A37)	Lower occur from 01h (2.49 m) to 10h (2.49 m); Highest values occur at 17h (2.67 m) to 23h (2.6 m).	Lower occur at 06h (10.85 s), 16h and 17h (10.8 s) ; Higher from 22h to 00h and from 09h 12h (11.2 s)	Varied from the 220° southwest (01h to 03h) to 230° at 17h	Lower from 01h to 10h (33 kW/m) and higher from 17h to 00h (36 kW/m); Peak at 18h (38 kW/m) (Figure A38d).
	6 hourly	Lower in the morning (2.5 m) and higher in the evening (2.6 m).	Lower in the afternoon (6.45 s) and higher at night (6.6 s).		Lower in the morning (33 kW/m); Higher in the evening (37 kW/m), (Figure 4- 6civ).

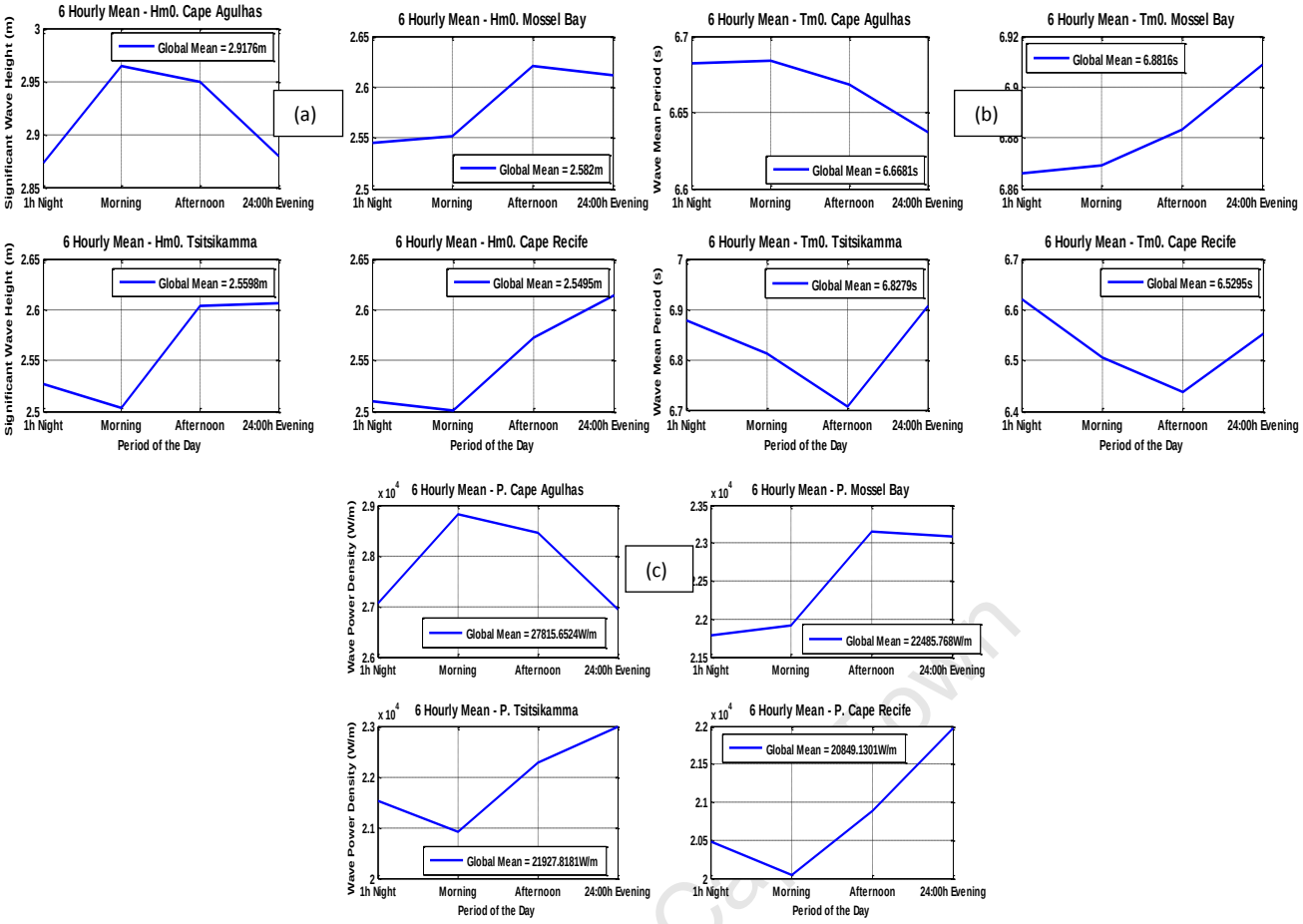

Figure 4- 6. Diurnal cycle (ADCP data), 6 hourly mean: (a) Significant wave height; (b) Mean Period; (c) Wave power density.

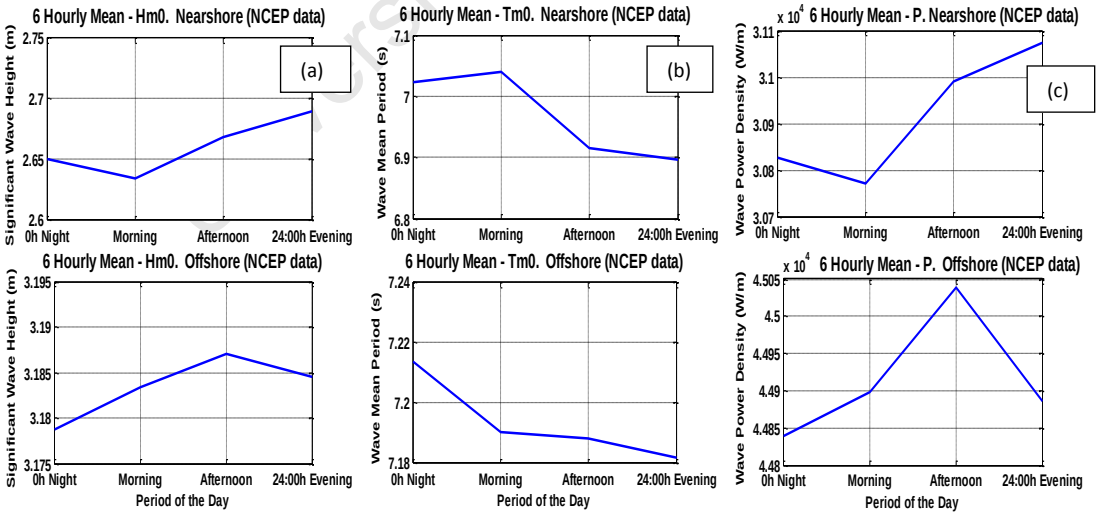

Figure 4- 7. Diurnal cycle (NCEP data), 6 hourly mean: (a) Significant wave height; (b) Mean Period; (c) Wave power density.

4.3 Description of the Agulhas Bank wave field based on the NCEP dataset

To better understand the availability of wave power density (**P**) across the Agulhas Bank, spatial and temporal analysis of the wave field parameter and **P** were conducted by analysing the Hindcasted wave data from NCEP – WAVEWATCH III. It is important to recall that these estimations were based on calculations of wave energy resource along the bathymetric contour near 128 m water depth because there is little difference between the values of the wave parameter measured in both 80 and 128 m bathymetric contours, moreover, by using the 128 m bathymetric contour it enable us to obtain a more precise and comprehensible characteristics of the wave field across the costal and offshore environments at once. Experiments conducted within this study suggest that the values of **Hm0** for the bathymetric contour of 128 m depth (corresponding to 35.5° S) differ in a factor of 6% to 11% from the values of **Hm0** for the bathymetric contour of 95.5 m (34.5° S).

4.3.1 Cumulative distribution of the wave field parameters and wave power density

The results show that most of the waves have **Hm0** in the interval between 2 and 6 m, however the 3 m waves are the most frequent followed by 2 m and 4 m waves (Figure 4- 8a and A34). The frequent waves have their **Tm0** in the interval between 6 and 9 s, being the 7 s waves the most frequent followed by 6 s and 8 s (Figure 4- 8b and A34). The also results show that most of the waves on the Agulhas Bank have their incidence direction from 210° to 260° southwest. The highest frequency of occurrence corresponds to waves heading from 230° southwest (Figure 4- 8c and A34). According to the cumulative distribution, most of the waves that occur across the Agulhas Bank have values of **P** varying from 10 to 80 kw/m and the peak occurrence frequency corresponds to waves with power density equal to 30 kW/m followed by 40 kW/m, 50 kW/m and 20 kW/m (Figure 4- 8d and A34).

In terms of cumulative probability distribution and technically recoverable resource it is observed that 60% of the waves have **Hm0** in the interval between 2 to 4 m (Figure 4- 9a); 70% of the waves have mean period in the interval between 6 to 8 s (Figure 4- 9b) and 85% of the waves have their mean incident direction from 210° to 250° southwest (Figure 4- 9c). And most important features is that more than 85% of the waves have values of **P** below 80 kW/m but only 15% of the waves are below 10 kW/m, which means that the **P** is more concentrated in the interval between 15 and 60 kW/m (Figure 4- 9d).

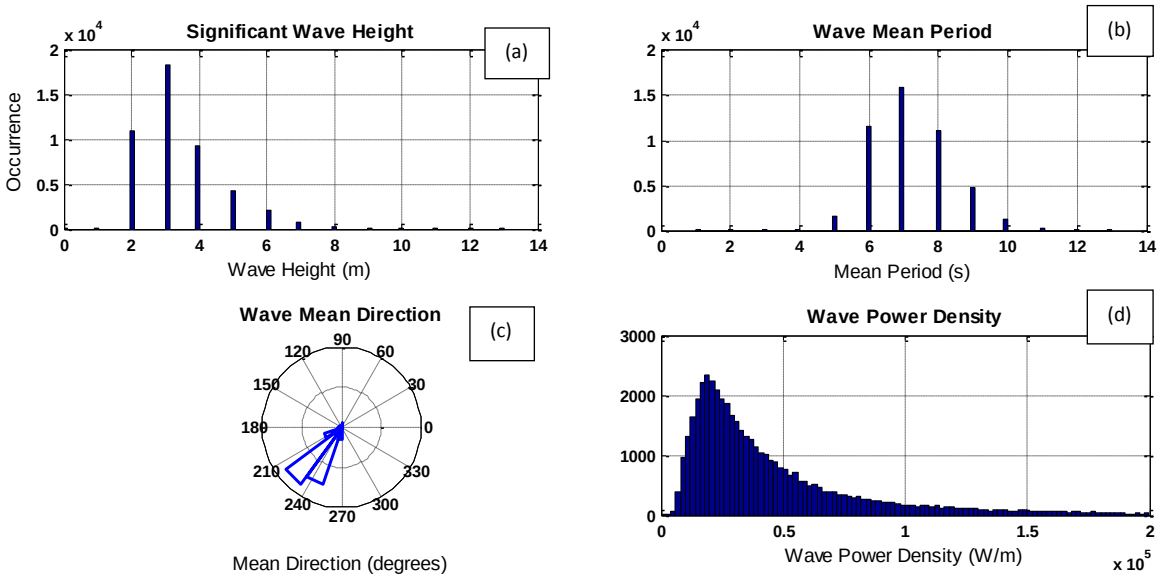

Figure 4- 8. Frequency of occurrence: (a) Hm0; (b) Tm0; (c) Mean direction; (d) Wave power density

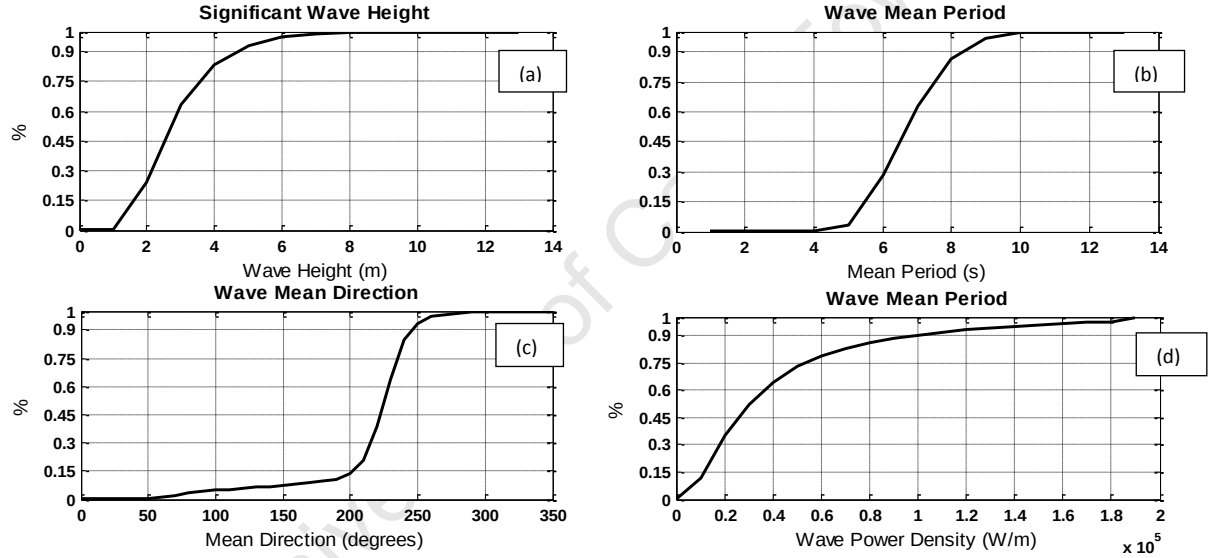

Figure 4- 9. Cumulative probability distribution: (a) Hm0; (b) Tm0; (c) Mean direction; (d) Wave power density

4.3.2 Seasonal and interannual variability

The time series obtained from the initial WAVEWATCH III data enabled us to plot 16 years of time series of wave parameter and the result show that the Agulhas Bank is characterised by waves with average **Hm0** of 3.40 m, average **Tm0** of 7.22 s and the wave direction is predominantly from southwest (Figures A31 to A33).

Averaging the initial monthly data (Equation 3- 5), the results reveal that the **Hm0** varied from 2.3 to 4.3 m with the mean equal to 2.97 m; the **Tm0** varied from 5.6 to 8.3 s with a mean equal to 7.1 s. The time series also show the seasonal and interannual variability of **Hm0** and **Tm0**. A bimodal regime is observed during the years 1997-1998, 2000-2001-2002-2003, 2006-2007. Moreover, most of the consecutive peaks and troughs have different amplitudes. From the monthly mean time series, it is

also observed that there are three peaks from 1994 to 1996, 1999 to 2002 and from 2004 to 2007. The troughs were observed in years 1997 and 1998, 2002, 2003 and 2009. The highest peak of **Hm0** in this time series occurred in 1995 followed by another in 2006, with the lowest occurring in 2003. The pattern of **Tm0** is similar to the pattern of **Hm0**, however, the interannual variability is not well pronounced in the **Tm0** time series as it is in **Hm0** (Figure 4- 10a).

Seasonally the **Hm0** varied from a low of 2.4 to a high of 3.9 m with an average of 2.97 m (Figure 4- 9b). In the same context, the **Tm0** varied from 6.4 to 8.3 s with an average of 7 s (Figure 4- 10c). During the seasonal mean analysis (Equation 3- 5), it is observed that from 1994 to 1997 the seasonal mean values of **Hm0** and **Tm0** were below the average, while from 1998 to 2001 the **Hm0** values fluctuated around the mean value. Between 2002 and 2006, the **Hm0** and **Tm0** values were above the mean values. From 2007 to 2010, the values of **Hm0** and **Tm0** were again below the mean but not as much as it was in the period from 1994 to 1997. The results also show that for the annual cycle, the **Hm0** has its lower value between December and January (2.5 m), staying low throughout all the summer season, but then in autumn it increases from 2.8 to 3.4 m. During the winter the **Hm0** reaches a maximum on July then decreases again as the year cycle progresses (Figure 4- 10d). The **Tm0** follows the same pattern, but has the lowest values of the mean period occurring in December (Figure 4- 10e). The wave mean and peak direction are dominant from the west (225° to 230° southwest) during winter season, July being the most westward month, and more from the south (190° to 210°) during the transitional seasons, March and October being the most southward months (Figure 4- 10f). With regards to the **P** across the Agulhas Bank, the results show that it varied between 8kW/m to over 200 kW/m with the mean equal to 50 kW/m (Figure A34).

After filtering and averaging the initial data monthly (Equation 3- 5), the results show that **P** vary from 15 kW/m to 74.8 kW/m with a mean equal to 32 8kW/m. Moreover, looking at the results of monthly mean of **P** across the Agulhas Bank over 16 years period, it is first seen that the troughs have almost the same pattern while the peaks varied year to year. The results also highlight that the values of **P** were higher in the years 1994 to 1996, 2002, 2007 and lower in the 1997 to 2001 and from 2003 to 2007 and 2009. The lowest peak value occurred in 2004 followed by 2003 and 1998, while the highest peak occurred in 2007 followed by 1994 and 1995. The highest trough values occurred in 2007 and 1998, with the lowest in 2005 and 1999 (Figure 4- 11a).

Averaging **P** seasonally (Equation 3- 5) from 1994 to 2010, the results show values that varied from 17 kW/m to 53 kW/m, with an average of 31.5 kW/m. An interannual variability is also observed in the seasonal mean of **P** across Agulhas Bank. Looking at the whole time series of the seasonal mean, one can see that from 1994 to end of 1997 the seasonal mean values of **P** is very much below the average while from 1998 to 2001 the values of **P** were mostly above the average value. The peak was reached between 2002 and 2006 when the seasonal values of **P** are between 31 and 52 kW/m. From 2007 to

2010 the values of **P** were mostly below the mean but not as much as it was in the period between 1994 and 1997 (Figure 4- 11b).

Similar to **Hm0 Tm0** and **Mdir** within an annual cycle, values of **P** are higher during the winter season with the peak occurring in July (~ 47 kW/m) and the trough occurring during summer where the lowest values occur in December (~ 20 kW/m). The transitional seasons are characterized by a fast increase of **P** from April (27.5 kW/m) to June (49kW/m) and a relatively slow descent in August (43 kW/m) and in October (28 kW/m) (Figure 4- 10c). The results also show that the period of time per annual cycle in which the values of **P** is above the annual mean is ~ equal to the period of time in which **P** is below the annual mean. Furthermore, the results show that during the annual cycle only three months have values below 25 kW/m (these are the summer months which corresponding to 25% of the annual cycle). Winter and spring (each has ~ 30 kW/m) contain 7.5% more of the total annual wave power density than the summer and autumn months. Most of the wave power density can be recovered from April to November, which corresponds to ~ 60% of the annual cycle (Figure 4- 10d).

By plotting the spatial distribution of wave parameter of the Agulhas Bank and by averaging each data point for the entire period of 16 years (Figure 4- 12), it is observed that the **Hm0** has relatively high values (> 3.5 m) offshore and decreases towards the shore following the bathymetric contours to ~ 1.25 m at 10 m depth (Figure 4- 12a). The **Tm0** has an average value equal to 7 s ain almost every nearshore area of the bank (Figure 4- 12b). Moreover, it appears that the southwest offshore region of the Agulhas Bank has **Tm0** equal to 8 s and the southeast offshore region has **Tm0** equal to 9 to 10 s. By averaging **P** at each data point for whole period from 1994 to 2010, it is observed that the distribution of **P** over the Agulhas Bank follows a simple pattern which accommodates the **Hm0** and **Tm0** distribution, with lower values ~ 10 kW/m in shoreline (~ 10 m water depth), then increases to 20 kW/m in nearshore (~ of 80 m), and 30 kW/m of shore (> 80 m water depth). From the mid shelf towards offshore, the values of **P** increase from ~ 40 kW/m between 130 and 500 m water depth to 50 kW/m on the deep ocean region in the edge of the Agulhas Bank (Figure 4- 12c).

During summer (Figure 4- 13c), high energy waves with high values of **P** concentrate outside of the Agulhas Bank leaving this region with waves of ~ 20 to 30 kW/m. The lowest value of **P** during summer (~ 10 kW/m) is observed shoreline. In autumn (Figure 4- 13a) the high energetic waves start to approach the bank. During this season, waves with 35 to 40 kW/m reach the mid shelf of Agulhas Bank along the 37° S, and nearshore the values of **P** oscillates between 10 and 20 kW/m. During winter (Figure 4- 13b) all the Agulhas Bank is covered by high energy waves. The entire region way from the coast at 35.5° S is under influence of 50 kW/m waves. The southwest region of the bank near Cape Agulhas receive 40 kW/m while most of the offshore area (are south of 35° S) is under influence of waves with **P** of ~ 40 kW/m. In spring (Figure 4- 13d), the high energy waves begin to retreat towards offshore leaving most of the area the bank with values of **P** of 30 kW/m. Only nearshore is

found values of **P** of ~ 20 kW/m. The wave distribution during spring is similar to the wave distribution during summer and winter. The only big difference is the magnitude of **P** which is lower in summer and higher in winter. However, the autumn season differs from the other seasons in the spatial distribution of **P** due to its intense gradient which displays lower values on the southwest side near Cape Agulhas and higher values offshore on the southeast side of the bank.

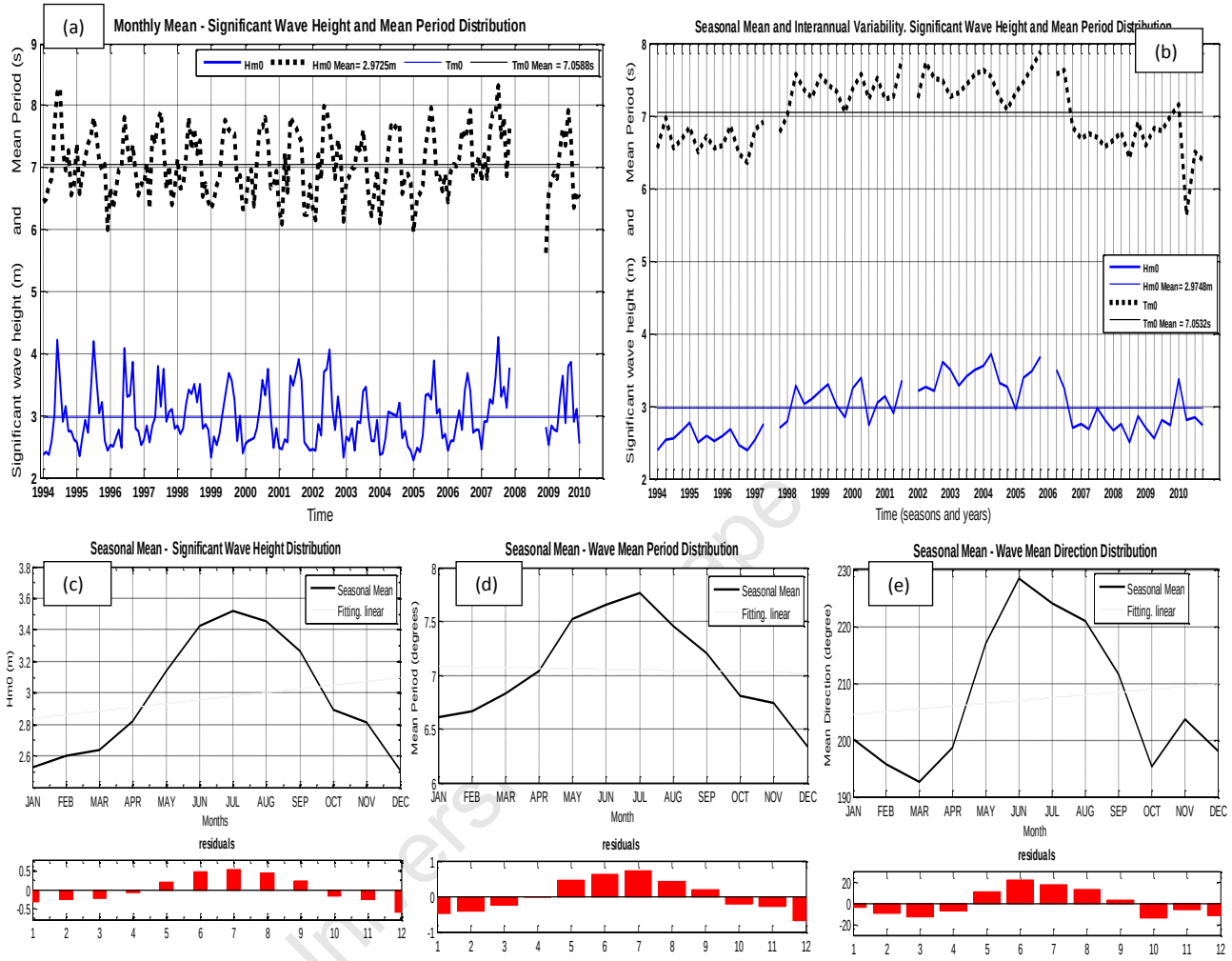

Figure 4- 10. (a) Monthly mean and interannual variability of Hm0 and Tm0; (b) Seasonal mean and interannual variability Hm0 and Tm0; (c) Monthly mean and seasonal variability of Hm0; (d) Monthly mean and seasonal variability of Tm0; (e) Monthly mean and seasonal variability of Mean direction.

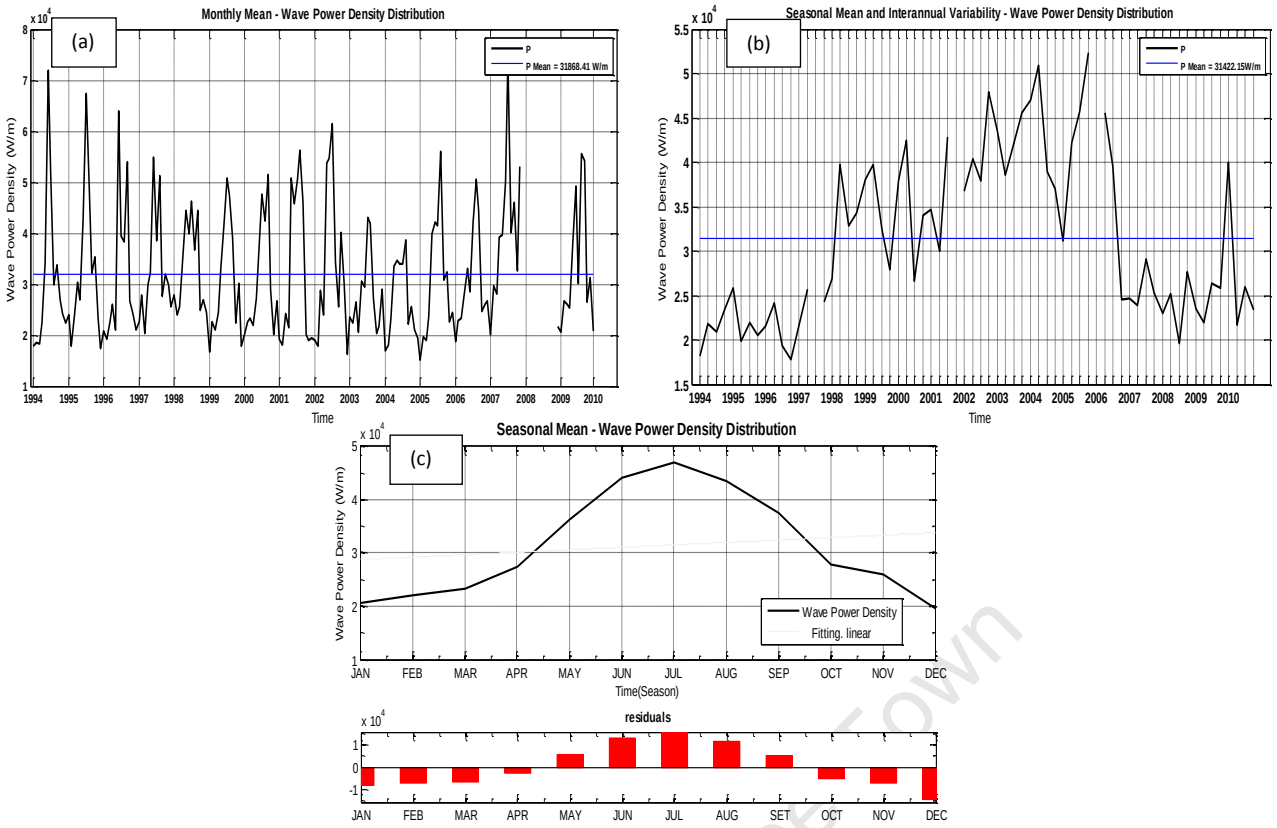

Figure 4- 11. Climatology of the wave power density: (a) Monthly mean and interannual variability; (b) Seasonal mean and interannual variability; (c) Monthly mean and seasonal variability;

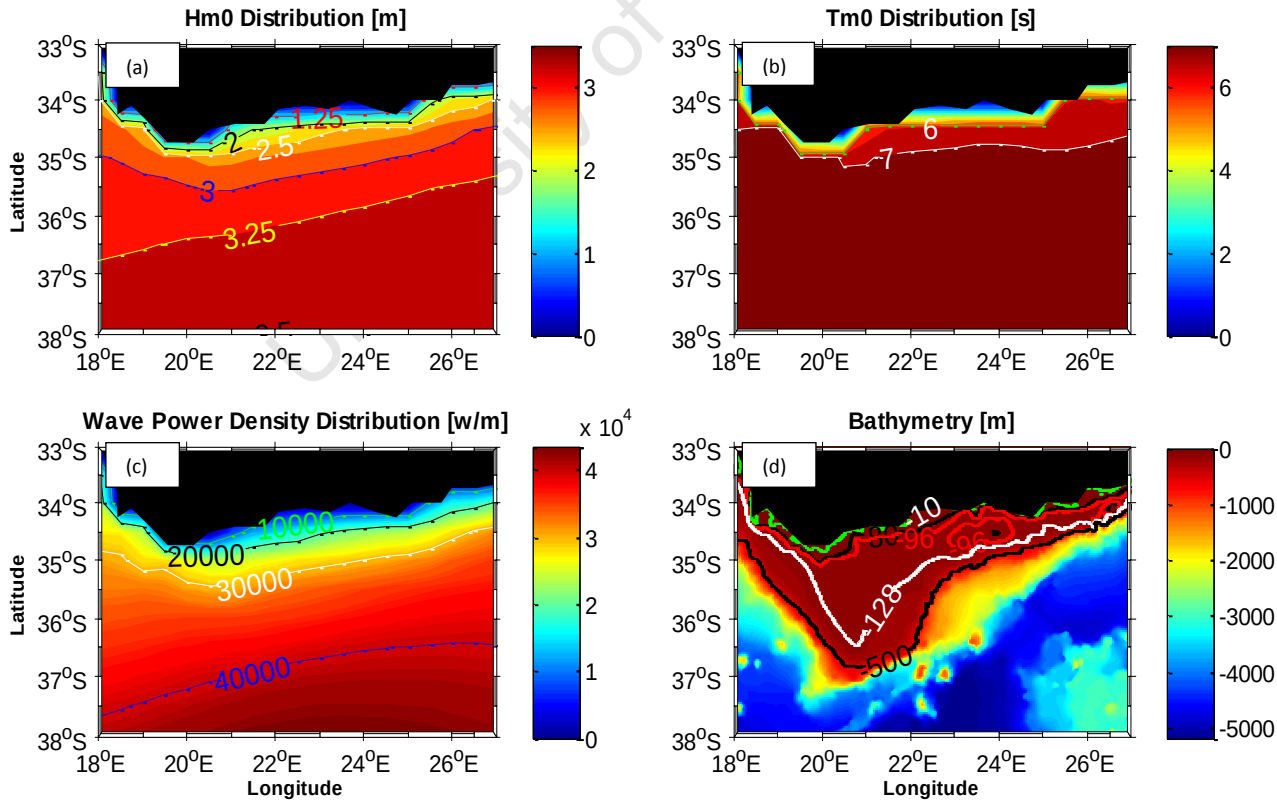

Figure 4- 12. Spatial distribution of: (a) Hm0; (b) Tm0; (c) Wave power density; (d) Bathymetric contours of interest.

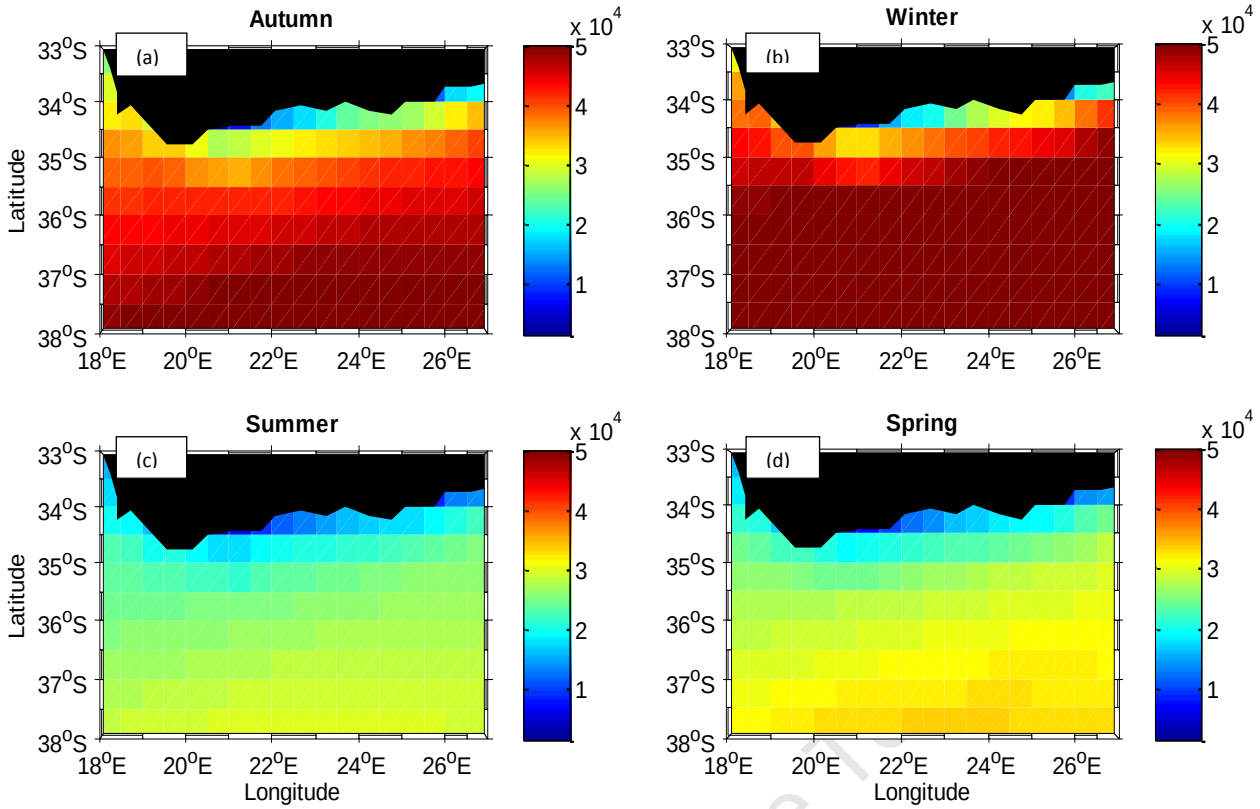

Figure 4- 13. Seasonal variability of wave power density (W/m) across Agulhas Bank: (a) Autumn; (b) Winter; (c) Summer; (d) Spring.

4.4 Long term wave field trends in relation to climate variables

The results show a considerable positive and negative correlation (Equation 3- 6) between **SLP** and **P** on the Agulhas Bank. The spatial correlation graph show that between the years 1994 to 2010 there was a positive and strong correlation (> +0.6) existed around 12° S to 24° S with the highest values (+0.8) along the west coast of Southern Africa over the Benguela Current System, and extends across the tropical Atlantic region to the west coast of South America. A relative strong negative correlation (> -0.4) was observed in the region around 48° S between the Greenwich Meridian and 25° E (Figure 4- 14a).

The results obtained from the CERSAT - QuikSCAT scatterometer wind field data (Figure 4- 14b), show that there was a strong positive correlation (> +0.6) between wind speed and stress and Agulhas Bank **P** in the regions around the equatorial Atlantic (0° S to 24° S, 40° W to 0° E), the Brazil Current, the Agulhas Current (in which the correlations prolongs towards the Brazil Current region), the South Atlantic Current, and the west coast of South America. A negative correlation (~ -0.6) was observed in the equatorial Atlantic region to the west African coast around 2° S to 14° S between 10° W to 15° E, and also around the southeast coast of South America around 36° S and 55° S.

There is a link between the meridional wind speed and values of **P** on the Agulhas Bank. The results from NCEP (Figure 4- 14e) show that between 1994 and 2010 there was a strong positive correlation of 0.6 around 12° S between 25° W and 50° W along the South American coast, and over a small region between 12° S to 24° S and 0° E to 10° E close to the west African coast of Angola. There was also a weak correlation of about +0.2 to +0.4 in the region south of 48° S. An extremely negative correlation (< -0.8) was observed in the region corresponding to the Agulhas Bank from 40° S to 28° E and 10° S to 25° E. Another negative correlation was observed on the same latitude but on the west coast of South America. The results from CERSAT - QuikSCAT wind speed and stress also (Figure4- 14f) show the same pattern of correlation, however, the magnitude of negative correlation produced by this dataset is lower and the wind stress correlation show some existence of positive correlation in the Agulhas Bank region (Figure 4- 14j).

The correlation between the zonal wind speed and **P** was almost opposite with the correlation with the meridional wind for the same NCEP time series. Very high correlations of +0.8 was observed just over the Agulhas Bank and slowly it weakens along the subtropical Atlantic region between the 0° W and 60° W and 24° S to 42° S, from the African to the South American coast (Figure 4- 14c). On other hand, negative correlation (-0.6) was observed around west coast of Africa just over the Benguela Current System, and it extends towards the central tropical Atlantic around 12° S. Negative correlation was also observed along the west South American coat from 24° S northwards. Similar to what happens with meridional wind speed, the results from CERSAT - QuikSCAT (Figure 4- 14d) also show almost the same pattern of correlation, however, the magnitude of negative correlation produced by the wind speed data is lower. With this data is observed a positive correlation (> +0.4) around 60° S and between 0° S to 12° S and 0° E to the west African Coast. The zonal wind stress also show a positive correlation over the westerlies region and around 60° S following the South Atlantic current (Figure 4- 14h).

There is a notable link between regional sea surface currents and **P** on the Agulhas Bank (the mechanism is explained in section 2.2.9, Equations 2- 21 and 2- 22). The results show a positive correlation (> +0.6) between **P** and regional meridional sea surface currents in the regions of the Agulhas Current, and also a strong positive correlation (~ +0.8) was observed in the western side of the southern Africa near the Benguela Current System, and also near the Brazil Current (Figure 4- 14i). Concerning the regional zonal sea surface currents, a high correlation of +0.6 to +0.8 was observed in the region of Agulhas Bank and Benguela Current System. This region of positive correlation extends from the southeast coast of Africa westwards along 34° S, reaching the South American coast. On the other hand, a negative correlation of -0.6 was observed near the eastern coast of South American coast and in the equatorial Atlantic region (Figure 4- 14g).

These results also show a strong and positive correlation (+0.6) between **P** and monthly mean **SST** anomalies over the major ocean basins in latitudes from 12° S to 20° N. The hot spots are located in the

regions of the eastern Pacific (80° W to 120° W), across the north of the North Australia, from the equator to 20° N and from 60° E to 140° E, and in a small region of central equatorial Atlantic (Figure 4- 14k). Weak negative correlation was observed in the Southern Hemisphere. These results suggest that there is a correlation between **P** on the Agulhas Bank and some climate parameters such as the Southern Oscillation Index (**SOI**), El Niño Southern Oscillation (**NINO3**), and Southern Annular Mode (**SAM**). By investigating the time series of these climate parameters in relation to **P**, the results are following: For **NINO3** (Figure 4- 14l, Figure A43), between 1994 and 2003 the correlation coefficient (**r**) was -0.17 and the regression ($\mathbf{R^2}$) was 0.03, and between 2002 and 2010 **r** was -0.28 and $\mathbf{R^2}$ was 0.08. For **SAM** (Figure 4- 14m, Figure A44), from 1994 to 2002 **r** was -0.33 and $\mathbf{R^2}$ was 0.11, and between 2002 and 2010 **r** was -0.19 and $\mathbf{R^2}$ was 0.03. And for **SOI** (Figure 4- 14n, Figure A45), a considerable **r** value of -0.16 and $\mathbf{R^2}$ of 0.13 occurred between 2002 and 2010.

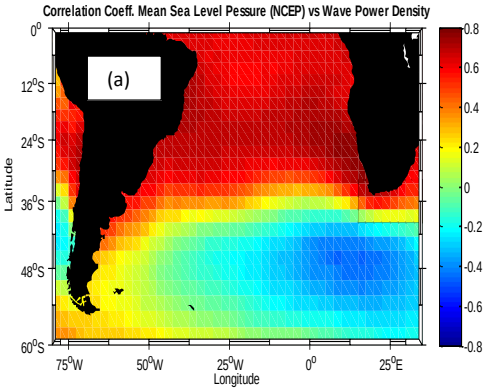

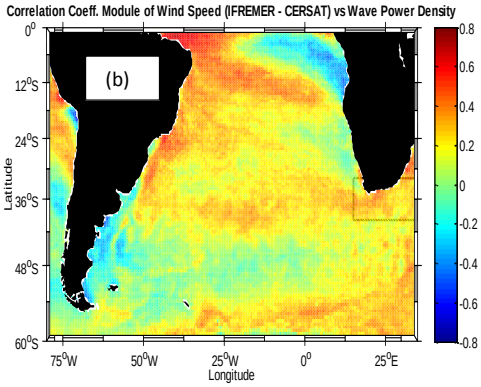

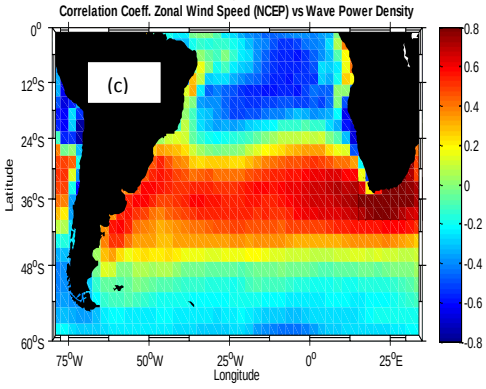

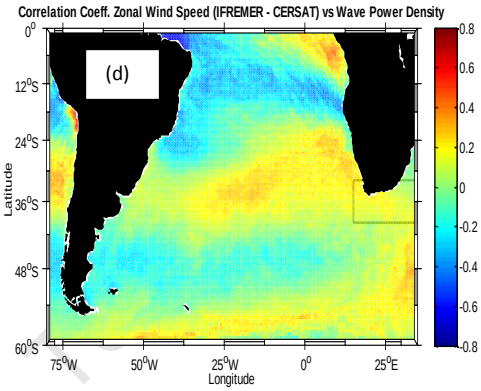

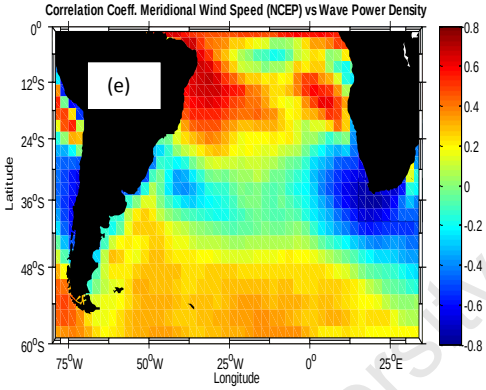

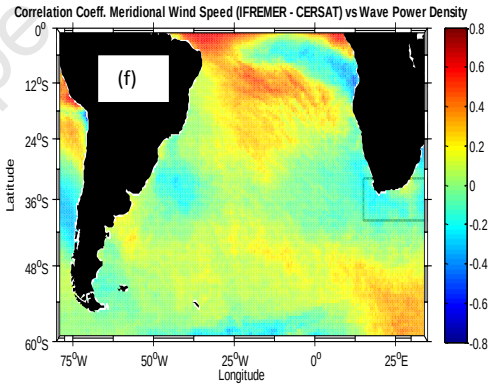

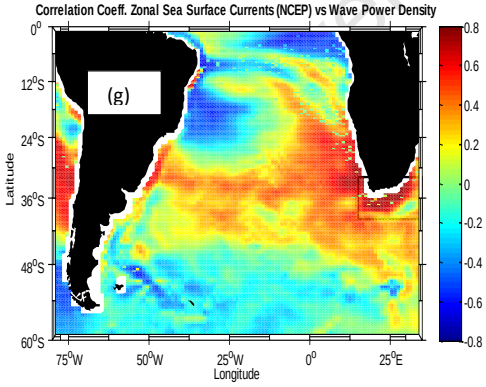

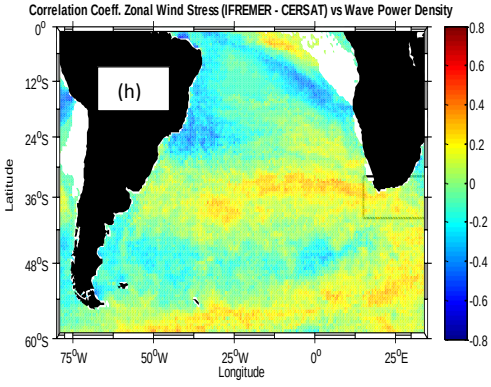

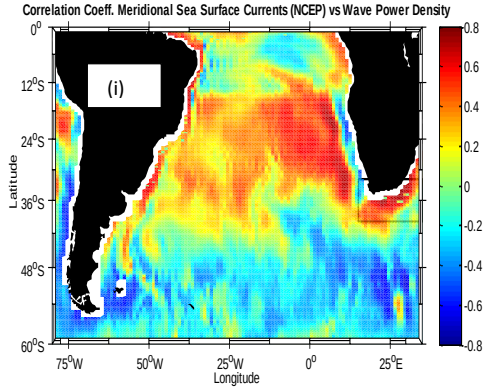

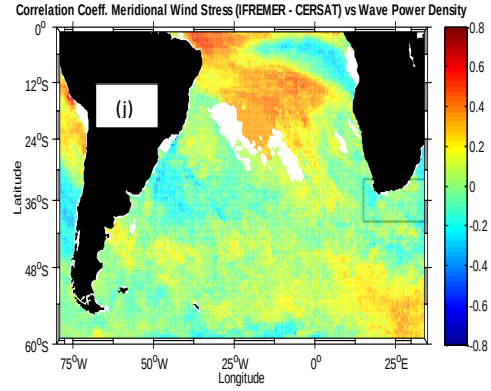

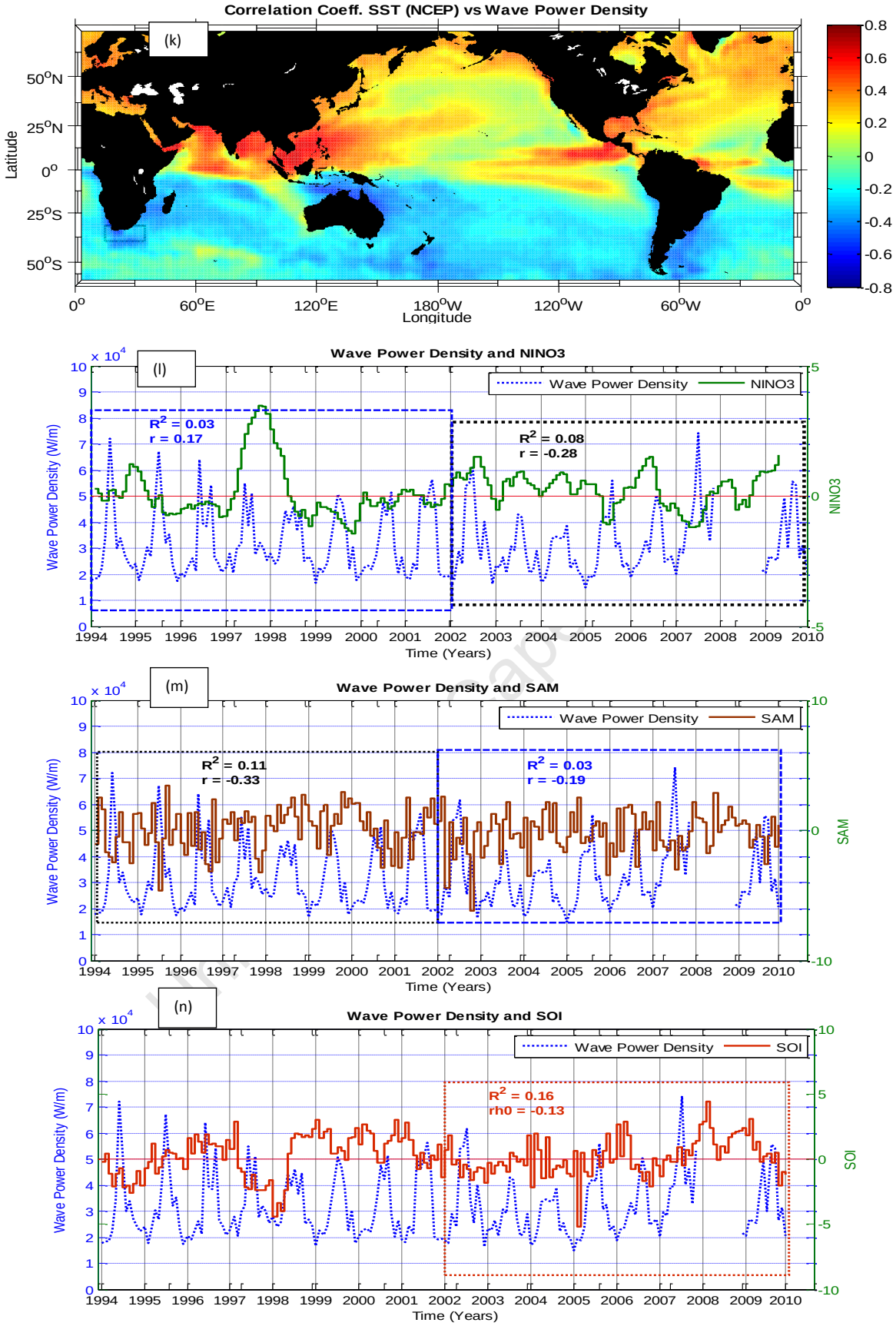

Figure 4- 14. Correlation coefficients between monthly mean P on the Agulhas Bank and monthly mean of: (a) SLP (NCEP); (b) Module of wins speed (IFREMER-CERSA); (C) Zonal wind (NCEP); (d) Zonal wind speed (IFREMER-CERSA); (e) Meridional wind speed (NCEP); (f) Meridional wind speed (IFREMER-CERSA); (g) Zonal sea surface currents (NCEP); (h) Zonal wind stress (IFREMER-CERSA); (i) Meridional sea surface currents (NCEP); (j) Meridional wind stress (IFREMER-CERSA); (k) Global SSTS (NCEP); (l) NINO3 (NCEP); (m) Southern Annular Mode (NCEP); and (n) Southern Oscillation Index (NCEP).

4.5 Wave energy resource across the Agulhas Bank

After assessing the wave field across the Agulhas Bank, it is now important to estimate the naturally available and the recoverable wave energy resource using the ADCP and NCEP data for short and long term timescales respectively. Both the naturally available and the recoverable wave energy resource were estimated using a total length of the bathymetric contour equal to 50 km for each selected site (Cape Agulhas, Mossel Bay, Tsitsikamma and Cape Recife), and for the total domain of the Agulhas Bank. The calculations used a total length equal to 1 000 km for the seasonal and annual cycles.

4.5.1 Naturally available energy resource

The total available wave energy resource (Equation 3- 41) corresponding to the ADCP measurements along the four selected mooring sites are presented in the Table 4- 2. These calculations were done using the total sampling time of 72 days. The total and regional available wave energy resource estimated using the long time series NCEP data for monthly, seasonally and annually cycles are shown in Table 4- 5, Table 4- 6, and Table 4 -7 respectively. The results show that the total annual naturally available wave energy near 128 m water depth is ~ 383 TWh/yr.

Table 4- 5.Total available wave energy resource corresponding to the 90 days ADCP data (t ~1 728 h and L ~ 50 km)

Cape Agulhas	Mossel Bay	Tsitsikamma	Cape Recife
2.7 TWh	2.3 TWh	2.2 TWh	2.0 TWh

Table 4- 6. Total naturally available wave energy resource breakdown by region and by month (t ~ 720 h and L ~ 333 km)

Region	JAN	FEB	MAR	APR	MAY	JUN	JUL	AUG	SEP	OCT	NOV	DEC
southwest	6.6 TWh	7.1 TWh	7.4 TWh	8.7 TWh	12 TWh	14.5 TWh	15.4 TWh	14.2 TWh	12 TWh	8.8 TWh	8.3 TWh	6.2 TWh
South	6.8 TWh	7.2 TWh	7.8 TWh	9 TWh	12 TWh	14.4 TWh	15.6 TWh	14.4 TWh	12.6 TWh	9.4 TWh	8.6 TWh	6.2 TWh
southeast	7.4 TWh	7.8 TWh	8.6 TWh	10.1 TWh	13.4 TWh	15.8 TWh	17.3 TWh	16.2 TWh	14.1 TWh	10.8 TWh	9.4 TWh	6.5 TWh

Table 4- 7. Total naturally available wave energy resource breakdown by region and by season (t ~ 2 880 h and L ~ 333 km)

Region	Summer	Autumn	Winter	Spring	TOTAL
Southwest	21.1 TWh	35.0 TWh	41.6 TWh	23.4 TWh	121.2 TWh/yr
South	22.0 TWh	35.4 TWh	42.7 TWh	24.34 TWh	124.5 TWh/yr
Southeast	24.0 TWh	39.3 TWh	47.6 TWh	26.8 TWh	137.6 TWh/yr
TOTAL	67.0 TWh	109 TWh	132.9 TWh	74.6 TWh	383.4 TWh/yr

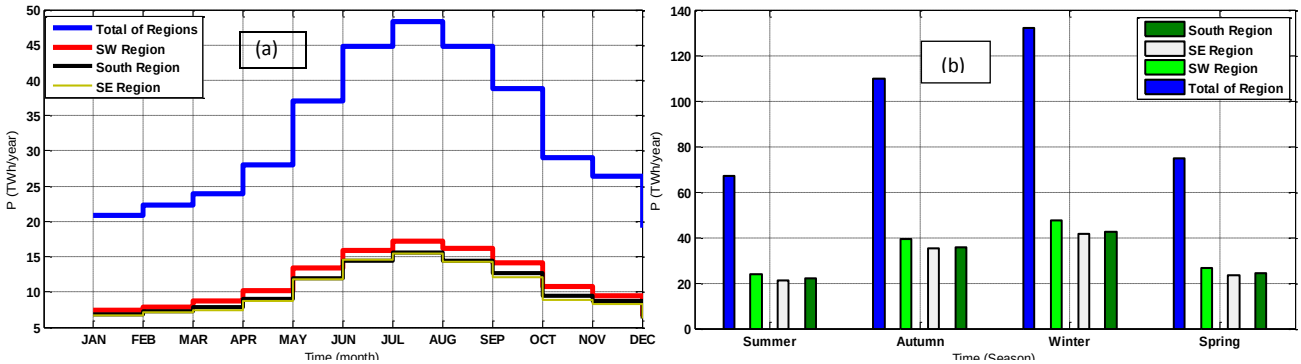

Figure 4- 15. Naturally available wave energy resource across the Agulhas Bank: (a) Total per month for each region (green, black and red lines) and total per month of all regions (blue line); (b) Total per season for each region (the short bars) and total per season of all regions.

4.5.2 Recoverable wave energy resource

To assess the quantity of the wave energy resource that can technically be converted into useful work by a WEC, the cumulative probability distribution was calculated using ADCP and NCEP data set. Table 4- 8 shows that Cape Agulhas has the greatest recoverable wave energy, followed by Mossel Bay, Tsitsikamma, and Cape Recife. Using the NCEP data set to do the long term analysis of recoverable wave energy, the entire domain of the Agulhas Bank were divided into three regions the southwest region, the south region and the southeast region, as it was done to estimate the total naturally available resource. The southeast regions has ~ 63%, for South region has ~ 69%, the southwest region has 83%, and the entire domain has 73%. Moreover, each km of the 128 m bathymetric contour on the Agulhas Bank can provide a recoverable wave energy resource in the interval between 1.0 and 8 MW (Figure 4- 16).

Table 4- 8. Recoverable wave power density resource estimated using short term ADCP dataset

	Cape Agulhas	Mossel Bay	Tsitsikamma	Cape Recife
Minimum	10 kW	7 kW	7 kW	7 kW
Average	62%	49%	49%	44%
Maximum	80 kW	80 kW	80 kW	80 kW

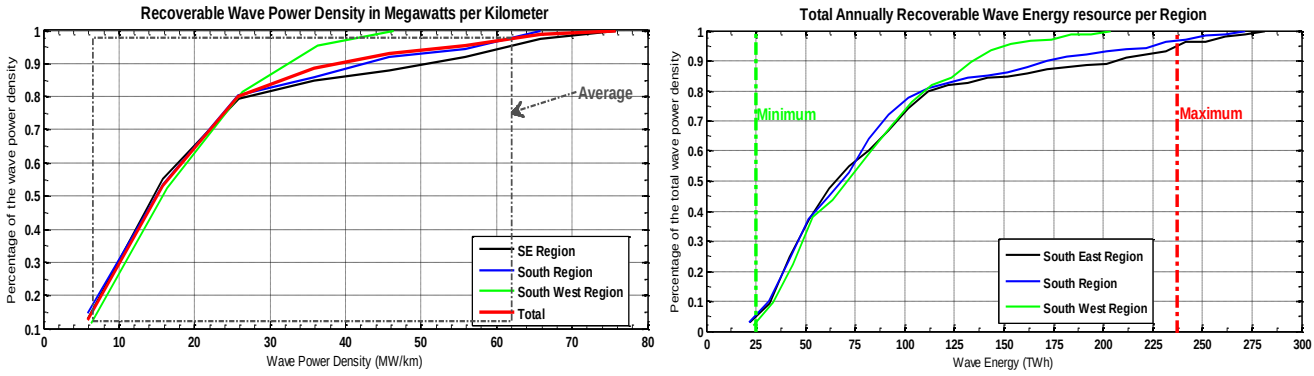

Figure 4- 16. Total annually recoverable wave power density along the 128 m bathymetric contour on the Agulhas Bank: (a) Average wave power density field per km; (b) Cumulative percentage for the wave energy per region.

4.6 Estimation of the necessary power for the pump storage scheme

To know if the available **P** is sufficient to be converted into useful work (mechanical or electricity) , i.e. to pump sea water into a reservoir atop an mountain, this study conducted experiments to estimate the necessary power (Equation 3- 8) for a given head (effective height in m), flow rate (in m^3s^{-1}) and efficiency (ratio of output and input power), and selected three different heads (**H**) of 100, 250 and 350 m, three different flow rates (**Q**) of 1, 50 and 100 m^3 and two different values of efficiency (**η**) of 80% and 85%.

These results (Figure 4- 17a) show that there is a linear dependency between the power supplied ($\mathbf{P_{PSS}}$) and the **H**, **Q** and **η**. For a small flow rate of 1 m^3s^{-1}, the necessary power supply to pump sea water 100, 250 and 350 m up into the upper reservoir with 80% of efficiency will be ~ 0.8, 2.0 and 2.8 MW respectively and by considering an efficiency of 85%, the values of $\mathbf{P_{PSS}}$ would be 0.85, 2.1 and 2.9 MW respectively. For a decent flow rate of 50 m^3s^{-1}, the values of $\mathbf{P_{PSS}}$ necessary to pump sea water 100, 250 and 350 m up into the upper reservoir with an 80% of efficiency will be ~ 40, 100 and 140 MW respectively and if the efficiency is 85%, then the values of $\mathbf{P_{PSS}}$ are 43, 107 and 150 MW respectively. And for a relatively large flow rate of 100 m^3s^{-1}, the necessary power needed to pump sea water 100, 250 and 350 m up with an 80% of efficiency will be ~ 80, 201 and 281 MW respectively and by considering an efficiency of 85% the values of $\mathbf{P_{PSS}}$ would be 85, 213 and 299 MW respectively.

To assess the optimum pumping power range which suits the input local wave power density, characteristics of the reservoir and pumping time, this study selected three volumes for the reservoir (**V**) of 5, 10 and 15 million m^3 and three flow rates of 1, 50 and 100 m^3 respectively. These results clearly show that the bigger the rate flow, the least time is needed to fill reservoir. Hence, if the flow rate is 1 m^3s^{-1} then the time to fill a reservoir of 5, 40 and 15 million m^3 will be ~ 62.5, 112 and 175 days respectively. And , if the flow rate is 50 m^3s^{-1} then the time necessary to fill the same volumes will be ~ 27, 55 and 83 hours respectively. However, for flow rates of 100 m^3s^{-1}, the time to fill the same reservoirs would be ~ 13, 27 and 41 hours respectively (Figure 4- 17b).

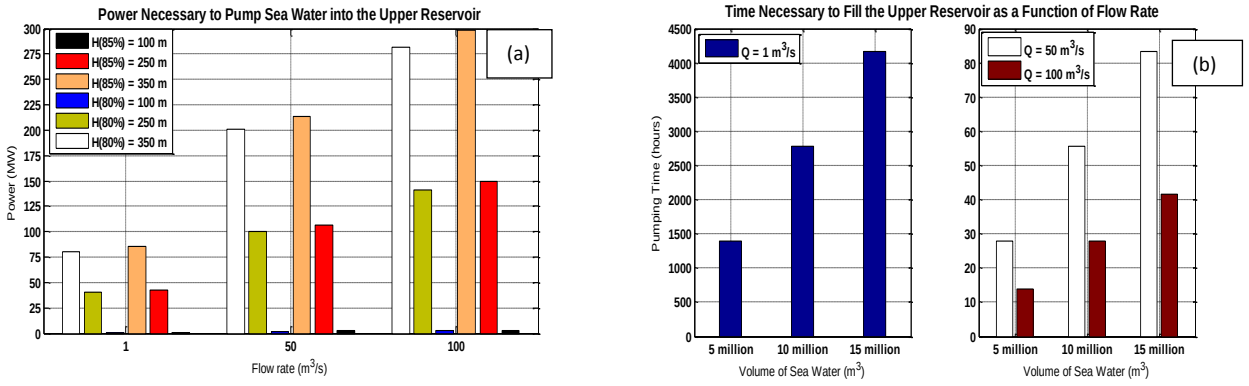

Figure 4- 17. (a) Estimated necessary power to pump sea water into a upper reservoir given a Head and flow rate; (b) Estimated necessary time to fill up the upper reservoir given a flow rate and reservoir volume.

Chapter 5

Discussion

The Agulhas Bank region can be characterised as having three wave climates the "west and east coast swells, and the winter storm wave". These three wave climates are characterised by several sea states described below.

The most dominant waves the Agulhas Bank are those which come from the southwest direction and constitute the southwest sea state. These waves originate from extra-tropical storms generated by low pressure systems over the sub-polar regions around 60° S. These systems occur throughout the entire year. The effect, however, on the Agulhas Bank is less intense during summer and more intense during winter as the sub-polar belt moves northwards to latitudes around 40° S. The characteristics of the southwest sea state are, waves with **Hm0** ranging from 2 to 5 m and **Tm0** ranging from 6 to 9 s, which corresponds to a **P** varying from 12 to 110 kW/m. During summers when the sea storms are reduced and the influence of the strong Westerly winds are less, the southwest sea state is mostly characterised by medium size southwest swell and seas generated locally by coastal winds. During this season, the typical **Hm0** is on average 2.5 m nearshore with a typical mean period is 6.5 s and typical values of **P** between 20 kW/m nearshore and 60 kW/m offshore. During this season cold fronts associated with the sub-polar low pressure systems can sometimes migrate far enough north to bring higher waves to the bank (Rossouw et al 1982). However, during winter, the southwest sea state is highly energetic and rough. The strong Westerly winds are predominant over the Agulhas Bank and are intensified by the nearby sub-polar through and by coastal fronts associated with low pressure centres which regularly migrate from west to east along the coast. During this season, large southwest swells cover the Agulhas Bank and the local sea waves are high due to the regular passages of these cold fronts. During winter, the typical southwest nearshore sea states is characterised by an average **Hm0** of 3.4 m and an average **Tm0** of 7.5 s with a wave power density of 45 kW/m.

The Southerly sea state can be considered the second most dominant on the Agulhas Bank wave field. This sea state is related to the seasonal position and strength of the "two high pressure cells" the South Atlantic High off the west coast and the South Indian Ocean High off the east coast. These two high pressure systems have seasonal shifts which add more energy into the wave field during winter when they are located to the north, and bring calmer seas during summer when the high pressure system shift southwards. During the austral summer, the Southerly winds on the west coast are often strong and persistent, while on the south and southeast coast are more influenced by southerly and easterly winds. The characteristics of the Southerly sea state are medium size Southerly swells with **Hm0** of 2

m, **Tm0** of 6 s (12 kW/m nearshore), with often large waves from the southwest capable of over 40 kW/m and seas of 0.5 m.

Calm seas over the Agulhas Bank mostly occur during summer and transitional periods. However, during winter, calm seas may occur for a few days when the high pressure centre over the land moves southward favouring the northeast winds. During summer, the north-easterly winds are dominant and are strong along the east coast. During this season, the Southerly and northeast winds propagate in phase with the Agulhas Current, which occasionally are also in phase with the propagation of the swells. This leads to an attenuation of wave height calming the sea surface. Characteristics of the calm sea state are small southerly swells with **Hm0** less than 1 m. The **P** in these conditions is < 12 kW/m nearshore.

As mentioned above, storms over the Agulhas Bank are more frequent during winter with July being the stormiest month and they are less frequent during the transitional months of April and November. The frequency of occurrence of stormy sea states explains the annual variability in the wave direction. During winter, the wave mean direction is more westerly (230°). In summer, the wave direction swings to southwards (200°), but during the transitional periods around March and October, the wave direction is more southerly (190°). This suggests that most of the storm waves travel from southwest. This, however, is opposite to what happens on the east coast near Durban where the tropical storms including cyclones influence the sea state mainly during October and May (MacHutctchon 2006). Stormy seas produce values of **P** > 120kW/m in the nearshore and > 200 kW/m offshore.

Overall, the Agulhas Bank can be classified as a highly energetic wave region. From the coastline to the deep ocean, the average **P** across the Agulhas Bank is ~ 20 kW/m in shoreline (at ~ 10 m water depth), 30 to 40 kW/m nearshore (at ~ 80 m water depth) and over 50 kW/m offshore. It is important to note that the shoreline values of **P** resource are site specific and, in some locations such as St. Helena Bay and Hangklip, the values can reach an average of 39 to 41 kW/m (Joubert 2008). The southwest region has the most energetic wave field, with Cape Agulhas having the most energetic site followed by Mossel Bay. The intensity of the wave field decreases towards the east, resulting in Tsitsikamma and Cape Recife having less energetic wave fields compared to the western sites.

In terms of cumulative distribution of **Hm0**, our results showed that it follows a binomial distribution. The Cape Agulhas **Hm0** distribution spectrum is the widest followed by Cape Recife, Mossel Bay and Tsitsikamma. The cumulative distribution analysis also confirms that higher waves are more frequent in the southwest region, i.e. the Cape Agulhas wave field has the most frequent waves ranging between 2.3 and 2.7m, while at Mossel Bay the most frequent waves have an **Hm0** of 2.1 m. An important feature of this cumulative distribution is that it shows for all the wave fields studied, that the **Hm0** is not lower than 1 m. Cape Agulhas and Cape Recife had a minimum **Hm0** > 1.3 m. These findings are similar to those of MacHutchon (2006) who that the most frequent waves at Cape Point had **Hm0**of 2.5

m and the minimum was 1 m. For the Agulhas Bank region, he found that waves with **Hm0** of 2.0 and 2.5 and 3.0 m are the most frequent and the minimum **Hm0** at Cape Agulhas was near 1 m. Joubert (2008) found that the most frequent waves at Cape Point have **Hm0** of 2.7 and 3 m, while going northwards both from west or east coasts, the highest frequency of occurrence has waves with **Hm0** of 2 m, meaning that the **Hm0** is higher in the south over the Agulhas bank.

The diurnal cycle indicates that for the same period of day the occurrence of high waves on the W region of the Agulhas Bank is out of phase with the occurrence of high wave on the eastern region. It was also observed that the occurrence of higher and lower waves is advanced by ¼ of a day offshore in relation to nearshore, meaning that, the peak of **Hm0** is higher in the afternoon offshore and in the evening nearshore. However, the 90 days ADCP data shows a diurnal cycle characterized by values of **P** which vary from a minimum during night and morning and a maximum during the afternoon and evening for the south and southeast region of the bank. For the southwest region of the bank, a maximum occur in the morning and a minimum occur during evening and night. This may be related to shifts on the wind direction due to the influence of coastline agents near Cape Agulhas.

On average winter is the most energetic season (during July the peak is ~ 50 kW/m nearshore) and summer is the least energetic season (during December and January **P** is ~ 20 kW/m nearshore). On average, the values of **P** are not < 20 kW/m for the entire domain. Although, not totally conclusive, this study found that the interannual variability of **P** may be mostly driven by the annual variability of **SLP** and also is related to local and regional surface winds and currents. Large scale climate mode such as El Niño Southern Oscillation (**ENSO**) and the Southern Annular Mode (**SAM**) appear to influence the wave characteristics.

The naturally available **P** along 34.5° *S* (which corresponds to water depths between 80 and 128 m) cross the Agulhas Bank is on average 380 TWh/yr. Approximately 80% of this energy (over 30 MW/km) can be technically recovered and about 10 to 25 % can be converted into useful work. Winter (~ 140 TWh) and autumn (~ 110 TWh) contribute the largest **P** resource, summer (~ 70 TWh) and spring (~ 80 TWh), however, contributes less.

According to our data analysis, the naturally available **P** resource across the Agulhas Bank is on average high throughout the entire annual cycle. This study also finds that for discrete phenomena such as surface wind waves, the most appropriate statistical quantity to be considered is the frequency of occurrence (mode) of each wave parameter for a certain period of time, and not the average (mean). The average can be an excellent indicator for long term climate studies purposes, however for the wave energy conversion purposes the most important aspect is the characteristic of the instantaneous sea state. In other words, it is important to know, within a group of waves, how many have the minimum useful energy content? In this regards, the cumulative analyses done in this study easily demonstrates that for any given period of time, across the Agulhas Bank, most of the incident waves have **P** > 30 kW/m nearshore.

This study, therefore, clearly finds that the Agulhas Bank wave field comprises a consistently energetic wave climate in which wave energy farms can be successfully implemented.

The above findings also indicate that the **P** across the Agulhas Bank can be converted into mechanical or electrical energy to supply a pumped storage scheme. It was estimated that for the Agulhas Bank **P** resource, a moderate flow rate of ~ 50 m^3s^{-1} would be adequate to pump sea water into an upper reservoir with a head varying from 100 m to 350 m in a relatively short period of time. The later could vary from ~ 10 h to 80 h depending on the volume of the reservoir which for this specific study 5, 10 and 15 million m^3 were selected.

As previously indicated, the Agulhas Bank wave field is also directly influenced by several other factors such as the regional **SLP**, surface winds and currents, **ENSO**, **SAM** and tropical Atlantic **SST** variability. The influence of regional **SLP** is directly related to the surface winds. A negative correlation between SLP and **P** is observed in the region of the westerlies and a positive correlation is observed in the trade wind region. This means that the decrease in the **SLP** over the mid latitude (38° S to 60° S) areas leads to an intensification of the westerlies which consequently may increase the **P** on the Agulhas Bank. The variability of the regional SLP may be directly associated with the Southern Annular Mode (**SAM**) (Arblaster et al 2005, and Thompson et al 2002).

The **SAM** may be associated with **P** on the Agulhas Bank, since there is a tendency of the negative **SAM** phase to be associated with high values of **P** and vice versa. It was observed that from 1997 to 2001 and from 2003 to 2005 and again in 2007, the values of **P** over the Agulhas Bank were lower and for the same periods the **SAM** index was in its positive phase. Furthermore, wavelet analysis suggests that the strong seasonality of **SAM** may be one of the major factors influencing the seasonal and interannual variability of **P** across Agulhas Bank. The strong relation between **SAM** and **P** over the Agulhas Bank may be due to the negative phase of the **SAM** index is associated with the intensification of the westerlies near 35 to 45 ° S and increases in the frequency and intensity of storms. This is caused by the increase of SLP over Antarctica and decrease of SLP over the middle latitudes. The positive phase of **SAM** is associated with less storms over the mid-latitudes (Gillett et al 2006, Arblaster et al 2005, and Thompson et al 2002), which leads to calm seas therefore, low values of **P**.

There is a positive correlation between the meridional and zonal sea surface currents and **P** on the Agulhas Bank. This is consistent with the correlation with surface wind speed and stress. The Agulhas Current has strong signals in both the meridional and zonal directions. Since the main wave direction is from the southwest, it opposes the flow of the Agulhas Current. As a result of the presence of westerly winds, southwest swells and northeast Agulhas Current, the **Hm0** and the wave steepness over the Agulhas Bank increase leading to an increase in **P**. On the other hand, because the Benguela Current flows northwards, its direction is in phase with the predominant wave direction and is also in

phase with the surface meridional winds so that intensification of any of these two meridional components leads to a decrease in **P** on the Agulhas Bank.

Equatorial SSTs around the globe are positively correlated to **P** on the Agulhas Bank. Strong signals are observed north of Australia and in the eastern equatorial Pacific. This suggests that anomalies in the SST are also related to the **P** on the Agulhas Bank. By comparing the monthly mean **NINO3** with the monthly mean **P** fluctuations for the period between years 1994 to 2010, it was observed that there is a tendency of positive **NINO3** years being related to low values of **P** over the Agulhas Bank. Moreover, the results from the wavelet analysis showed that the 5 year period of interannual variability of **NINO3** and **SOI** may strongly influence the interannual variability of **P** on the Agulhas Bank. This was highlighted by the strong positive correlation between these two quantities which occurred between 1996 and 1999 and between 2006 and 2010. Moreover, data analysis also shows that higher values of **P** were correlated to **La Niña** years and lower values of **P** were correlated to **El Niño** years. Thus, **ENSO** influences appear to exist. Variability of the tropical South Atlantic (**TSA**) **SST**s also seems to play a role in the wave climate over the Agulhas Bank.

5.1 Comparison between these results and previous studies worldwide

In the recent past, several studies in wave energy have been conducted in different locations across the globe. Places such as Norway, Japan, China, India, Denmark, Sweden, Portugal, Netherlands, Korea, Indonesia, Republic Ireland, Israel and Cape Verde "have on-going wave energy conversion projects". Most of these projects are running as prototypes. In Portugal, Spain, the United Kingdom, the United States of America, Australia and Italy, wave energy farms (WEF) are operating or are about to operate for commercial purposes. Having evaluated the wave energy resource on the Agulhas Bank, it is important to compare these results with other regions. Two regions were selected taking in account the actual stage of utilization of wave energy, geographical location and climate similarity or discrepancy.

Portugal was the first nation to implement a commercial wave energy farm. In 2008, three Pelamis wave devices were deployed 5 km offshore of Póvoa de Varzim in Portugal to constitute the Aguçadoura Wave Energy Farm, producing a 2.25 MW of total installed capacity. Portugal has values of **P** of 45 kW/m offshore and ~ 30 kW/m at water depths of 50 m (Cruz et al 2004). These values of **P** suggest that this nation has a medium-high wave energy potential within the world ranking. On the other hand, South Africa has annual average values of **P** of ~ 50 kW/m offshore and ~ 32 kW/m at 50 to 130 m of water depth. Making a good case for this country to move into a prototype phase.

The similarity in the values of **P** can be related to the similarity in the location of each nation in to the equator (Portugal 34° N to 43° N and 34° S to 40° S for Agulhas Bank). In both locations, the predominant winds are westerlies. The differences between the Portuguese wave field and the

Agulhas Bank wave field are due to the distinct coastline shape and shelf width. Across the northern Portuguese wave field, 95% of the waves have **Hm0** greater than 1 m and only 5% have **Hm0** greater than 4 m (IM 29-02-2004). Most of the waves in this sub region are generated in the North Atlantic while others are generated by local north and northwest winds with period ranging from 7 to 10 s. The small waves are mostly generated by offshore swells produced by high pressure centres over the land which force winds to blow from the land (i.e. offshore) causing calm seas during the summer (IM 29-02-2004). During summer, the diurnal cycle is characterised by higher waves in the afternoon decreasing in amplitude towards the next morning. The high values of **Hm0** over the north region of Portugal occur more during the winter and transitional months and are related to the northeast anticyclone at northeast Azores and northwest post frontal depression (IM 29-02-2004). The highest values of **Hm0** and **Tm0** are associated with Westerly storms which occur when the polar front moves down to the mid-latitudes, bringing waves as high as 7 m and long as 16 s (IM 29-02-2004, Vitorino et al 2002). The sea states over the southern Portuguese waters are more associated with meteorological conditions originating on the west coast or by western storms which bring waves with **Hm0** between 2 and 3 m and **Tm0** between 7 and 8 s (Vitorino et al 2002). In this sub-region, the southeast sea state is associated with eastern Atlantic winds and southeast winds originated from the Gibraltar Strait. However, the most dominant sea state over the southern Portuguese coast is generated by local breezes in which **Hm0** increases from morning to the afternoon (IM 29-02-2004, Dodet et al 2010).

Comparing the predominant **Hm0** and **Tm0** values for both the Portuguese and Agulhas Bank wave fields, the Agulhas Bank has higher values of **Hm0** than the Portuguese wave field, but the **Tm0** is relatively lower by ~ 1 to 2 s, which means that on the Agulhas Bank, the values of **P** are much higher offshore and less nearshore compared with Portugal.

In the southern hemisphere, Australia is the most advanced in implementing wave energy converter systems. In Australia, two on-going wave energy farms are presently being tested and developed for commercial use. One is *CETO technology* operated by *Carnegies Wave Energy Limited* an Australian wave energy technology developer company. This farm located on the Western Australian coast at Carden Island, is designed to produce 2 MW of installed capacity (Orchison 2010, CETO 2012). Other wave energy farm located near Portland (Victoria), will be operated by *Ocean Power Technologies (Australia) Pty Ltd* and is set to produce 19 MW of electricity.

The south coast of Australia is one of the most energetic regions in world (see Figure 2- 3). It has a **P** resource of 35 to 50 kW/m at 25 m water depth, and 50 kW/m across all southern margins. The total annual resource is ~ 1.329 TWh/yr (Hemer et al 2010, CSIRO EP-126167 2012). These values of **P** across southern Australia are 35% to 50% higher than to those estimated for the Agulhas Bank region. Similar to the Agulhas Bank, the values of **P** in the southern Australia reach a peak during winter, but differ in that this winter peak is prolonged from July to September (Hemer et al 2010), while on the

Agulhas Bank the peak only occurs in July. The winter values of **P** in the southern Australia reaches 50 kW/m which is similar to the Agulhas Bank (at 35° S). Cape du Couedic (36° S) and Cape Naturaliste (33° S) which are at similar latitudes to the Agulhas Bank (Cape Agulhas at 34.5° S) are the most energetic regions on the south coast of Australia.

The similarity of values **of P** between the Agulhas Bank and the south coast of Australia are mostly related to geographical location. At both regions, most of the waves are generated in the circumpolar trough and by intense extra-tropical cyclones over the Southern Ocean around 60° S. At both regions, part of the wave field is generated by local fronts which propagate from the west to east with periods varying from 6 to 8 days (Rossouw et all 1992, Simmonds and Keay 2000). The seasonal shift of the South-Polar wind Belt from 45° S in summer to 35° S in winter (Hurrell et al 1998) drives the seasonal variability of these wave climates, bringing higher waves closer to the shore during winter with calmer seas during summer.

The differences of values of **P** between the Agulhas Bank and south coast of Australia may be related to the influence of tropical cyclones over the eastern tropical Indian Ocean. These increase values of **Hm0** on the Australian wave field. Also of importance is that factor is that the southern Australia is influenced to greater degree by stronger westerly surface winds compared to the Agulhas Bank.

5.2 Suitable location for the PSS

This study set three criteria to better rank the wave fields by sub-regions on the Agulhas Bank: (1) magnitude of the available **P**, (2) variability of the available resource and (3) local shelf width. For the first criteria, the values of **P** are higher in the west region of the Agulhas Bank near Cape Agulhas and decrease eastwards. The second criterion suggests that there is no significant difference between the interannual variability of **P** within the entire Agullhas Bank domain. There are, however, significant differences in diurnal variability between the western and eastern regions of the Agulhas Bank. The **P** has higher values during winter and transitional seasons and lower values during summer. The lowest values are on average not lower than 20 kW/m, at ~ 80 m water depth. The third criterion (continental shelf width) is an important parameter for the technical and economical point of view of implementation of wave energy converter systems. As previously mentioned noted, the Agulhas Bank is narrower on the extremities compared to the centre and are mainly close to deep water. However, due to the predominant southwest waves, higher and more energetic waves occur mainly at Cape Agulhas where the deep water waves reach the coast with less attenuation. The same southwest waves lose energy travelling for longer times over the bank to reach Cape Recife. This wave energy loss may be due to bottom friction, destructive interference with surface currents and surface winds (hence the **Hm0** is higher at Cape Agulhas compared to Cape Recife). Another effect of shelf width is on the **Tm0** which is relatively higher on the centre of the bank where the effect of the Agulhas Current is minor.

Despite these differences and given the sub regional wave field characteristics, this study suggest that the entire Agulhas Bank is suitable for installing wave energy converter devices. However, given the local higher values of **P**, the diurnal cycle and the narrow shelf, Cape Agulhas on the west region, is the most viable location to implement wave energy converter systems, followed by Mossel Bay, and Cape Recife. Due to the existence of a sensitive marine reserve, Tsitsikamma cannot be used.

5.3 Suitable technology for the PSS

Wave energy converters (WEC) are meant to convert the kinetic and potential energy transported by ocean waves into useful work. In general the **P** in a specific coastal region may vary with the local depth. Apart from design types (attenuators, point absorbers, oscillating wave surge converter, oscillating water column, overtopping device, submerged pressure differential and others, see section 2.8) wave energy converters are basically classified by the location to the coastline (shoreline, nearshore or offshore).

Shoreline wave energy converters have the advantage of being close to the main electric grid (meaning less power loss through transport), they are easier to maintain and they are protected from extreme wave conditions. However, the disadvantage is the reduced power capacity per unit due to lower **P** availability in very shallow water. Depending on the local geomorphology, the shoreline WECs are very site specific and most of the time requires modifications of the natural environment and the geometry of the site, implying that it cannot be designed for mass production (Boyle 2004, Drew et al 2009, and Rodrigues 2012).

Nearshore devices are mounted in intermediate waters where the local depth is less than ¼ of the incident wavelength (Drew et al 2009). For the Agulhas Bank wave field, this is between 10 and 80 m water depth. These devices have the advantage of allowing both fixed structure or floating moorings and can be close enough to the shore to make them easier to install and maintain. The disadvantage is the relatively reduced available **P**, limiting the harvesting potential (Drew et al 2009, Rodrigues 2012).

Offshore WECs are those designed for deep water where the local depth is greater than 1/3 of the wavelength (Drew et al 2009). These have the great advantage of harvesting greater power due to the large wave energy available in deep water waves (Thorpe 1999, Boyle 2004, and Drew et al 2009. To date, the most successful shoreline WECs are the oscillating water column (OWC). However, despite the great challenges in installation maintenance and initial investment, nearshore and offshore devices are the most implemented WECs (Thorpe 1999, World Energy Council 2007).

This study suggests that for the PSS, a mixture of different technologies can deliver better results. A single or an array of wave energy converters which convert directly wave energy into electricity would be used to produce electricity to supply an electric pump which will pump sea water to the PSS. In the

same PPS system, another array of wave energy converters would directly convert wave energy into mechanical energy to pump sea water to the PSS. Additionally, a wind farm would be placed in the same system to work in the same scheme as the WECs.

5.4 Weaknesses and limitations

Similar to the several scientific studies, this study also has a few limitations concerning on the data and methods. The first limitation concerns the spatial resolution of the WAVEWATCH III / IFREMER dataset, which is 0.5°x0.5°, which is too low to resolve the details of coastal wave processes such as reflection, diffraction and attenuation into small capes and bays.

The second limitation concerns the short sampling time of the insitu ADCP data, which means that only 90 days (correspond to the autumn of 2011) were used to directly assess the wave fields at the four selected mooring sites. This limited the extraction of more precise diurnal cycle. However, the long-time series 8 hourly NCEP data enabled the extraction and investigation of the diurnal cycle.

The third limitation was the over/under estimation of the naturally available **P** resource at various depth. Calculations done using the low resolution of the WAVEWATCH III dataset forced the values of **P** to be averaged with depth. A much better method to assess the local **P** potential would be to sub-divide the wave field into a smaller grid with a maximum resolution possible and then to estimate the **P** available in each cell. These results can then be integrated throughout the entire domain to obtain the total naturally wave power resource. This methodology may produce slightly different results ranging from 3 to 5 kW/m shoreline and nearshore, but not significantly different results offshore because here the offshore wave field tend to be uniform for wide areas and independent of bottom friction. Notwithstanding, the results obtained in the present study are still reliable and consistent with others studies such as Joubert (2008) who used the SWAN model, with a relative small grid, MacHutchon (2006) who used insitu buoy dataset, and the Wave Energy Council. Moreover, the results obtained using the NCEP dataset are consistent with the results obtained using ADCP dataset. Differences between results from ADCP and WAVEWATCH III data may occur because the ADCP data corresponds to the bathymetric contour of 80 m (34.5° S) water depth while the WAVEWATCH III data corresponds to water depth near 128 m (~ 35.5° S). The choice of different bathymetric contours was an attempt to cover both nearshore and offshore environments. It was realised that there is little difference ($\Delta \approx 6\%$ to 11%) between the values of the wave parameters measured at the 80 and near 128 m bathymetric contours.

Although the WAVEWATCH III dataset has ½° resolution, it still considered reliable for operational purposes. This dataset is one of the most widely used for regional and global wave forecasting purposes. When integrating it into nearshore wave models such as SWAN or WAM, it can provide a higher level of confidence for nearshore and shoreline wave processes. Many other wave models such

as the MOHID, *MIKE 21*, and WaMoS II are used for operational purposes and most of these models use the same input data as the WAVEWATCH III but other are purely radar based models.

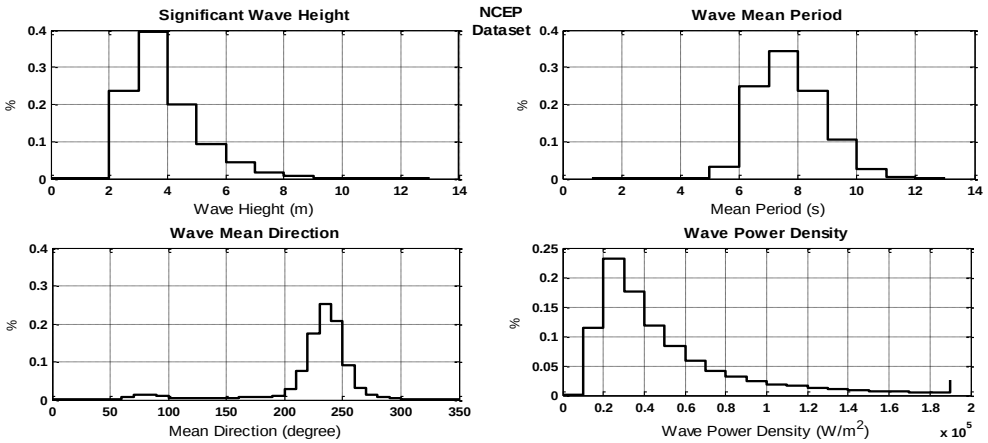

Figure 5- 1. Cumulative analysis of the nearshore wave field parameters across the Agulhas Bank.

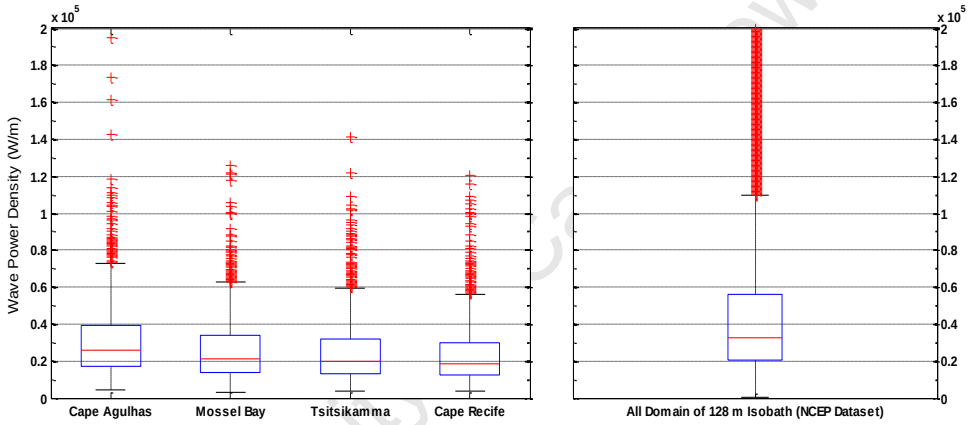

Figure 5- 2. The 25 and 75 percentile comparison between wave power density values estimated from the ADCP and NCEP datasets.

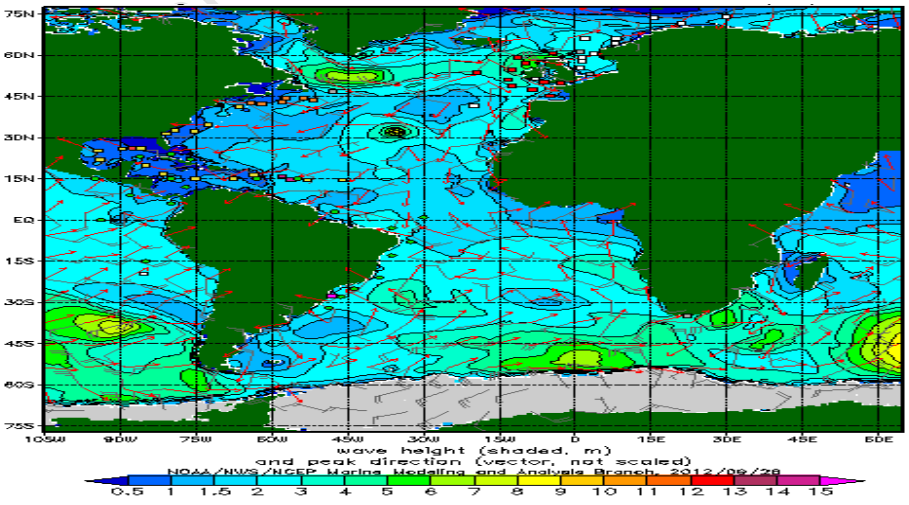

Figure 5- 3. Dominant regions of wave generation. WAVEWATCH III (NCEP).

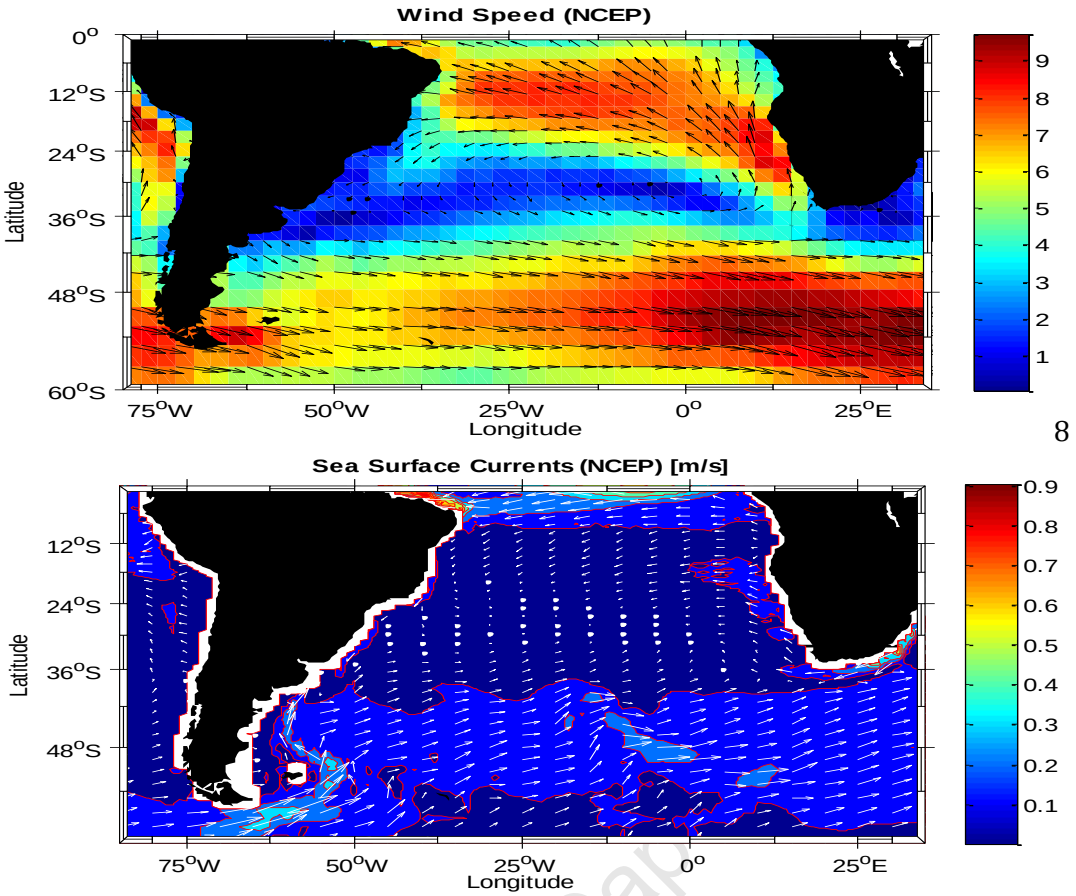

Figure 5- 4. Dominant wind and surface currents patterns over Sothern Atlantic Ocean.

Chapter 6

Conclusions

The present study investigated the characteristics of the wave field on the Agulhas Bank to assess if the naturally available and technically recoverable wave power density is sufficient for a pumped storage scheme (PSS). This study investigated the wave field characteristics, taking into account the spatial and temporal variability, and also estimated the wave power necessary for the PSS. To address these issues, this study used insitu ADCP wave data which were collected at four selected mooring sites (Cape Agulhas, Mossel Bay, Tsitsikamma, and Cape Recife), and also used a 16 years 0.5x0.5° resolution WAVEWATCH III wave data. The main wave parameters analyzed were the significant wave height (**Hm0**), mean period (**Tm0**), mean direction (**Mdir**) and wave power density (**P**). The **P** resource was estimated by calculating the wave energy flux across a unit diameter circle of wave field.

This section presents the conclusions of this study according to the main addressed questions of the Chapter 1 section 3 (1.3).

Wave field characteristics

From the results and analysis produced using the ADCP data, this study concludes that the values of **Hm0** are greatest at Cape Agulhas followed by Mossel Bay, Tsitsikamma and Cape Recife. The values of **Tm0** are higher on the middle of the bank near Mossel Bay and Tsitsikamma and relatively lower at either extremity of the bank (Cape Agulhas and Cape Recife). The incident waves are predominantly from the southwest. Comparing the four selected mooring sites, Cape Agulhas had most available **P** (75% for 40 kW/m, 25% for 17 kW/m with, an average of 31 kW/m) followed by Mossel Bay (75% for 34 kW/m, 25% for 14 kW/m, with an average of 25.2 kW/m), Tsitsikamma (75% for 32 kW/m, 25% for 13 kW/m, with an average of 25.0 kW/m), and Cape Recife (75% for 30 kW/m, 25% for 12 kW/m, with an average of 23.7 kW/m).

From the long time series NCEP data, this study was able to conclude that from the nearshore to 128 m water depth, the most frequent waves have 3.0 m of **Hm0**, 7.0 s of **Tm0** and the dominant wave direction is from the southwest. The highest frequency of occurrence corresponds to waves with values of **P** equivalent to 30 kW/m followed by 40 kW/m, 50 kW/m and 20 kW/m.

Temporal and spatial variability

This study concludes that the diurnal cycle of the **P** is similar to the diurnal cycle of the **Hm0**. From the long time series WAVEWATCH III data, this study indicates that nearshore **P** and **Hm0** has higher values in the evening and lower values in the morning, and offshore, **P** and **Hm0** values are higher in

the afternoon and lower at night. However, the nearshore **Tm0** values are higher in the morning and lower in the evening, and offshore values of **Tm0** are higher at night and lower in the evening.

This study also concluded that there are seasonal and interannual variability within the Agulhas Bank wave field. The lowest values of **Hm0**, **Tm0** and **P** occurs during summer, (December is the trough) and the highest values occur during winter, (July is the peak). The period of time per annual cycle in which values of **P** are above the annual mean is ~ equal to the period of time in which values of **P** are below the annual mean, however, the lowest summer values are in average not lower than 20 kW/m.

With respect to the spatial variability, this study also concludes that during summer the values of **P** are lower (~ 20 to 30 kW/m)on the entire area of the Agulhas Bank. In autumn, waves with 35 to 40 kW/m reach the mid shelf along the 37° S, and during winter the entire area of the Agulhas Bank is covered by high energetic waves (40 kW/m at very nearshore and 50 kW/m form 35.5° S towards offshore). In spring, the higher energetic waves begin to retreat towards offshore leaving most area the bank with values of **P** of 30 kW/m.

Long term wave field variability in relation to global climate variables and parameters

After investigating the **P** time series of the Agulhas Bank, this study concludes that there is a strong correlation between this variable and mean **SLP** monthly mean zonal and meridional wind and sea surface currents, and monthly mean **SST**. This study also concludes that the interannual variability of the wave field on the Agulhas Bank may be influenced by **NINO3** (higher values of **P** are correlated to **La Niña** years and lower values of **P** are correlated to **El Niño** years), by **SOI**, and by **SAM** which all showed significant values of correlation and regression.

Total available wave energy resource

This study estimates that the total annual wave energy resource near 128 m water depth is ~ 380 TWh/yr. The southwest and southeast regions of the bank has the most (138 TWh) and least (121 TWh) available wave energy resource respectively, and the central region has ~ 124 TWh. It is also concludes that the winter season (133 TWh) has the most naturally available wave energy resource, and the summer season has the least (67 TWh). The total annual recoverable wave energy is in average ~ 700 TWh (10.0 to 80 MW/km).

Concerning the pumped storage scheme, this study concludes that for a small flow rate (1 m^3s^{-1}), the necessary power supply to pump sea water 100, 250 and 350 m up into the upper reservoir with a 80% or 85% of efficiency will be ~ 0.85, 2.0 and 2.9 MW respectively, for a decent flow rate (50 m^3s^{-1}), the values of power necessary to pump sea water 100, 250 and 350 m up into the upper reservoir with a 80% or 85% of efficiency will be ~ 43, 107 and 150 MW respectively, and for a relatively large flow rate (100 m^3s^{-1}), the necessary power needed to pump sea water 100, 250 and 350 m up with a 80%

or 85% of efficiency will be ~ 85, 210 and 299 MW respectively. This study also concludes the time necessary to pump sea water to the upper reservoir with a small flow rate will be ~ 63h to 175h for volumes of 5 to 15 million m^3, 28 to 82 pumping hours using moderate flow rate it would, and 13 to 27 pumping hours using a large flow rate.

Finally, this study concludes that the entire Agulhas Bank has sufficient wave energy resource to supply a PSS. Given the great technological advancements in the field of wave energy converting systems, it is therefore feasible to install arrays of wave energy converting devices along bathymetric contours > 10 m water depth.

Bibliography

ACORE. Ocean Power Technologies (2012): Capturing Wave Energy for the U.S. Navy and the Grid. *Available at: http://www.acore.org/wp-content/uploads/2012/01/Ocean-Power-Technologies-Case-Study.pdf.*

Alvarez, A. F. and Kofoed, J. P. (2010). Estimation Of Available Wave Power in the Near Shore Area Around Hanstholm Harbor. *Civil Engineer Department Aalborg University*.

Arblaster, J. M., Meehl. G. A. (2005). Contributions of External Forcings to Southern Annular Mode Trends. *Journal of Climate Volume 19*.

AWS Ocean Energy Ltd. (2012): Technology. Practical, affordable wave energy. *Available at http://www.awsocean.com/technology.aspx.*

ASX Announcement (2012). CSIRO wave energy report confirms huge potential. Carnegie Wave Energy Limited. *Available at: http://www.carnegiewave.com/index.php?url=/projects/perthproject.*

Babarit. A. (2010). Impact of long separating distances on the energy production of two interacting wave converters. *Ocean Engineering*. 37:718 729.

Barstow. S. (2010). WorldWaves: Integrated Model, Satellite and In-Situ Measurements Providing Quality Wave and Wind Data Anywhere, anytime. *Fugro OCEANOR*. Norway.

Bauer. E. (2001). Interannual Changes of the Ocean Wave Variability in the North Atlantic and in the North Sea. *Climate Research Clim Res*. Vol. 18: 63–69, 2001.

BBC News (2007). Orkney to Get Biggest Wave Farm. A*vailable at http://news.bbc.co.uk/1/hi/Scotland /6377423.stm*.

Behrens, S., Hayward. J., Woodman, S., Hemer, M. And Ayre, M. (2012). AEMO 100% Renewable Energy study: Wave Energy. Australia: CSIRO.

BERR. (2008). Atlas of UK Marine Renewable Energy Resources: A strategic Environmental Assessment Report.

Beels. C., Trocha. P., Kofoed. J. P., Frigaard. P., Kringelum. J. V., Kromann. P. C., Donovanc. M. H., Roucka. J., De Backera. G.)2011). A methodology for production and cost assessment of a farm of wave energy converters. *Renewable Energy*. Volume 36, 3402–3416.

Boyd, A. J., and F. A. Shillington. (1994). Physical forcing and circulation patterns on the Agulhas Bank. S. Afr. Jounranl of Science, (90). 114-122.

Boyle. G. (2004). Renewable Energy. Power for a Sustainable Future. Second Edition: Oxford University Press.

Birkett. A. (2010). Relationship between Atmospheric Variability and Variability in the Wave Records at Cape Point. MSs. thesis. University of Cape Town.

Baschek. B. (1999). Wave-Current Interaction in Tidal Fronts. USA: Woods Hole Oceanographic Institution.

Cameron. L., Doherty. R., A. Henry., Bourdier, T. Whittaker. (2010). Design of the Next Generation of the Oyster Wave Energy. 3rd International Conference on Ocean Energy, 6 October, Bilbao 2010.

Carbon Trust. (2011). Accelerating Marine Energy. The potential for cost reduction – insights from the Carbon Trust Marine Energy Accelerator.

Carnergie Wave Energy. (2009): CETO West Perth Western Australia: *Available at: http://carnegiecorp.com.au/index.php?url=/ceto/what-is-ceto*.

Carnegie Wave Energy Limited. (2012). Renewable Power from the Ocean's Waves. CETO Wave Power. *Available at: http://www.carnegiewave.com/index.php?url=/ceto/ceto-overview.*

Carter, R. and M. H. Schleyer. (1988). Plankton Distribution in Natal coastal Waters. In Coastal Ocean Studies off Natal, South Africa, E. Lecture Notes on Coastal and Estuarine Studies 26, Springer-Verlag, Berlin, 152-177.

Cayan, D. (1992): Latent and sensible heat flux anomalies over the northern oceans: Driving the sea surface temperature. *Journal of Physical Oceanography*, (22), 859–881.

Centre for Renewable Energy Sources (CRES). (2002): European Thematic Network on Wave Energy. Wave energy Utilization in Europe. Current Status and Perspectives, ISB 960-86907-1-4.

Clément. A., McCullen. P., Falcão. A., Fiorentino. A., Gardner. F., Hammarlund. K., Lemonisa. G., Lewis. T., Nielsen. K., Petroncini. S., Pontes. M. T., Sjöström. B. O., Sørensen. H. C., Thorpe. T. (2002). Wave energy in Europe: Current Status and Perspectives. *Renewable and Sustainable Energy Reviews*, Volume 6, (5), 405–431.

Continental. (2008). AquaBuOY Converts Waves into Energy. *Available at http://www.contionline.com/generator/www/com/en/continental/pressportal/themes/press_releases/1_topics/conticompact/ms_2008_11_03_en.html (Accessed 25 jun. 12).*

Cook, K. H. (2000). The South Indian Convergence Zone and Interannual Rainfall Variability over Southern Africa, Journal of Climate, (13), 3789– 3804.

Cook, K. H. (2001), A Southern Hemisphere Wave Response to ENSO with Implications for Southern Africa rainfall, Journal of Atmospheric Sciences, 58(15), 2146–2162.

Cook. C, Reason C. J, and B. C. Hewitson. (2004). Wet and Dry Spells within Particular Wet and Dry Summers in the South African Summer Rainfall Region. *Climate Research*, (26), 17–31.

Cooper. A. L. (1986). Interaction between Ocean Surface Waves and Currents. N.R.L. Memorandum report. Naval Washington. D.C : Research Laboratory.5755, 1-18.

Costa. J. S., Sarmento. A., Gardner. F, Beirão. P., Brito-Melo. A. (2005). Time Domain Model of the AWS Wave Energy Converter. 6th European Wave and Tidal Energy Conference Glasgow, UK.

Cruz. J. M. B. P., Sarmento. A. J. N. A. (2004). Energia das Ondas Introdução aos Aspectos Tecnológicos, Económicos e Ambientais. Instituto do Ambiente Alfragide. WEC – Wave Energy Centre, ISBN: 972-8577-11-7.

Currie. R., Elrick. B., Loannidi. M., Nicolson. C. (2002). Wave Power: The University of Strathclyde in Glasgow. *Available at: http://www.esru.strath.ac.uk/EandE/Web_sites/01-02/RE_info/wave%20power.htm.*

Cushman. B. R., Beckers. J. M. (2011). Introduction to Geophysical Fluid Dynamics – Physical and Numerical Aspects. Second Edition. Elservier. Academic Press.

Department of Environmental Affairs. (2012). Report 1. ADCP Kinetics versus Measurement Integrity on a tethered buoy deployment. South Africa.

Department of Minerals and Energy. (2004a). Economic and financial calculations and modelling for the renewable energy strategy formulation. Pretoria: Prepared for DME by Conningarth Economists for CaBEERE project.

Department of Minerals and Energy. (2004b). White paper on renewable energy policy of the Republic of South Africa. Government Gazette.

Dodet. G., Bertin. X., and Tadora. R. (2011). Wave Climate Variation in the North-East Atlantic Ocean over the Last Six Decades. C. Little. Portugal.

Drew. B., Plummer. A., R, and Sahinkaya. M. N., (2009). A Review of Wave Energy Converter Technology. DOI: 10.1243/09576509JPE782.

Earle. M. D., Bishop. J. M. (1984). A Practical Guide to Ocean Waves Measurement and Analysis. ENDECO, INC. Marion.

El-Zaza. S. Z., and Elzebda. J. M. (2009). Development of Wave Energy Conversion Device - Gaza Shoreline. A MSc. Thesis, 1430, The Islamic University of Gaza.

EPRI (2011): Overview, supra note 4, at 16; Ocean Wave Power. Available at: http://www.wcl.american.edu/org/sustainabledevelopment/2007/07spring.pdf.

EMEC. (2009). "EMEC: European Marine Energy Centre.". *Available at: http://www.emec.org.uk/.*

Esper. O., Versteegh. G. J. M,. Zonneveld. K. A. F., Willems. H. (2003). A Palynological Reconstruction of the Agulhas Retroflection (South Atlantic Ocean) during the Late Quaternary. *Global and Planetary Change*, 41 (2004) 31–62.

Flemming. M. K., and Akkers. W. (1986). Agulhas Bank Studies. Marine geology off the Tsitsikamma Coast. *Poster paper*, Agulhas Bank Symposium, Cape Town.

Folley. M., and Whittaker. T. J. T. (2009). Analysis of the nearshore wave energy resource. *Renewable Energy* 34(7), 1709-1715.

Folley. M., Elsaesser. B., and Whittaker. T. (2010). Analysis of the wave energy resource at the European Marine Energy Centre. SPACE, RPS Group Plc.

Generation Communication – GI 003. (2010). Pumped Storage Schemes: Drakensberg and Palmiet. *Available at: http://www.eskom.co.za/content/Pumped%20Storage%20Schemes%20-%20Palmiet%20&%20Pumped%20Storage.pdf.*

Gill. A. E., and E. H. Schumann. (1979). Topographically Induced Changes in the Structure of an Inertial Coastal Jet: Application to the Agulhas Current. *Journal of Physical Oceanography.* (9), 975-991.

Gill. A. E. 1977. Coastally Trapped Waves in the Atmosphere. Quart.Journal of Roy. *Meteorology. Soc*., (103), 431-440.

Gillett. N. P., Kell. T. D., and Jones. P. D. (2006). Regional climate impacts of the Southern Annular Mode. *Geophysical Research Letters*, VOL. 33, L23704, doi:10.1029/2006GL027721.

Gulev. S. K., And H. L. (1999). Changes of Wind Waves in the North Atlantic over the Last 30 Years. *Int. J. Climatol*. (19), 1091–1117.

Guzman. H. A. R. (2010). Value of Pumped-Storage Hydro for Wind Power Integration in the British Columbia Hydroelectric System. MSc thesis, University of British Columbia.

Hammar. L., and Ehnberg. J. (2010). A screening of Ocean Energy Resource in the Western Indian Ocean. CHALMERS UNIVERSITY OF TECHNOLOGY Göteborg. Report No. DRAFT ISSN No. 1404-8167.

Hanley. K., Stephen. E., Belcher. E., Sullivan. P. Peter. (2010). A Global Climatology of Wind–Wave Interaction. *American Meteorological Society*. DOI: 10.1175/2010JPO4377.1.

Hancke, Lisa, "Dynamics of the Tsitsikamma current, with implications for larval transport of chokka squid (Loligo reynaudii) on the eastern Agulhas Bank" (2010). CPUT Theses & Dissertations. Paper 328. http://dk.cput.ac.za/td_cput/328.

Hemer. M. A. and D. A. Griffin. (2010). The Wave Energy Resource along Australia's Southern Margin. *Journal Of Renewable and Sustainable Energy,* (2), 043108 2010.

Hemer. M. A., K. McInnes. J. A., J. R. Hunter. (2008). Variability and trends in the Australian wave climate and consequent coastal vulnerability. CSIRO. Australia. *Available at: http://www.climatechange.gov.au/publications/coastline/wave-climate.aspx.*

Holm. D., Banks. D, Schäffler. J., Worthington. R., and Afrane-Okese. Y. (2008). Potential of Renewable Energy to Contribute to National Electricity Emergency Response and Sustainable Development Renewable Energy *Briefing Paper*.Version 8.

Holms. P., Meadows. M. (2012). Southern Africa Geomorphology. Recent Trends and New Directions. SUN MeDIA Bloemfontein. SUN Press.

Hurrell. J.W. and H. Van Loon. (1994). A Modulation of the Atmospheric Annual Cycle in the Southern Hemisphere. *Tellus*, (46A), 325-338.

IM-29-02-2004, (2004): Caracterizacao Climatica da Costa. IM. Capitulo 2. Portugal. *Available at: http://mudancasclimaticas.cptec.inpe.br/~rmclima/pdfs/prod_probio/Sumario.pdf.*

Joubert. J. R., Bosman. D. E. (2008). An Investigation of the Wave Energy Resource on the South African Coast, Focusing on the Spatial Distribution of the South West Coast. Msc thesis, University of Stellenbosch.

Johnson. S. (2007). Wave Energy: New-Wave Interest in an Old Alternative Resource. Sustainable Development Law & Policy. Spring 2007, 21, 72-73.

Jacobson. J. (2011): Mapping Assessment of the United States Ocean Wave Energy Resource. Final Report. 1024637. EPRI. USA.

Kenyon. K. E. (1996). Shallow Water Gravity Waves: A Note on the Particle Orbits. *Journal of Oceanography* Vol. (52), 353 to 357.

Kidson. J. W. (1988). Interannual Variations in the Southern Hemisphere Circulation. *J. Climate*,(1), 1177–1198.

Kundu. P. K., Cohen. I. M. (2008). Fluid Mechanics. Elservier. Academic Press. USA.

Lewis, A., Estefen. S., J. Huckerby., Musial. W., Pontes. T., Torres-Martinez. J. (2011): Ocean Energy. In IPCC Special Report on Renewable Energy Sources and Climate Change Mitigation [O. Edenhofer, R. Pichs-Madruga, Y. Sokona, K. Seyboth, P. Matschoss, S. Kadner, T. Zwickel, P. Eickemeier, G. Hansen, S. Schlömer, C. von Stechow

(eds)], Cambridge University Press, Cambridge, United Kingdom and New York, NY, USA.

Lutjeharms. J. R. E. (2006). The Coastal Oceans of South-Eastern Africa. *In The Sea,* Volume 14B, Harvard University Press, Cambridge, MA, 783-834.

MacHutchon. K. R., and Bosman.D. E. (2010). The Characteristics of the South African Sea Storms. MSc thesis, University of Stellenbosch.

MATLAB R2011b. (2012): Partial Differential Equation Toolbox™ User's Guide. MathWorks. *Available at: www.mathworks.com.*

Meisen. P., Loiseau. A. (2009). Ocean Energy Technologies for Renewable Energy Generation. Global Energy Network. *Available at: www.geni.org.*

Nakicenovic. N., Grubler. A., and McDonald. A. (1998). Global Energy Perspectives. Cambridge: Cambridge University Press.

National Electricity Regulator. (2004a): National Integrated Resource Plan, 2003/4: Reference case. Energy Research Institute, University of Cape Town.

National Electricity Regulator-NER. (2004b): National Integrated Resource Plan, 2003/4: Stage two: Risk and Sensitivity Analysis. Energy Research Institute, University of Cape Town.

National Electricity Regulator-NER. (2001a): Electricity supply statistics for South Africa 2001. Pretoria,NER. *Available at: www.ner.org.za/publs.htm.*

National Electricity Regulator-NER. (2001b): Lighting up South Africa 2001. Pretoria, NER. *Available at: www.ner.org.za/publs.htm.*

National Electricity Regulator-NER. (2002a): Electricity supply statistics for South Africa 2002. Pretoria, NER. *Available at: www.ner.org.za/publs.htm.*

Nicholson. S. O., and Flohn. H. (1980). African Environmental and Climatic Changes and the General Atmospheric Circulation in Late Pleistocene and Holocene. *Climate Change* (2), 313-348.

Nortek (2005): AWAC - Acoustic Wave and Current Meter. User Guide September. NOTERK AS 2004 -2005. *Available at: http://imos-toolbox.googlecode.com/svn-history/r1177/wiki/documents/Instruments/Nortek/awac.pdf*

Nusca. A. (2012): "Aquamarine Power's Oyster 2: Can It Help Wave Energy Go Commercial?" Smart Planet. *Available at:. http://www.smartplanet.com/blog/smart-takes/aquamarine-powers-oyster-2-can-it-help-wave-energy-go-commercial/7376.*

Orchison. K. (2010): "Wave of the Future Needs Investment". The Australian. *Available at: http://www.theaustralian.com.au/special-reports/climate-change/climate-change/story-fn5oikwf-1225935586957.*

Palha. A., Mendes. L., Fortes. C. J., Brito-Melo. A., Sarmento. A. (2010). The Impact of Wave Energy Farms in the Shoreline Wave Climate: Portuguese Pilot zone case study using Pelamis energy wave devices. *Renewable Energy* (35), 62–77.

Phillips. O. M. (1962). Recent Developments in the Theory of Wave Generation by Wind. *Journal of Geophysical*

Research. Vol 67, No.8, 3135–3141.

Pound. S and Pickard. G. L. (1983). Introductory Dynamical Oceanography – 2nd Edition. PEGRAMON Press. Canada.

Reason. C. J. C., Landman. W., and Tennant. W. (2006). Seasonal to Decadal Prediction of Southern African Climate and Its Links with Variability of th Atlantic Ocean. *American Meteorological Society*. DOI:10.1175/BAMS-87-7-941.

Reason. C.J.C., J.R.E. Lutjeharms., J. Hermes., A. Biastoch., R.E. Roman. (2003). Inter-Ocean Fluxes South of Africa in an Eddy-Permitting Model. *Deep-Sea Research II* (50) 281–298.

Retief. D. (2007). Ocean Energy in South Africa. Center for Renewable and Sustainable Energy Studies. Wave Power Seminar. 8th June 20007.

Rodrigues. L. (2012). Wave power conversion systems for electrical energy production, Nova University of Lisbon.

Rossouw. J., Coetzee. L. W., and Visser. C. J. (1982). A South African Wave Climate Study. Proceedings of 18th Conference on Coastal Engineering. ICCE No 18.

Rossouw. J., Retief. G., Coetsee. A. (1989). Design Waves for the South African Coastline. PhD thesis, University Of Stellenbosch.

Russell. R.C.H et al. (1954). Waves and Tides. Hutchinson's. London.

SANERI. (2012). Renewable Energy Database and the South African Wind Atlas. Colloquium on Energy Planning Dept of Energy 29-30 March 2012 Gallagher Convention Centre.

Sigauke. C., and Chikobvuy. D. (2010). Daily peak electricity load forecasting in South Africa using a multivariate non-parametric regression approach. *NR* Volume 26 (2), 97-111.

Silvester. R., and Mitchell. H. L. (1997). Ocean Waves around the Coastlines of Australia. 6th Australian Hydraulics and Fluid Mechanics Conference. Adelaide, Australia, 5-9 December 1997.

Sorensen. B. (2004). Renewable Energy. Third Edition. Elsevier Academic Press.

Stewart. R. H., and Vesecky. J. (1982). The Observation of Ocean Surface Phenomena Using Imagery from the SEASAT Synthetic Aperture Radar: An Assessment. *Journal of Geophysical Research*, Vol. 87, (5), 3397-3430.

Stewart. R. H. (2005). Introduction to Physical Oceanography. Department of Oceanography. Texas A&M University. *Available at: http://oceanworld.tamu.edu/resources/oceanography-book/contents.htm.*

Stull. R. B. (2000). Meteorology for Scientists and Engineers. Brooks / Code Thompson Learning.

Swart, V. P and J. L. Largier. (1987). Thermal structure of Agulhas Bank water. *S. Afr. J. Mar. Sci*., (5), 243-253.

Whittaker. T.J.T., Collier. D., Folley. M., Osterreid. M., Henry. A., Crowley. M. (2007): 'The Development of Oyster – A Shallow Water Surging Wave Energy Converter', 7th European Wave & Tidal Energy Conference, Portugal.

Timera Eenrgy ©2012. UK. *Available at: http://www.timera-energy.com/energy-markets/fuel-for-thought-jan-27th/*

Tolman. H. L., Alves. J. H. G. M., Chao. Y. Y. (2004). Operational Forecasting of Wind Generated Waves by

Hurricane Isabel at NCEP. *Weather and Forecasting*. In press, 2004.

Tolman. H. L. (2009): User Manual and System Documentation of WAVEWATHC III (TM) Version 3.14. Environmental Modeling Center. NOAA.

Theron. A., Rossouw. M., Barwell. L., Maherry. A., Diedericks. G., Wet. P. (2010). Quantification of Risks to Coastal Areas and Development: Wave Run-up and Erosion. Science Real and relevant conference 2010. CSIR. Reference: NE20-PA-F.

Thomas. A. M, and Welch. K. W. (2006): SEADOG Pump Technology Wave Energy Converter. Proceedings of the Sixteenth (2006) International Offshore and Polar Engineering Conference. ISBN 1-880653-66-4 (Set); ISSN 1098-6189 (Set).

Thorpe. T W. (1999): A Brief Review of Wave Energy, A Report Produced for The UK Department of Trade and Industry. ETSU-R120. *Available at: http://www.mech.ed.ac.uk/research/wavepower/Tom%20Thorpe/Tom%20Thorpe%20report.pdf*

Thorpe. T W. (1999). An Overview of Wave Energy Technologies: Status, Performance and Costs. Wave Power: Moving towards Commercial Viability, London. *Available at: http://waveberg.com/pdfs/overview.pdf.*

Tyson P. D and Preston. W RA. (2000). The Weather and Climate of Southern Africa. Oxford Press.

Visbeck. M. (2008). A Station-Based Southern Annular Mode Index from 1884 to 2005. *Journal Of Climate* Vo 22. DOI: 10.1175/2008jcli2260.1.

VOITH. (2012). Wave power at Voith Hydro Wavegen. UK. *Available at: www.wavegen.com.*

Walck. C. (2007): Hand-book on Statistical Distributions for experimentalists. Internal Report SUF–PFY/96–01. University of Stockholm.

Wallace. J. M., and D. S. Gutzler. (1981). Teleconnections in the Geopotential Height Field during the Northern Hemisphere winter. Mon. *Wea. Rev*., (109), 784–812.

Walker. N. D. (1986). Satellite Observations of the Agulhas Current and Episodic Upwelling South of Africa. *Deep-Sea Res*., (33), 1083-1106.

White. W. B., and R. G. Peterson. (1996). An Antarctic Circumpolar Wave in Surface Pressure, Wind, Temperature and Sea-Ice Extent. *Nature,* 380, 699–702.

Wikipedia. (2012). Wave Dragon. Wikimedia Foundation. *Available at: http://en.wikipedia.org/wiki/Wave_Dragon.*

Wild. K., Crawford. C., Djilali. N. (2009). Coupled Operation of a Wind Farm and Pumped Storage Facility: Techno-Economic Modelling and Stochastic Optimization. Msc thesis, University of Victoria.

Winkler. H. (2007): Long Term Mitigation Scenarios: Technical Report. Pretoria: Department of Environment Affairs and Tourism, October 2007. *Available at: http://www.erc.uct.ac.za/Research/publications/07-Winkler-LTMS-Technical%20Report.pdf.*

Winkler. H., D. Davidson., Kenny. A, Prasad. G., Nkomo. J., Sparks. D., Howells. M., Alfstad. T. (2006). Energy Policies for Sustainable Development in South Africa. Energy Research Centre. University of Cape Town. ISBN: 0-620-36294-4.

Wolf. J., and Prandle. D. (1999). Some Observations of Wave–Current Interaction. *Coastal Engineering* (37), 471–485.

World Energy Council. (2003): South African Energy Profile. WEC and South African National Energy Association, Johannesburg. *Available at: http://www.sanea.org.za/*

World Energy Council. (2004): Survey of World Energy Resources 407 (2004). *Available at: http://www. worldenergy.org/wec-geis/global/downloads/ser04/SER_Wave_04.pdf.*

World Energy Council. (2010): 2010 Survey of Energy Resources. ISBN: 978 0 946121 021. *Available at: http://www. worldenergy.org/wec-geis/global/downloads/ser04/SER_Wave_10.pdf.*

World Meteorological Organization. (1998.): Guide to Wave Analysis and Forecasting. WMO-No. 702. *Available at: https://www.wmo.int/pages/prog/amp/mmop/documents/WMO%20No%20702/WMO702.pdf.*

Zabihian. F., and Fung. A. S. (2011). Review of marine renewable energies: Case study of Iran. *Renewable and Sustainable Energy Reviews*. (15), 2461–2474.

APPENDIX A

Auxiliary Tables

Table 3- 1. Technical specification of the wave measuring device, ADCP Nortek AWAC

Manufacturer	Nortek AS
Model	AWAK N6160 – 600kHz
Sensors	Temperature, Compass, Tilt, Pressure,
Software	AWAK/AWAC AST
Data Recording	Memory in bytes: 9xNo. Of samples + 46
System	Acoustic Frequency: 600 KHz; Acoustic beams: three slanted at 25°;
Operating mode	Stand alone or long term monitoring
Maximum Depth	40 m
Data types	Pressure and velocity cell along each beam, Acoustic Surface Tracking – AST
Depth cell size	0. 4 to 2.0 m
Maximum sampling rate	2Hz, AST 4Hz
Number of samples per burst	512, 1024, or 2048

Table 3- 2. Deployment configuration of the evaluation of the five devices

Instrument Make & Model	Instrument Moniker	Motion Logger	GPS Pos (lon, lat)	Bottom Depth	Strop length (anchor to buoy)
Wave Rider	WRN		-34.204, 18.28667	70m	N/A
RDI Workhorse	SKL L=long strop	#3	-34.2078666, 18.2886666	75m	30m
RDI Workhorse	SKS S=short strop	#1	-34.2060833, 18.2905833	79m	4m
RDI Workhorse	SKA A=anchored		-34.209033, 18.2901167	78m	0m
Nortek AWAC	SKN	#4	-34.2113833, 18.2902833	75m	40m

Table 3- 3. Measurement regime of the ADCP instruments during the evaluation process

Instrument	Measurement interval	Burst duration	Notes
Wave Rider	30min	TDB	
RDI-SKL	90 min	600 sec	UVW-mem processing
RDI-SKS	90 min	600 sec	UVW-mem processing

RDI-SKA	90 min	600 sec	Standard processing
Nortek	90 min	1024 sec	AST processing

Table 3- 4. Deployment sites position and characteristics

Cape Agulhas	Deployed at 79 m with a 43 m strop (measurements from approximately 36 m); 35˚ 07.052 S, 019˚ 57.077 E; Deployed 23 September 2011, 00h10; UTR depths: 77 m, 67 m, 57 m, 47 m, 37 m;
Mossel Bay	Deployed at 79 m with a 43 m strop (measurements from approximately 36 m); 34˚ 18.719 S, 022˚ 25.986 E; Deployed 20 September 2011, 13h53; UTR depths: 77 m, 67 m, 57 m, 47 m, 37 m;
Tsitsikamma	Deployed at 79 m with a 43 m strop (measurements from approximately 36 m); 34˚ 03.653 S, 023˚ 52.132 E; Deployed 21 September 2011, 17h06; UTR depths: 77 m, 67 m, 57 m, 47 m, 37 m;
Cape Recife	Deployed at 80 m with a 43 m strop (measurements from approximately 37 m); 34˚ 05.316 S, 025˚ 32.321 E; Deployed 21 September 2011, 06h43; UTR depths: 78 m, 68 m, 58 m, 48 m, 38 m;

The measured data were processed according to the following configuration:

Table 3- 5. Configuration set up of the ADCP Nortek AWAC for the four selected moorings

WaveBase Version	3.22
Processing Method	SUV
Wave Coordinate System	BEAM
Spectrum Selected	Depth Optimized
Wave Direction	From
Beams Included	1 2 3 4
Number of Bins for Smoothing	64
Start Frequency	0.02
End Frequency	0.49
Start Frequency AST	0.49

Frequency Step	0.01
Mounting Height	0.50
Directional and Pressure Offsets	0.00

Output Wave Files

The following output wave files were acquired as a result of the insitu measurements done by the AWAC current and wave profiler:

Table 3- 6. Description of the Nortek AWAC output files according to the AST configuration listed on the Table 3- 7

Wave parameter file *.wap	Estimates of the standard wave parameters for each wave burst measurement.
Wave engery spectra file *.was	Estimates the energy spectra for each burst and begins with the frequency values used (Hz). The units for the energy spectra are (m^2/Hz)
Wave directional spectra file *.wdr	Estimates the direction at each frequency, or the "directional spectra" for each burst and begins with the frequency values used (Hz). The units for the energy spectra are (degrees).
Wave full directional spectra file *.wds	Presents the energy distribution over both direction and frequency.
Wave Fourier coefficient file *.wcf	presents the first two Fourier coefficient pairs at each frequency
Wave band estimates file *.wbd	Estimates for swell and wind waves. The bands for swell and seas is defined in the processing settings with the processing parameter called separation frequency

Selection of Parameters

As referenced before, the AWAC employed for the measurements at the four selected sites was set up in the AST mode, and the respective wave parameters output files contains the following information:

Table 3- 7. Breakdown of the wave parameters acquired by the AST configuration mode.

Significant Wave Height (Hm0)	**Hm0** = 4sqrt(sum(**M0**)).
Mean 1/3 Wave Height (H3)	This is the mean of the 1/3 largest wave in a record.
Mean 1/3 Wave Height (H3)	This is the mean of the 1/10 largest wave in a record. **H10 = 1.27Hm0**
Maximum Wave Height (Hmax)	This is the largest wave in a record. **Hmax = 1.67Hm0**
Mean Period (Tm02)	This is the average period for all the waves in the burst and it is calculated from the energy spectrum according to the first and second moment of the energy spectrum: **Tm02 = sum(M0/M02)**.

Peak Period (Tpeak)	This is the period of the waves corresponding to the peak frequency for the wave spectrum.
Mean Zero-crossing Period (Tz)	This is the mean period calculated from the zero-crossing technique. It is calculated as the mean of all the periods in the wave burst.
Peak Direction (TpDir)	This is the direction of the wave corresponding to the peak period. The direction is reported as "from" and is reported in degrees.
Directional Spread (Spr1)	The directional spread is a measure of the directional variance. The estimate is calculated for the peak frequency.
Main Direction (Mdir)	This value is a weighted average of all the directions in the wave spectrum
Unidirectivity Index	This is a measure of how much of the wave energy over the full spectrum is from a single direction. Values range from 0.0 to 1.0, and a value of 1.0 indicates the energy is from one primary direction. Wave spectra with peak energy at several directions or frequencies will lead to lower values.
Mean Pressure	The mean pressure is calculated over the duration of the burst, and provides estimate of the depth.

Auxiliary Figures

A1

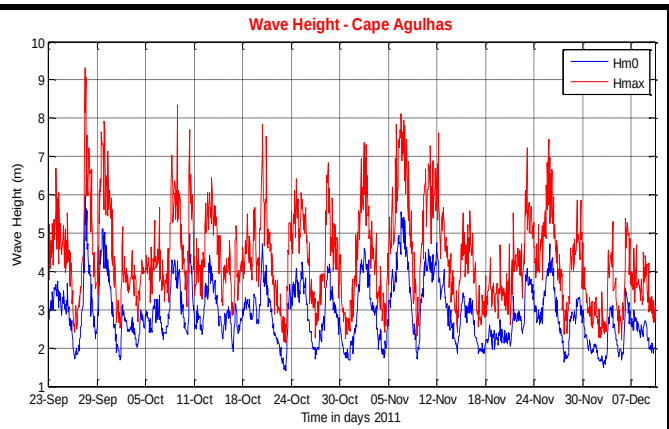

A2

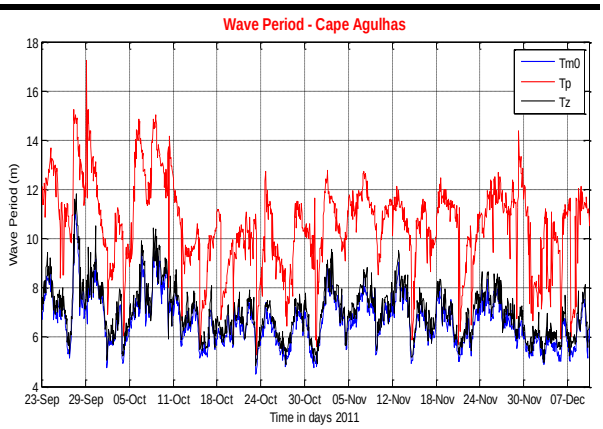

A3

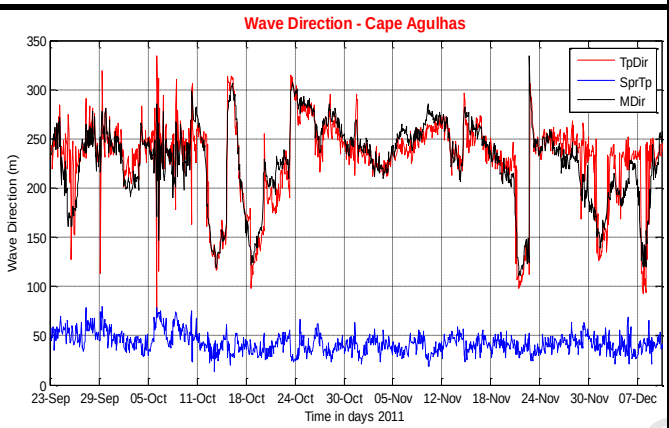

A4

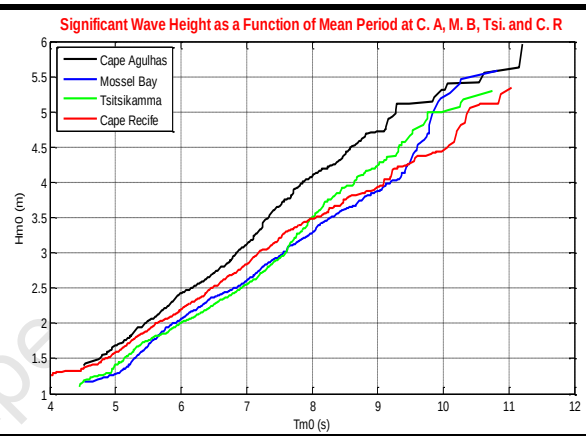

A5

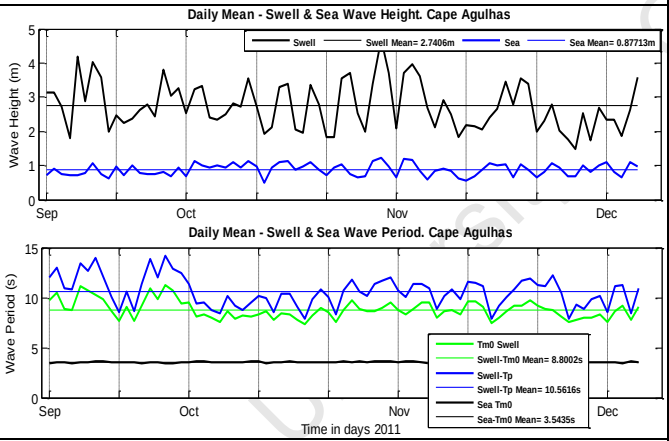

A6

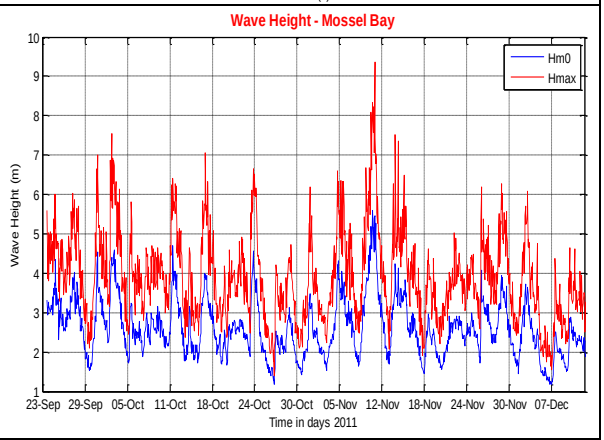

A7

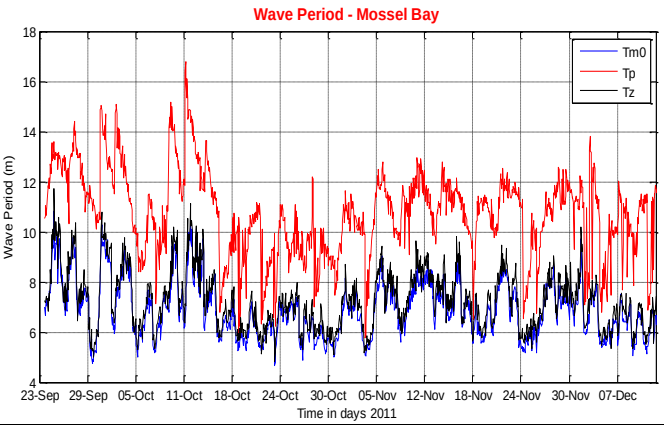

A8

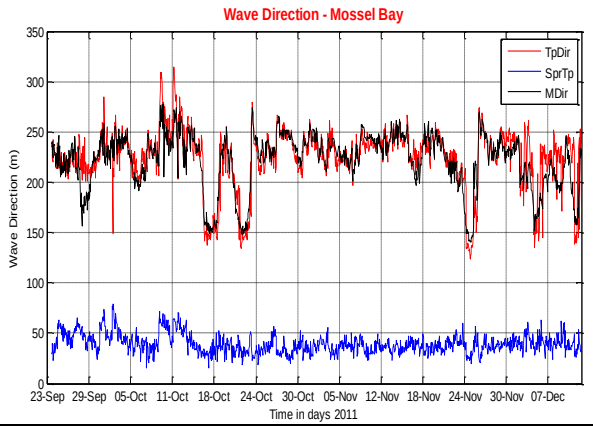

A9

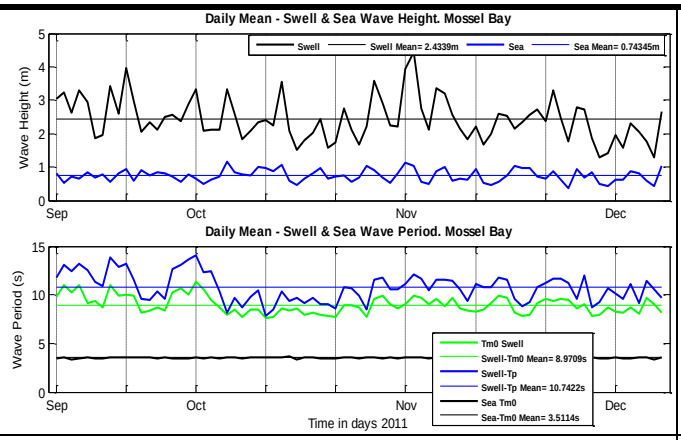

A10

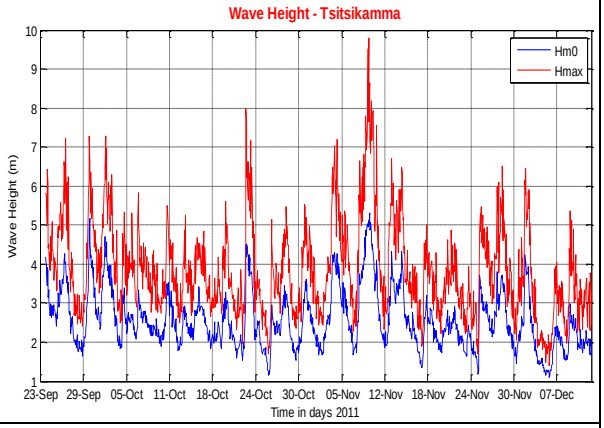

A11

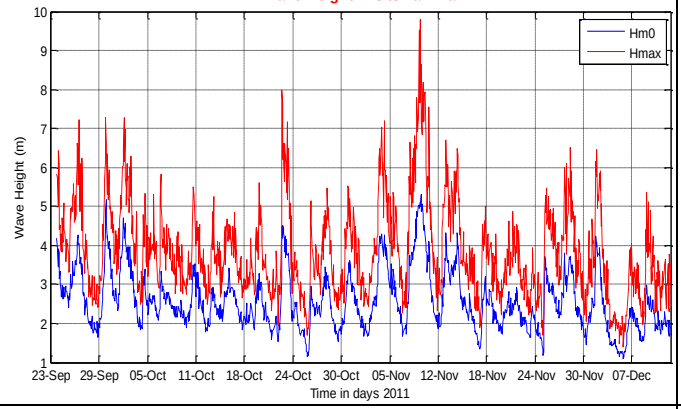

A12

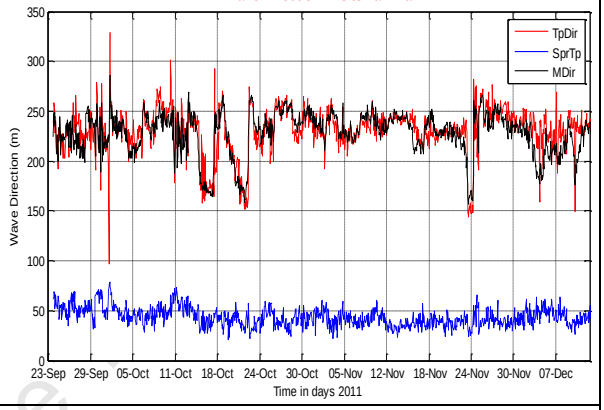

A13

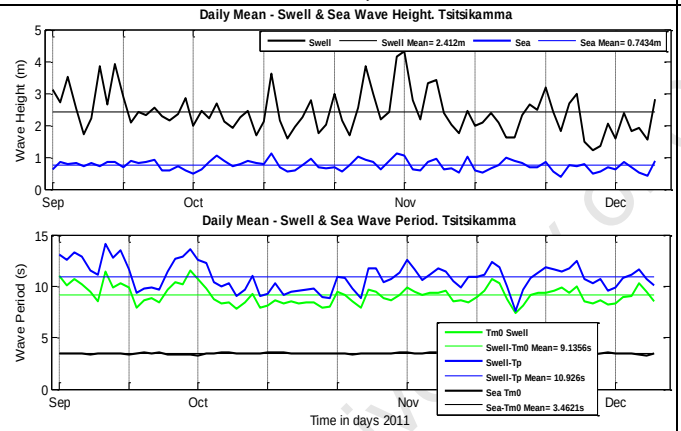

A14

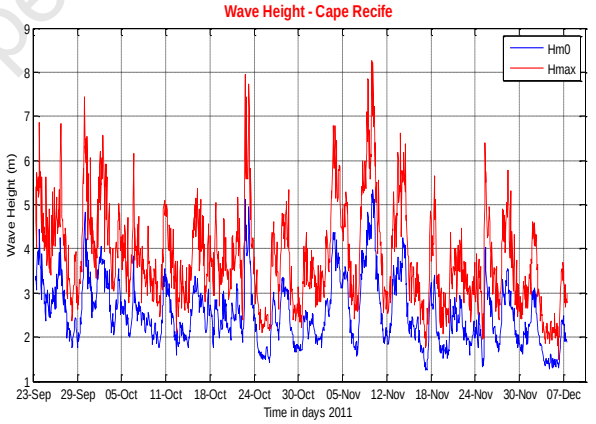

A15

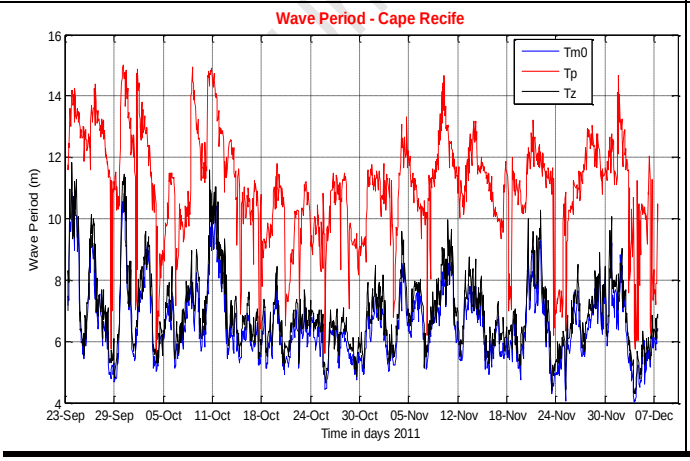

A16

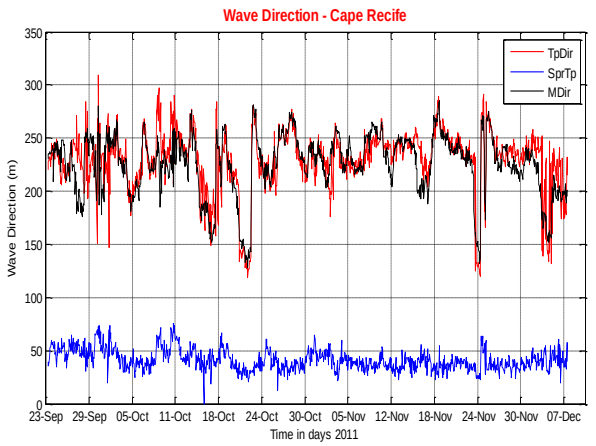

A17

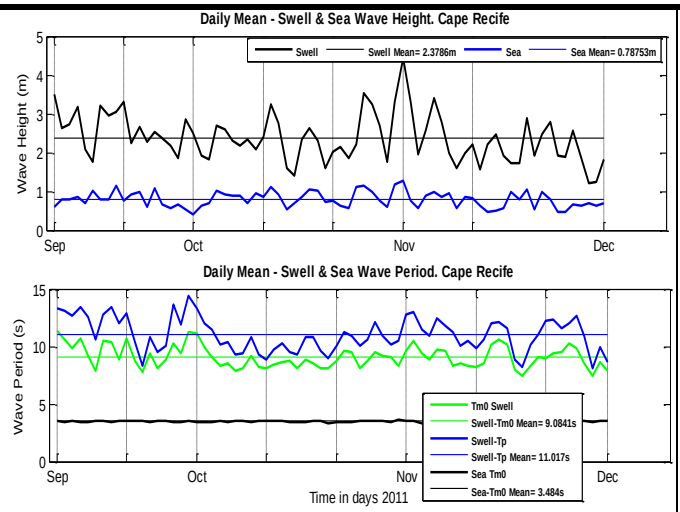

A18

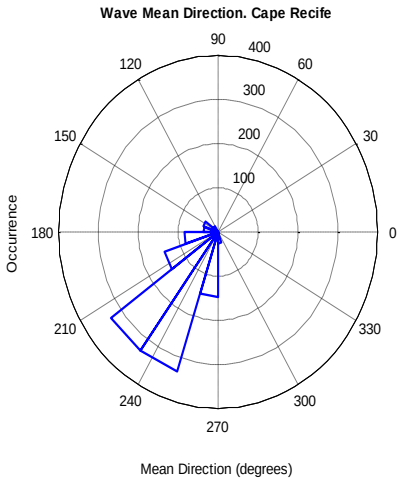

A19

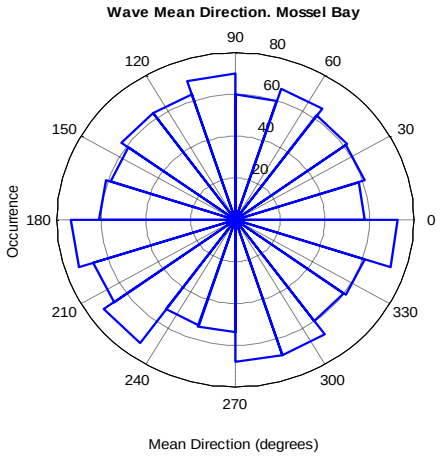

A20

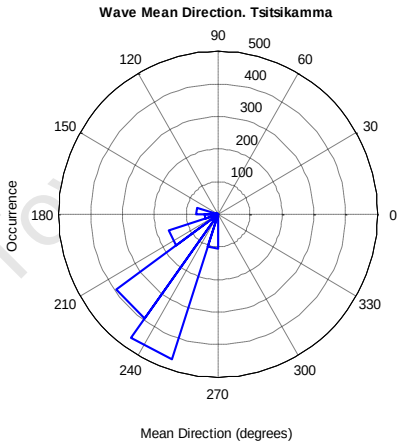

A21

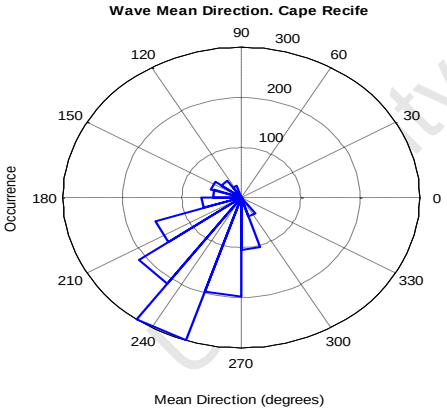

A22

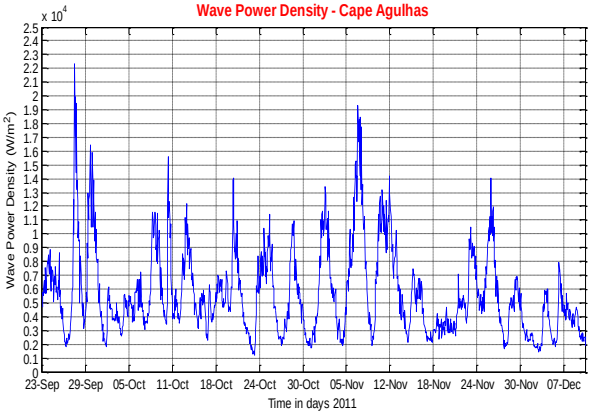

A23

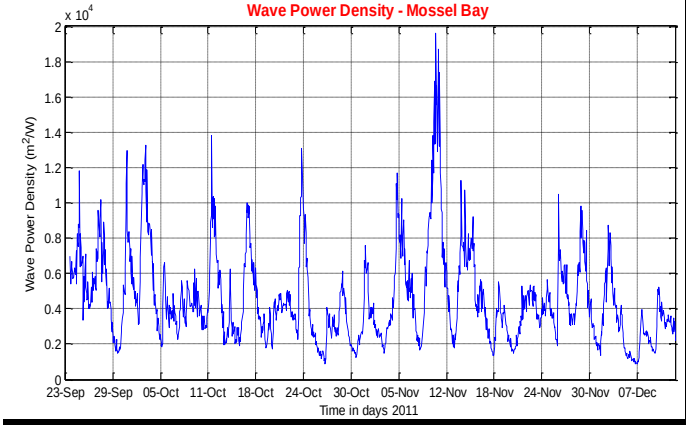

A24

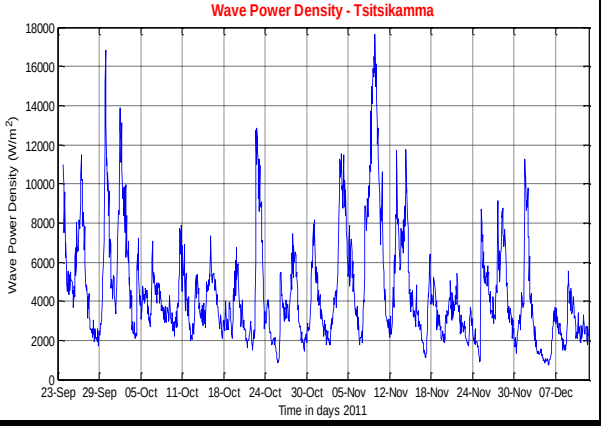

A25

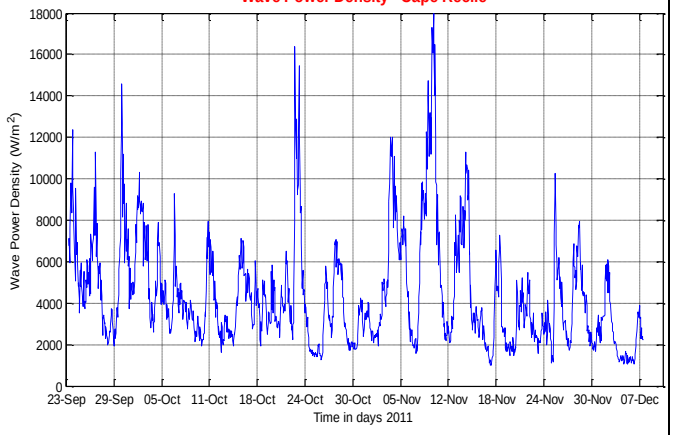

A26

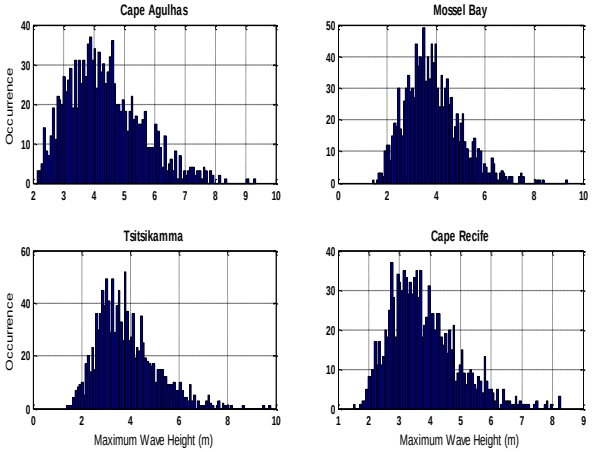

A27

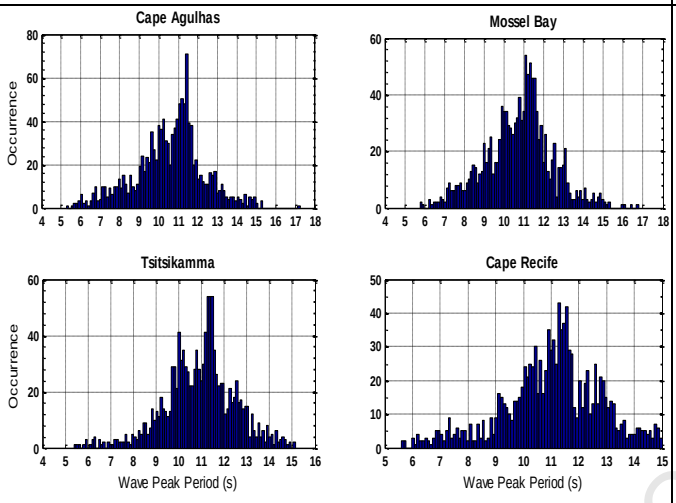

A28

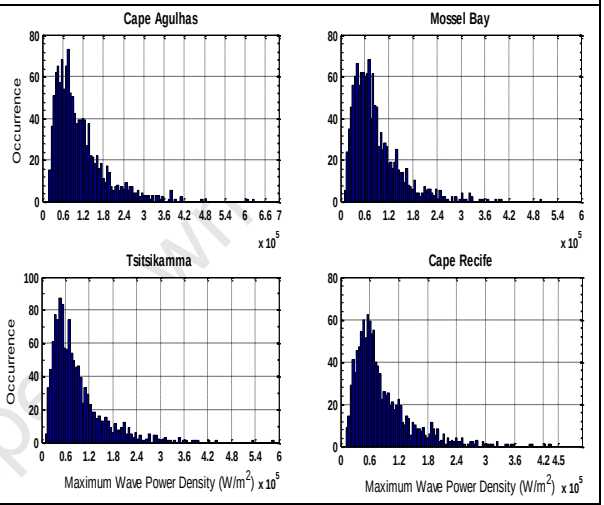

A29

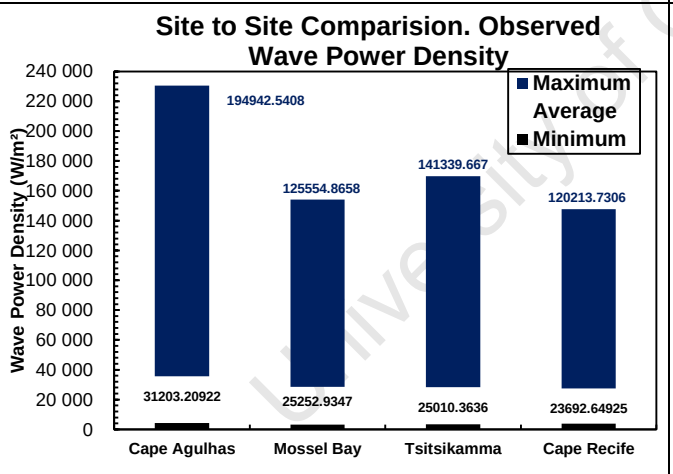

A30

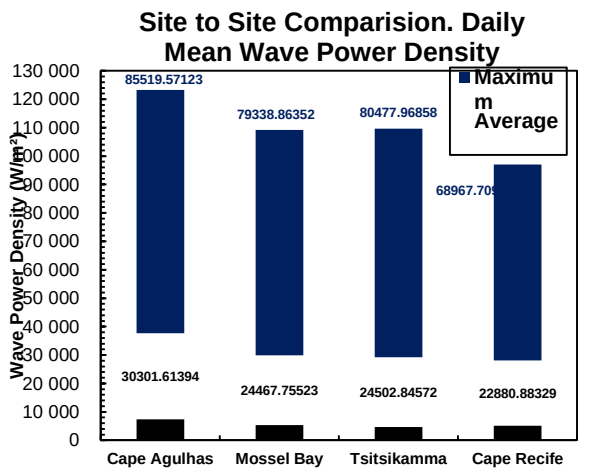

A31

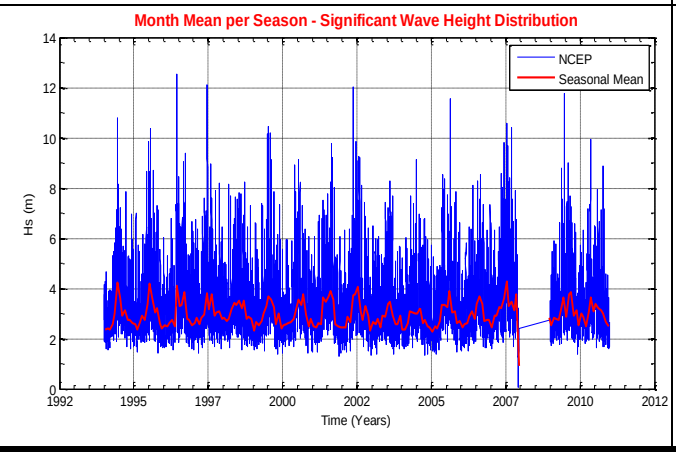

A32

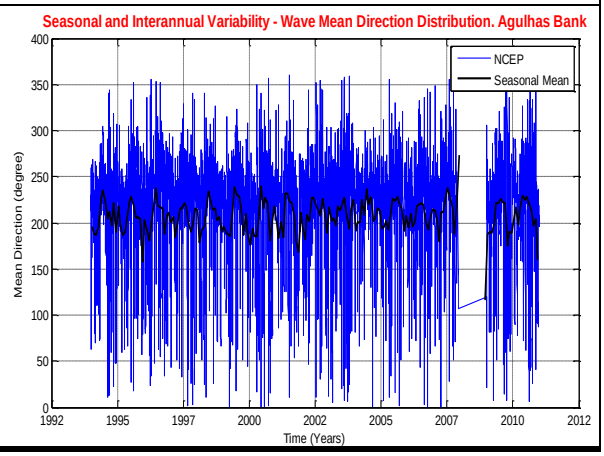

A33

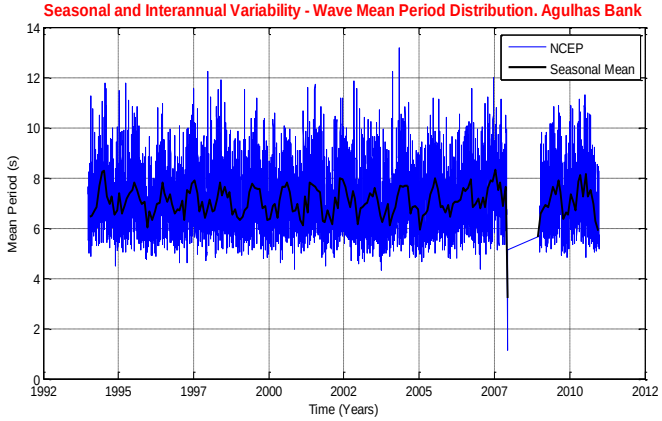

A34

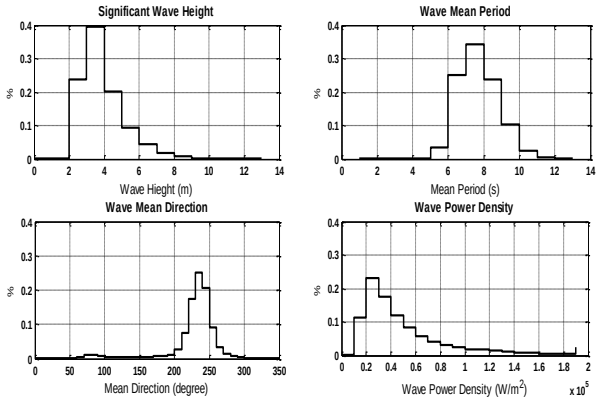

A35

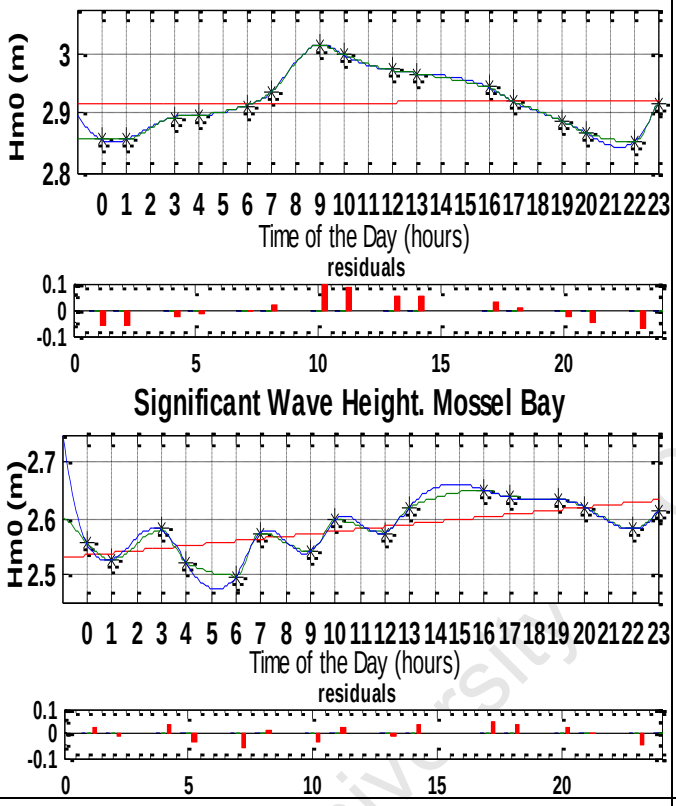

A36

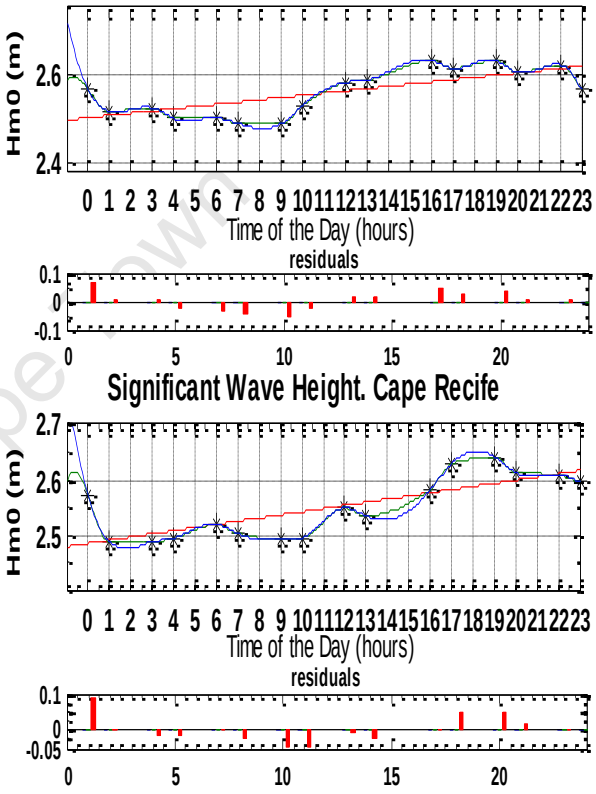

A37

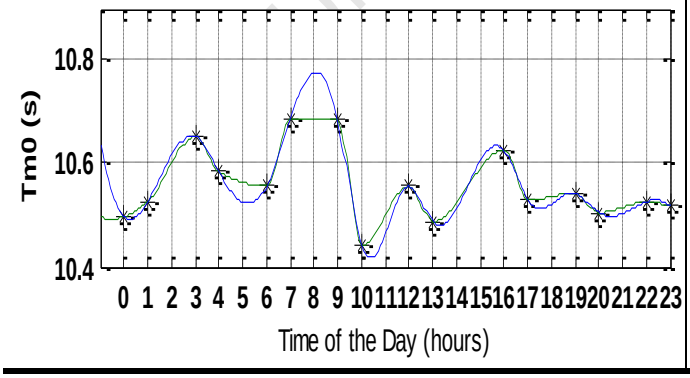

A38

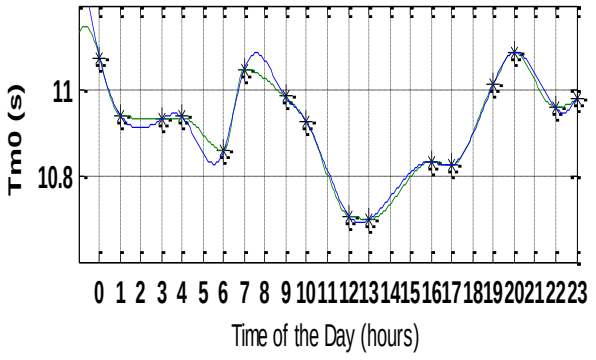

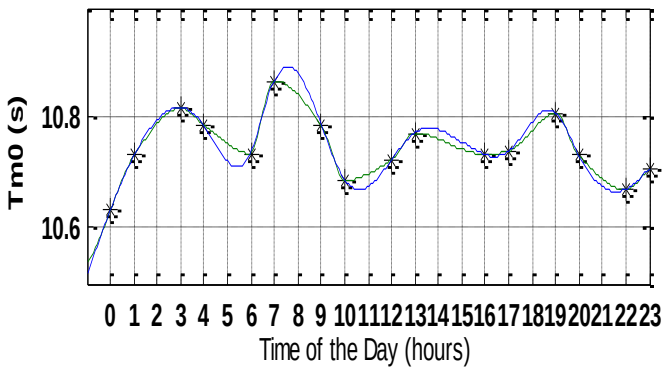

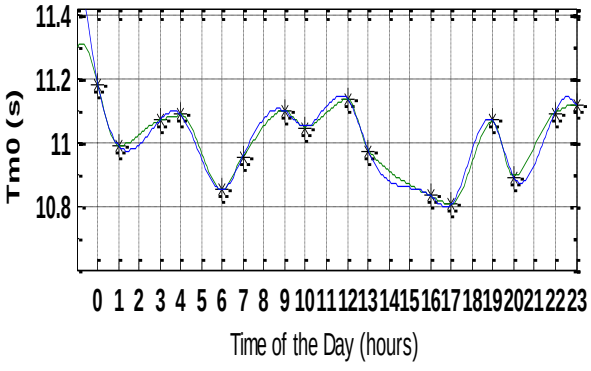

A39

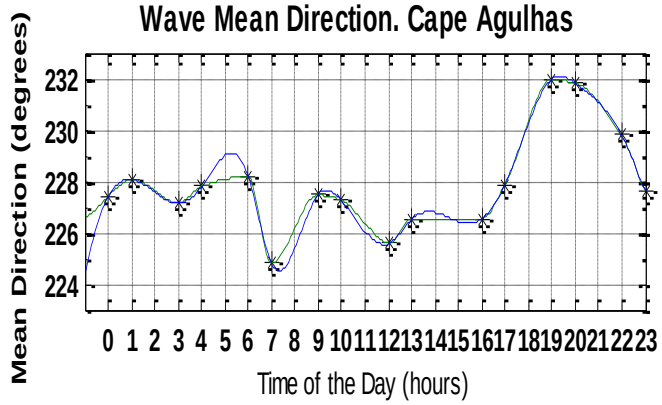

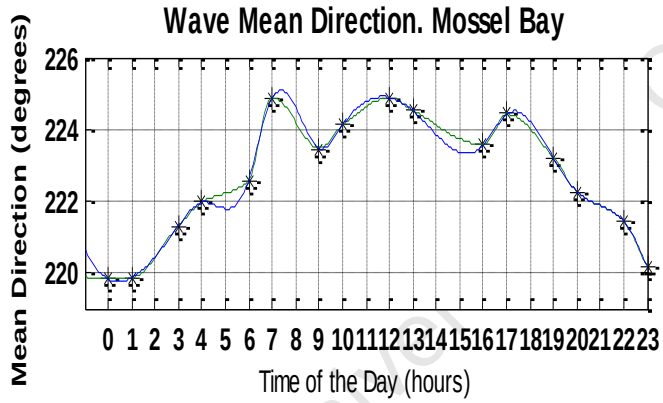

A40

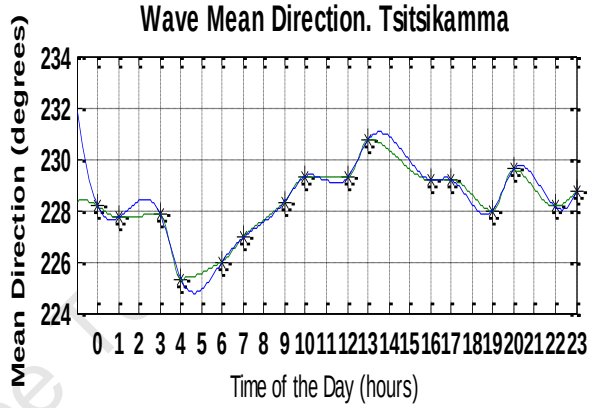

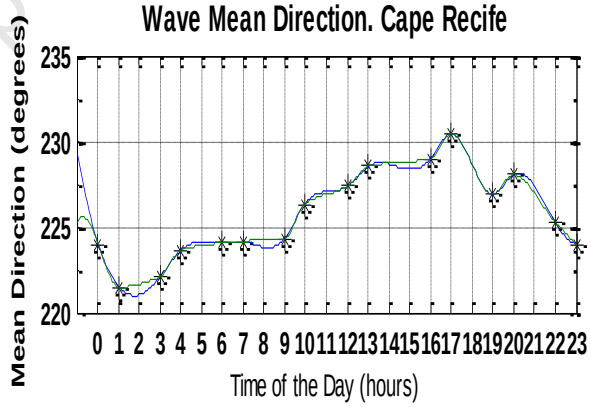

A41

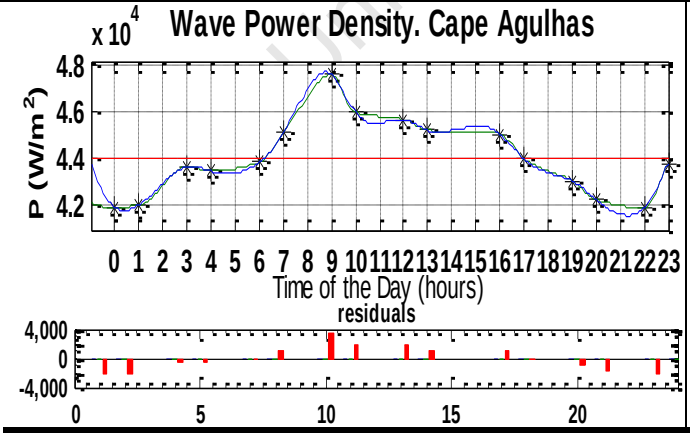

A42

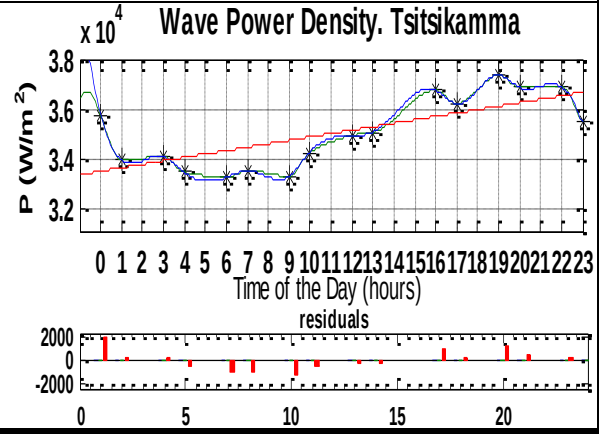

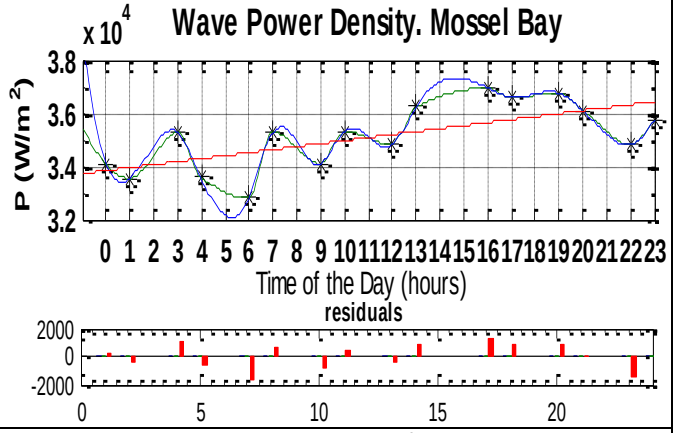
Wave Power Density. Mossel Bay
x 10^4
P (W/m^2)
Time of the Day (hours)
residuals

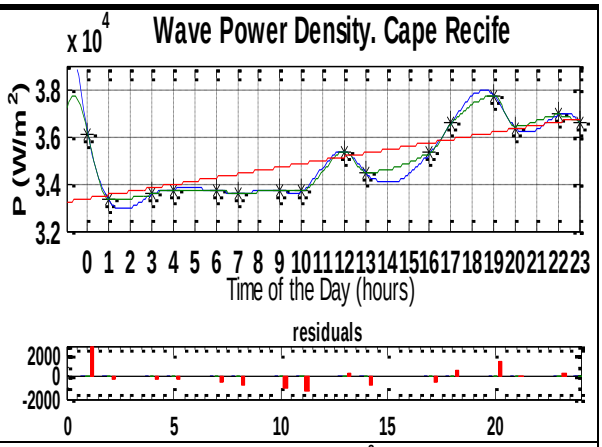
Wave Power Density. Cape Recife
x 10^4
P (W/m^2)
Time of the Day (hours)
residuals

A43

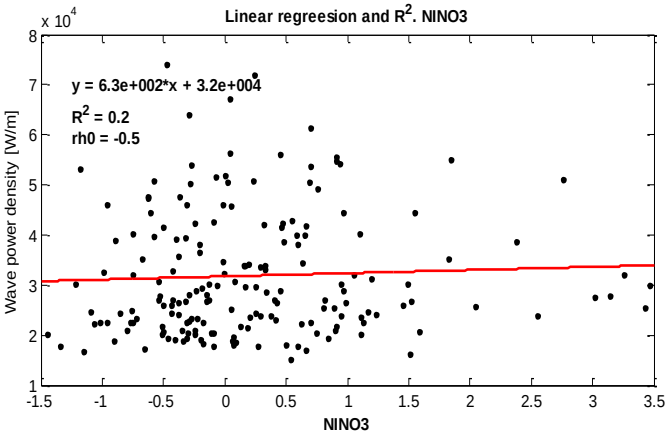
Linear regreesion and R^2. NINO3
y = 6.3e+002*x + 3.2e+004
R^2 = 0.2
rh0 = -0.5
Wave power density [W/m]
NINO3

A44

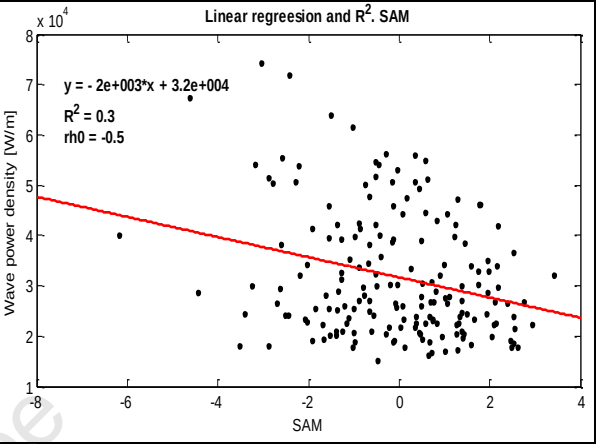
Linear regreesion and R^2. SAM
y = - 2e+003*x + 3.2e+004
R^2 = 0.3
rh0 = -0.5
Wave power density [W/m]
SAM

A45

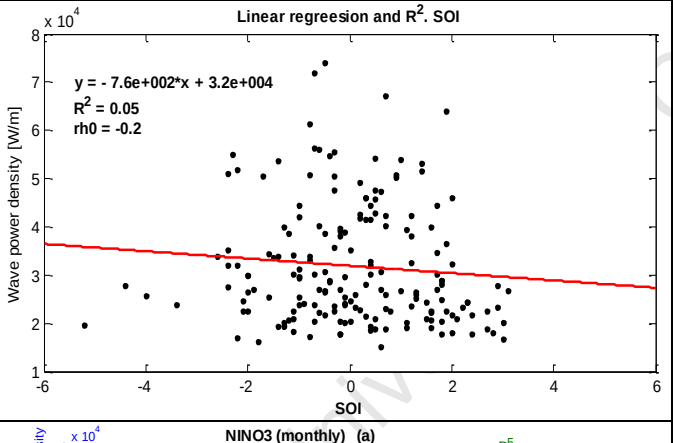
Linear regreesion and R^2. SOI
y = - 7.6e+002*x + 3.2e+004
R^2 = 0.05
rh0 = -0.2
Wave power density [W/m]
SOI

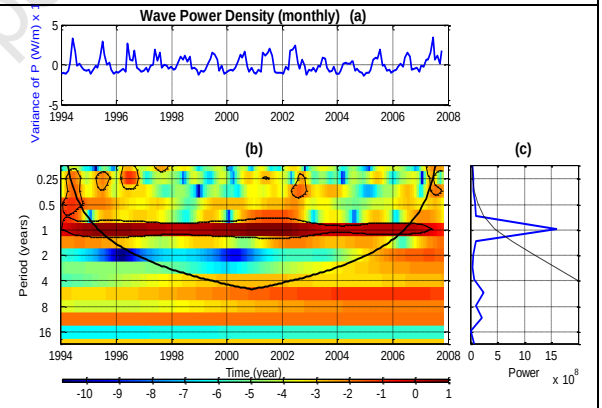
Wave Power Density (monthly) (a)
Variance of P (W/m) x
(b)
(c)
Period (years)
Time (year)
Power

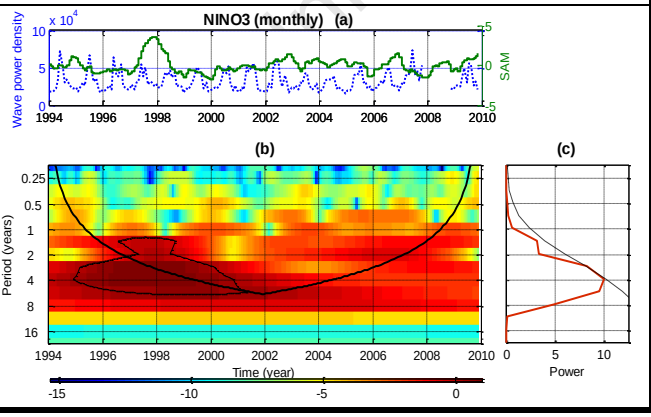
NINO3 (monthly) (a)
Wave power density
SAM
(b)
(c)
Period (years)
Time (year)
Power

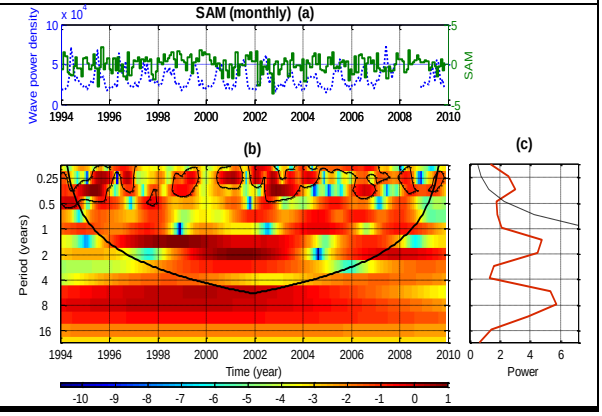
SAM (monthly) (a)
Wave power density
SAM
(b)
(c)
Period (years)
Time (year)
Power